Table of Contents

Chapter 1 1
Introduction 1
References 4
Chapter 2 5
ZnO as a semiconductor 5
2.1 Introduction 5
2.2 Crystal structure 5
2.3 Material growth techniques 7
2.4 Properties and Applications 8
2.5 Metal/ZnO contacts 11
2.5.1 Introduction 11
2.5.2 Ohmic contacts 11
2.5.3 Schottky contacts 12
2.5.3.1 Current-voltage (IV) measurements 13
2.5.3.2 Capacitance-voltage (CV) measurements 18
2.5.4 The Depletion layer 19
Summary 23
References 24
Chapter 3 27
Defects in semiconductors 27
3.1 Introduction 27
3.2 Point defects 28
3.2.1 The Oxygen vacancy 29
3.2.2 The Zinc vacancy 30
3.2.3 The Zinc interstitial 31
3.2.4 Negative-*U* and Metastability 31
3.3 Extended defects 34
3.3.1 Line defects 35
References 37
Chapter 4 39
Defect characterization 39
4.1 Introduction 39

4.2 Emission and capture of carriers from deep levels 39
4.3 Deep level transient spectroscopy, DLTS 43
4.3.1 DLTS Concepts 47
4.3.2 Peak height dependence on rate window frequency 51
4.3.3 Temperature dependence of the capture cross-section 52
4.4 Defect Depth profiling 55
4.5 Laplace DLTS 56
4.5.1 Introduction 56
4.5.2 Laplace DLTS principles 57
Summary 58
References 59
Chapter 5 61
Experimental Techniques 61
Introduction 61
5.1 Sample cleaning 61
5.2 Contact fabrication 61
5.3 Current-Voltage and Capacitance-Voltage measurements 64
5.4 Deep Level Transient Spectroscopy (DLTS) and Laplace-DLTS 66
5.5 Sample annealing 67
5.6 Proton irradiation 68
References 68
Chapter 6 69
Results and discussions 69
6.1 Defects in ZnO 69
Introduction 69
Results and discussions 69
Publication 1: On the temperature dependence of the electron capture cross-section of the E3 deep level observed in single crystal ZnO 74
Summary 78
References 79
6.2 Electron-beam induced defects 80
Introduction 80
Results and discussions 81

Publication 2: A comparative study of the electrical properties of Pd/ZnO Schottky contacts fabricated using electron beam deposition and resistive evaporation techniques 85

Summary 86

References 87

6.3 Annealing studies of ZnO using Hall Effect, IV and DLTS 88

Introduction 88

6.3.1 Hall effect studies 89

Introduction 89

Publication 3: Annealing and surface conduction on hydrogen peroxide treated bulk melt-grown, single crystal ZnO 89

6.3.2 IV measurements 90

Introduction 90

Publication 4: Thermal annealing behaviour of Pd Schottky contacts on melt-grown single crystal ZnO studied by IV and CV measurements 90

Summary 90

6.3.3 DLTS Studies 91

Introduction 91

Results and discussions 91

6.3.3.1 Vacuum annealing 91

6.3.3.2 Oxygen annealing 96

6.3.3.3 Argon annealing 101

Publication 5: Effects of hydrogen, oxygen, and argon annealing on the electrical properties of ZnO and ZnO devices studied by IV, DLTS and LDLTS 106

Summary 106

Conclusions 107

References 108

6.3.4 Argon and Oxygen annealing 109

Introduction 109

Publication 6: Effects of high temperature annealing on single crystal ZnO and ZnO devices 112

Summary 112

6.4 Irradiation induced defects 113

Introduction 113

Summary 115

References 115

Chapter 7 116
Conclusions 116
Summary of deep level defects observed and characterized in this study 118
Chapter 8 119
Future Work 119

Chapter 1

Introduction

ZnO is a wide and direct bandgap semiconductor with experimental band gap energy of 3.4 eV. This material exists naturally as n-type whose conductivity is attributed to the existence of native point defects such as Zn interstitials and oxygen vacancies [1]. Impurities such as hydrogen [2, 3] which acts as a shallow donor and aluminium [4, 5] also contribute to the n-type conductivity of ZnO. As in other wide bandgap materials, there exists the so-called doping asymmetry, i.e. it is easy to obtain n-type ZnO but rather difficult to produce p-type ZnO. The existence of native defects in ZnO has hindered success in the fabrication of UV light emitting diodes because of their self-compensation behaviour [6].

ZnO possesses superior electronic and optoelectronic properties which make it a good candidate in optoelectronic, transparent electronics and spintronics applications. Its high efficiency in UV emission makes it a good material for fabrication of white lighting devices [7]. The resistance to radiation damage makes it possible to fabricate devices on ZnO that can operate within the UV region and in space applications, e.g. in solar cells as a transparent conducting oxide (TCO) [8], UV photodetectors, just to mention a few.

The use of ZnO in the fabrication of devices that can operate in space applications requires the devices to be highly stable, i.e. they must be resistant to high temperature fluctuations. Stable contacts on ZnO can be obtained through the use of metals with high melting points. The main problem with these types of contacts lies in the fabrication techniques to be used. With high melting point metals, the likely deposition techniques include among others, the electron-beam (e-beam) deposition and sputter deposition. However, these techniques tend to introduce defects in devices.

Defects are often detrimental to device operation. The use of ZnO in the fabrication of solar cells and UV detectors requires the material to be of high quality, i.e. with minimal defects as defects often influence the electrical and optical properties of semiconductors by affecting the doping, minority carrier lifetime and luminescence efficiency.

Apart from native point defects, ZnO also possesses deep level emission bands that emit all colours in the visible range with good colour rendering properties [9]. Knowledge and control of defects is essential to improve efficiency of devices; by removing them in the case of solar cell applications. Also, an understanding of the origins of emissions related to deep level defects in ZnO for development of highly efficient optoelectronic devices is required, i.e. to introduce them if necessary. Annealing of crystals is one possible way of recovering or removing defects in semiconductors. Defects can also be intentionally introduced in semiconductor material by irradiating with energetic particles.

Defect characterization in semiconductors is important for fabrication of high quality devices as it provides an understanding of the defect identity, defect control, properties and influence on devices. Different techniques have been used to characterize defects in semiconductors, some of which include the Hall Effect, positron annihilation spectroscopy (PAS), X-ray diffraction, Rutherford backscattering spectroscopy (RBS), admittance spectroscopy, cathodoluminescence and photoluminescence. In this thesis, deep level transient spectroscopy (DLTS) has been used to characterize deep level defects in ZnO.

DLTS is a capacitance based spectroscopic technique that can give information about the signature of an electrically active defect state, i.e. the activation enthalpy and capture cross-section within the bandgap of a semiconductor. This depletion layer method provides an environment where the occupancy of a deep state can be manipulated with relative ease [10, 11] by probing the depletion region of a metal/semiconductor contact, metal oxide semiconductor structure or an ordinary p-n junction.

An overview of the properties of ZnO as a semiconductor and its use in the fabrication of rectifying metal/semiconductor contacts is given in chapter 2. Chapter 3 gives an outline of defects in semiconductor materials with particular reference to ZnO. A method of characterizing defects in materials using capacitance based DLTS and Laplace-DLTS techniques is given in chapter 4. Experimental techniques employed in this particular work are outlined in chapter 5. Chapter 6 contains all the results and discussions obtained from this

work. A summary of conclusions drawn from the study are presented in chapter 7, while chapter 8 contains details of future studies to be carried out on ZnO.

Bestpfe.com

References

1. D. C. Look, J. W. Hemsky and J. R. Sizelove, Phys. Rev. Lett. **82**, 2552 (1999)
2. D. G. Thomas and J. J. Lander, J. Chem. Phys. **25**, 1136 (1956)
3. E. Mollwo, Z. Phys. **138**, 478 (1954)
4. M. D. McCluskey and S. J. Jokela, Physica B, **401**, 355 (2007)
5. T. Minami MRS Bull. **25** (8), 38 (2000)
6. M. Willander, O. Nur, Q. X. Zhao, L. L. Yang, M. Lorenz, B. Q. Cao, J. Zuniga Perez, C. Czekalla, G. Zimmermann, M. Grundmann, A. Bakin, A. Behrends, M. Al-Suleiman, A. El-Shaer, A. C. Mofor, B. Postels, A. Waag, N. Boukos, A. Travlos, H. S. Kwack, G. Guinard, D. Si Le Dang, Nanotechnol. **20**, 332001 (2009)
7. A. Zainelabdin, S. Zaman, G. Amin, O. Nur, and M. Willander, Nanoscale Res. Lett. **5**, 1442 (2010)
8. A. Nuruddin, and J. R. Abelson, Thin Solid Films, **394**, 49 (2001)
9. M. Willander, O. Nur, N. Bano, K. Sultana, New J. Phys. **11**, 125020 (2009)
10. D. V. Lang, J. Appl. Phys. **45**, 7 (1974)
11. L. Dobaczewski, A. R. Peaker, K. Bonde Nielsen, J. Appl. Phys. **96**, 9 (2004)

Chapter 2

ZnO as a semiconductor

2.1 Introduction

ZnO is a wurtzitic compound semiconductor with a wide and direct bandgap of 3.4 eV at room temperature. This material occurs naturally as n-type with the native defects particularly zinc interstitials, and oxygen vacancies being proposed to be the source of n-type conductivity [1]. Some reports claim that the n-type conductivity is due to some impurities [2] introduced during material growth predominantly hydrogen and other group I related elements, arguing that the oxygen vacancy is too deep to contribute a significant concentration to the n-type conductivity of ZnO [3,4,5,6,7]. The effects of hydrogen in ZnO have been studied. It has been proposed that hydrogen in ZnO is a shallow donor [2,8,9] and can form several bond structures which include the BC_{II} and $BC_{\perp}$ configurations [2]. However the realization of *p*-type ZnO still remains a challenge as it lacks reproducibility [10, 11].

2.2 Crystal structure

ZnO is a highly ionic compound semiconductor which crystallizes into three common lattice structures, and these are; the rock salt, zinc blende and the wurtzite structure. The wurtzite structure is the most thermodynamically stable one at ambient conditions [12] i.e. for bulk ZnO crystals. This structure can be considered as two interpenetrating hexagonal-close-packed lattices, characterized by two interconnecting sublattices of Zn^{2+} and O^{2-} such that each Zn ion is surrounded by a tetrahedral of O ions and vice versa [13]. The tetrahedral arrangement gives rise to the polar symmetry along the hexagonal axis. Four common terminations for the wurtzitic ZnO structure exist and these are; Zn-polar terminated (0001)

BESTPFE.COM
List of research project topics and materials

and the O-polar terminated $(000\bar{1})$ faces (*c*-axis oriented), the non-polar $(11\bar{2}0)$ (a-axis) and $(10\bar{1}0)$ faces which both contain an equal number of Zn and O atoms. Due to the difference in face terminations, the polar faces have different physical and chemical structures; with the O-polar face having a unique electronic structure from the other three [13]. The wurtzite structure of ZnO is shown in Figure 2.1.

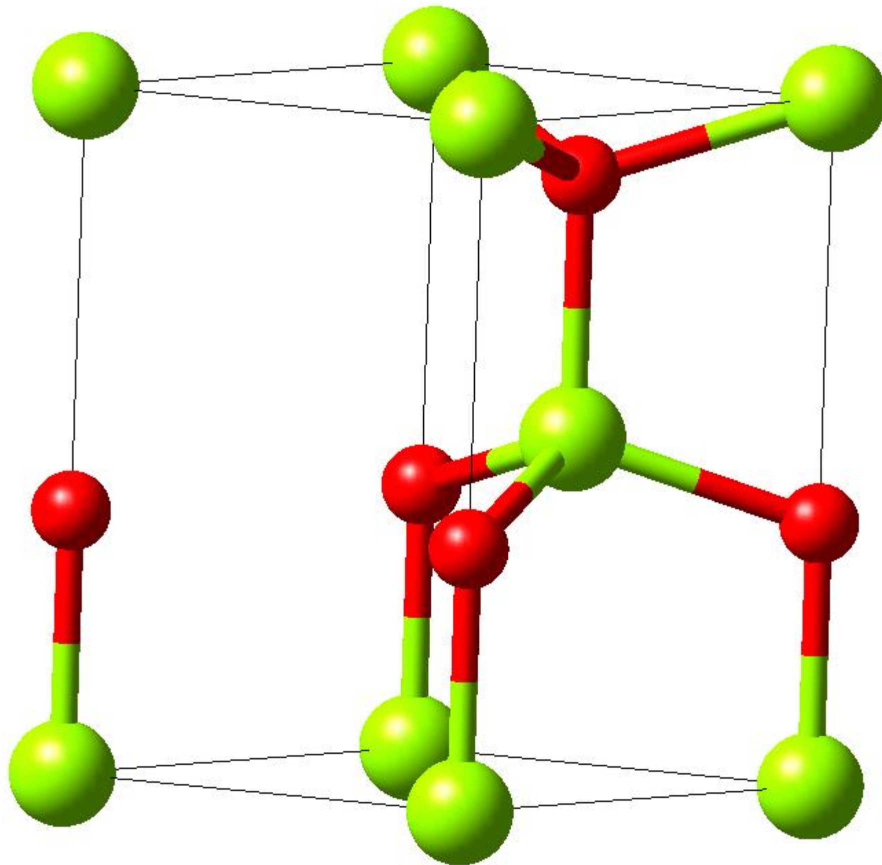

Figure 2.1: *The hexagonal wurtzite structure of ZnO. O atoms are shown as small dark spheres, Zn atoms as large light spheres. Redrawn from ref* [*14*].

The physical parameters of the wurtzite ZnO structure are given in Table 2.1.

Table 2.1: *Physical parameters of the wurtzite ZnO structure*

Parameter name	Symbol	Value	Temperature (K)	Ref
Lattice constants	a	3.249Å		[15]
	c	5.205Å		
Primitive lattice cell volume	V_{lc}	23.79Å^3		[15]
Electron affinity	χ	4.57 eV	300	[16]
Electron effective mass	m_e^*	0.27		[17]
Hole effective mass	m_h^*	0.59		[18]
Dielectric constants	ε_s^{II}	7.46		[19]
	$\varepsilon_s^{\perp}$	8.59		
Effective density of states	N_{C}	3.5×10^{18}cm^{-3}	300	[20]
	N_{V}	1.1×10^{19}cm^{-3}	300	

2.3 Material growth techniques

ZnO is available as bulk single crystals and also as thin films. Bulk material is grown using the hydrothermal, chemical vapour transport (CVT), and melt growth techniques, while thin film material is grown using the pulsed laser deposition, metalorganic chemical vapour deposition (MOCVD), metalorganic vapour phase epitaxy (MOVPE), just to mention a few. In this particular study, main focus is on melt grown bulk ZnO single crystals. Traditional melt growth processes rely on material growth from a melt or liquid. They are associated with three main hindrances, which include melt containment, ZnO decomposition at atmospheric pressure near the melting point, and crystal contamination [21]. These problems are however eliminated in the melt growth technique used by Cermet [21]. The melt growth technique produces high quality material that is free from solvent related impurities and thus minimal defects. The other advantage of this technique is the high material growth rate [21].

2.4 Properties and Applications

Due to its wide bandgap, this material finds its use in several applications some of which include the fabrication of ultraviolet detectors and daylight-blind UV detectors, transparent conducting oxides, acoustic wave devices, light emitting diodes, laser diodes, high frequency electronic devices, varistors, piezoelectric transducers, and paints. ZnO has an excitonic binding energy of 60 meV at room temperature and is compatible with the conventional chemistry etching similar to that used in Si technology which gives it more advantages over other wide band gap materials, e.g. GaN.

The use of ZnO in the electronic and optoelectronic industries requires the fabrication of highly stable good quality metal/ZnO contacts. Fabrication of good quality rectifying contacts has been a problem since the early discoveries of the material and still remains a challenge as different Schottky barrier heights have been reported for the same metal deposited on ZnO. Reports have indicated the dependence of contact quality on cleaning procedures used other than on the metal work function [22]. Polarity of the material [23] (in the case of bulk material) and the deposition techniques used [24] have also been reported to affect contact quality. This is valid since different cleaning procedures will influence the surface states, hydrocarbon and hydroxide surface contamination, oxygen chemisorption, subsurface defects and surface morphology due to the chemical reactions taking place at the surface. The above-mentioned will in turn affect the metal-surface reactions and hence the contact quality.

Table 2.2 shows the variation of measured current voltage (IV) parameters with cleaning procedures and deposition techniques from selected references. These parameters have been obtained at room temperature.

Table 2.2: *Values of barrier height, ideality factor and degree of rectification (defined as the ratio of the forward current to the reverse current at 1.0V) from selected references.*

Growth Technique	Cleaning Procedure	Deposition Technique	Metal (ZnO-face)	Barrier Height(eV)	Ideality factor	Degree of Rectification	Ref
hydrothermal	OS	e-beam	Pd(O-polar)	0.75	1.4	~2	[25]
Melt	OSA	e-beam	Pd(Zn-polar)	0.55	2.0	~2	[23]
Melt	OSA	e-beam	Pd(O-polar)	0.59	1.2	~4	[23]
Melt	OSA	e-beam	Pt(Zn-polar)	0.55	2.0	~2	[23]
Melt	OSA	e-beam	Pt(O-polar)	0.68	1.2	~4	[23]
Melt	OSA	resistive	Au(Zn-polar)	0.71	1.4	~5	[23]
Melt	OSA	resistive	Au(O-polar)	0.69	1.1	~5	[23]
Melt	OSA	resistive	Ag(Zn-polar)	0.78	1.2	~7	[23]
Melt	OSA	resistive	Ag(Zn-polar)	0.77	1.1	~7	[23]
Melt	OSP	resistive	Au(Zn-polar)	0.63	1.15	~4	[26]
MOCVD	OSP	-	Pt(--)	0.78	1.02	~6	[27]
Hydrothermal	OSA	sputter	Pt(Zn-polar)	0.96	1.1	~6	[28]
Hydrothermal	OSA	sputter	Pt(O-polar)	0.60	3.1	~2	[28]
PLD	OSA, RP	--	Pd($11\underline{2}0$)	0.68	1.4	~4	[29]
PLD	OSA, RP	--	Ag($11\underline{2}0$)	0.59	1.4	-	[29]
Hydrothermal	ROP	e-beam	Ir(O-polar)	0.64	1.36	~4	[30]
Melt	OSP	resistive	Pd(O-polar)	0.77	1.85	~8	[31]
Melt	OSP	resistive	Pd(Zn-Polar)	0.72	1.43	~8	[34]
Melt	OSP	e-beam	Pd(Zn-Polar)	0.62	1.66	~5	[34]

* Organic solvents only, (OS), organic solvents and any acid etch (OSA), organic solvent and hydrogen peroxide treatment (OSP), Remotely oxygen plasma cleaned (ROP), remotely plasma cleaned (RP).

A dramatic improvement of contact quality has been reported after the treatment of the material with hydrogen peroxide [26,27,32,33,34,35]. The study of the effects of deposition techniques has not been extensively carried out. High quality metal/ZnO contacts are of importance in the fabrication of UV detectors and also in the characterization of deep level defects in semiconductors.

Modifications of the electrical properties of ZnO after annealing in different ambient conditions have been studied using Hall Effect measurements [36,37,38], photoluminescence [39] and DLTS measurements [40,41,42]. The Hall Effect measurements have indicated an increase in surface conductivity after hydrogen annealing [43, 44] which influences device characteristics. A reduction of the shallow donor concentration in ZnO after Ar annealing has been reported [45]. Passivation of deep level defects in ZnO after hydrogen annealing has also been observed using the PL measurements [44]. Oxygen annealing at high temperatures is also of very high significance as it helps in eliminating surface adsorbents. At the same time, it leads to surface thermal decomposition which is an ideal method for preparing the material for surface electronic studies. This clearly indicates that the electronic and optical properties of ZnO can be easily altered by thermal treatments to suit the needs of the researcher. The fact that ZnO allows for band gap engineering by alloying it with MgO and CdO to increase and decrease its bandgap energy, respectively [46] is an important aspect since it allows for tuning of the material’s optoelectronic properties for use in selected wavelengths of the electromagnetic spectrum for selective light sensing purposes.

2.5 Metal/ZnO contacts

2.5.1 Introduction

Metal/semiconductor contacts are important to the microelectronics industry as well as in the characterization of fundamental properties of semiconductors using junction techniques e.g. DLTS. The quality of a metal/semiconductor contact determines its performance as poor contacts result in undesired effects e.g. high leakage currents and low barrier heights. Metal/semiconductor quality is determined by a number of factors, some of which include the mismatch between the Fermi-energies of the metal and semiconductor, the semiconductor processing steps (cleaning and annealing) prior to contact fabrication and the contact fabrication techniques. These contacts are considered to be ohmic or rectifying (Schottky) as governed by their response to an applied external bias.

2.5.2 Ohmic contacts

A contact is said to be ohmic if the barrier formed from the intimate contact of a metal and semiconductor is zero. In an ideal ohmic contact, charge carriers are free to move in either direction across the contact with minimal or no resistance. To fabricate such a contact on an n-type semiconductor, we require that the metal work function must be closer to or smaller than the semiconductor electron affinity. Formation of such a contact is illustrated in Figure 2.2.

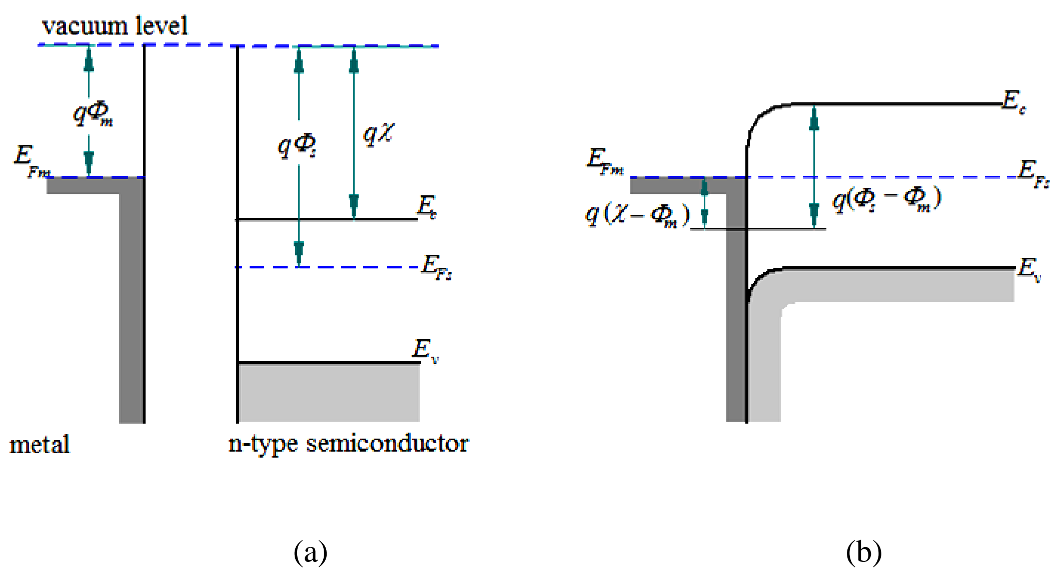

Figure 2.2: Ohmic contacts to n-type semiconductor $\Phi_M < \Phi_S$ *(a) before contact, (b) equilibrium band diagram for the contact. Adopted from ref* [14]

Bringing the metal into intimate contact with the semiconductor will result in Fermi-level alignment as shown in Figure 2.2b. This raises the semiconductor electron energies relative to the metal, reducing the barrier to electron flow between the metal and semiconductor. However under real situations, ohmic contact formation is affected by external factors, some of which include; conditions under which the contacts are fabricated, surface states, interface states, and also reactions between the metal and semiconductor. Ohmic contacts are classified into tunnel, and annealed and alloyed contacts; with the tunnel contacts being the most practical ones. Tunnel contacts possess a positive barrier at the metal/semiconductor interface, but also have enough doping in the semiconductor such that there is only a thin barrier separating the metal from the semiconductor. This thin barrier allows carriers to easily tunnel through the interface. For an ohmic contact, under any applied biasing conditions, the IV characteristics must always obey Ohm’s law, since there is a very thin barrier for electron flow in any given direction, i.e. metal to semiconductor or semiconductor to metal.

2.5.3 Schottky contacts

If a metal-semiconductor contact can rectify signals in the forward biased mode and allows negligible or no current to flow in the reverse bias, it is referred to as a Schottky contact. Ideal Schottky contacts are formed when a difference in potential exists between the Fermi energy of the metal and the band edge where majority charge carriers reside (ignoring the effects of surface and interface states). The formation of a Schottky contact is illustrated in Figure 2.3. The difference in potential between the Fermi-energy of the metal and semiconductor gives the barrier height, ϕ_B. For an n-type semiconductor, the barrier height is given theoretically as [47];

$$\phi_B = \phi_M - \chi_S \tag{2.1}$$

where ϕ_M is the metal work function, χ_S is the electron affinity of the semiconductor. In real Schottky contacts, the barrier height is affected by interfacial layers, surface states, defects and chemical reactions which also determine the quality of the contacts.

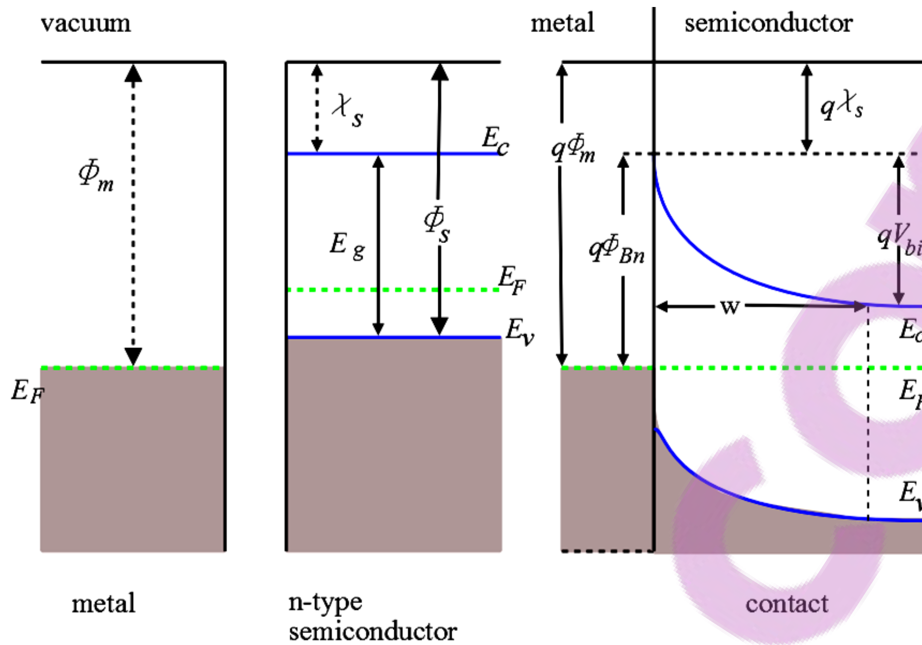

Figure. 2.3: Flatband diagram of a metal/n-type semiconductor contact at equilibrium. Redrawn after ref [14]

2.5.3.1 Current-voltage (IV) measurements

The current voltage technique offers a good method for evaluating the quality of a Schottky contact by determining the reverse and forward current that flows through the device under different biasing conditions. This enables us to deduce the current transport mechanisms that dominate the conduction process within the device. Figures of merit which include barrier height, ideality factor and series resistance can also be obtained.

In this section, a couple of IV characteristics obtained from metal/ZnO structures are presented and discussed. This section aims to point out some of the factors affecting the quality of the contacts, in as much as the fabrication techniques and material processing steps are concerned.

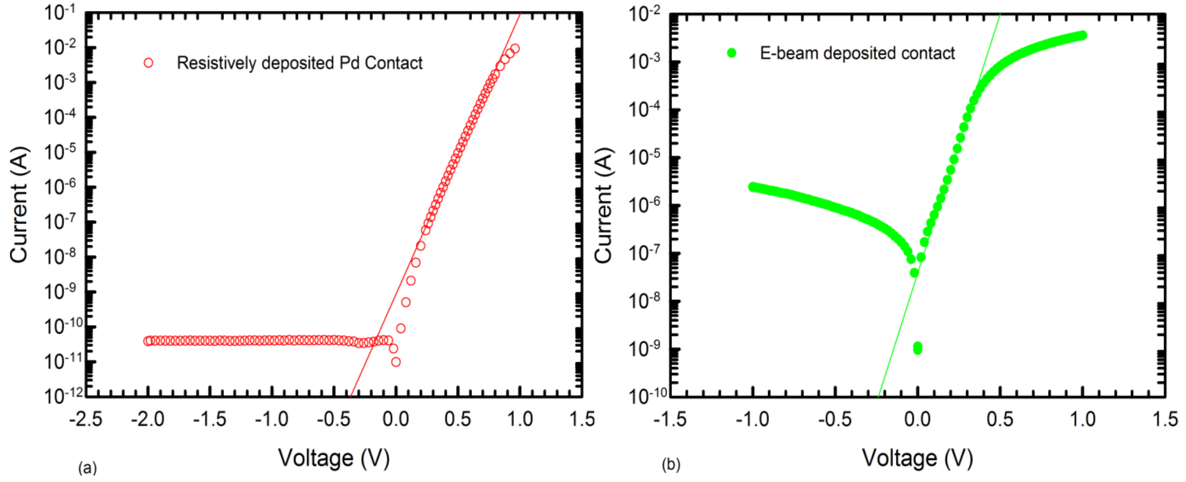

Figure 2.4: *A semi-logarithmic IV characteristics of (a) resistively deposited and (b) e-beam deposited Pd/ZnO Schottky contacts obtained at 298 K from the best selected contacts.*

A typical current-voltage characteristic of metal/ZnO Schottky contacts is illustrated in Figure 2.4. These contacts show a strong dependence on the contact fabrication technique used since the material processing steps are the same. The straight line shows the linear fit to the data by assuming a pure thermionic emission model. The current flowing through the metal semiconductor contact is given by [48],

$$I = I_S \exp\left[\frac{q(V - IR_s)}{nkT}\right]\left\{1 - \exp\left[\frac{q(V - IR_s)}{kT}\right]\right\} \qquad (2.2)$$

where V is the applied voltage, R_s is the series resistance, n is the ideality factor, I_s is the saturation current. From the straight line fit shown in Figure 2.4, the ideality factor and the barrier height can be deduced. The ideality factor is obtained from the gradient, as,

$$n = \frac{q}{2.3kT \cdot [d(\ln I)/dV]} = \frac{q}{2.3mkT} \qquad (2.3)$$

where m is the gradient of the straight line. The saturation current is obtained as the intercept to the $\ln I$ axis at $V = 0$ as,

$$I_S = AA^*T^2 \exp\left(-\frac{q\phi_B}{kT}\right) \qquad (2.4)$$

where A is the Schottky contact cross-sectional area, A^* is the Richardson constant, T is the temperature in Kelvin, k is the Boltzmann constant and ϕ_B is the barrier height calculated as

$$\phi_B = \frac{kT}{q} \ln\left[\frac{AA^*T^2}{I_S}\right] \qquad (2.5)$$

Deviations from linearity at high applied voltage are due to the effects of series resistance. The resistive evaporation technique proves to produce better quality contacts with very low leakage currents and a higher degree of rectification compared to the e-beam deposited contacts. Table 2.3 shows some of the parameters extracted from the resistively deposited and e-beam deposited contacts by fitting the data to a pure thermionic emission model.

Table 2.3: *Values of ideality factor n, Schottky barrier height (SBH), series resistance, saturation current I_s and the degree of rectification for the resistively and electron-beam (E-beam) deposited Pd contacts.*

Deposition Technique	Ideality factor, *n*	SBH (eV)	Series Resistance (Ω)	Saturation current, I_s (A)	*Degree of rectification
Resistive	1.56 ± 0.05	0.75 ± 0.01	21 ± 5	$(1.1 \pm 0.4)\times10^{-10}$	9
E-Beam	1.7 ± 0.2	0.60 ± 0.02	143 ± 7	$(8.4 \pm 5)\times10^{-8}$	3

*Refers to the ratio of the forward current measure at 1.0 V to the reverse current at 1.0 V

From the average parameters shown in Table 2.3, it can be observed that the resistive technique yields better quality contacts compared to the e-beam technique. However, it must be noted that in some cases it is not a matter of choice for one not to use the latter technique. To fabricate contacts which are thermally stable at high temperatures, high melting point metals must be used. Since these metals cannot be resistively evaporated, other techniques e.g. sputter deposition or e-beam deposition must be employed. IV characteristics of some chosen high melting point metals are shown in Figure 2.5.

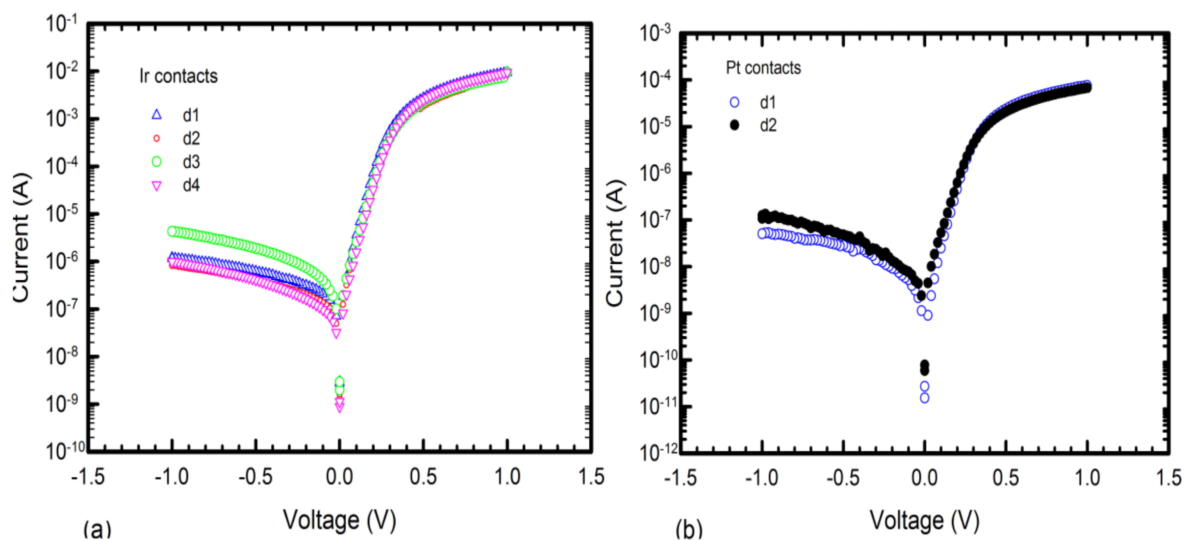

Figure 2.5: Semi-logarithmic IV characteristics of (a) Ir and (b) Pt contacts obtained at 298 K.

BESTPFE.COM
List of research project topics and materials

Table 2.4: *Values of ideality factor n, Schottky barrier height (SBH), series resistance, saturation current I_s and the degree of rectification for the electron-beam (e-beam) deposited Ir and Pt contacts.*

Metal	Ideality factor, n	SBH (eV)	Series Resistance (Ω)	Saturation current, I_s (A)	Degree of rectification
Ir	1.29 ± 0.02	0.567±0.003	77 ± 7	$(1.2 \pm 0.1)\times10^{-7}$	5
Pt	1.5 ± 0.1	0.67 ± 0.01	(9 ± 0.3))$\times10^{3}$	$(3 \pm 1)\times10^{-9}$	3

For all the characteristics presented in this chapter, the e-beam deposited contacts have poor quality contacts in terms of leakage current and lower orders of rectification compared to the resistively deposited contacts. This has been attributed to the damage caused by the ionized gas particles that impinge onto the sample causing damage to the surface. Since the filament is not a true point source of electrons; stray electrons originating from it and are not focused onto the metal can also impinge onto the sample [49].

Annealing of samples prior to contact fabrication and after fabrication also affects the quality of the contacts. This is because annealing can recover defects in crystals or can remove defects which in turn affect device operation. Figure 2.6 shows some IV characteristics of metal contacts fabricated on ZnO samples annealed at different temperatures. It must be mentioned that the ZnO samples were first annealed in Ar at different temperatures prior to contact fabrication. This is because annealing of the samples at elevated temperatures with the Schottky contacts fabricated would result in an ohmic behaviour as has been observed by Mtangi *et al*. [31] on Pd/ZnO structures annealed in Ar.

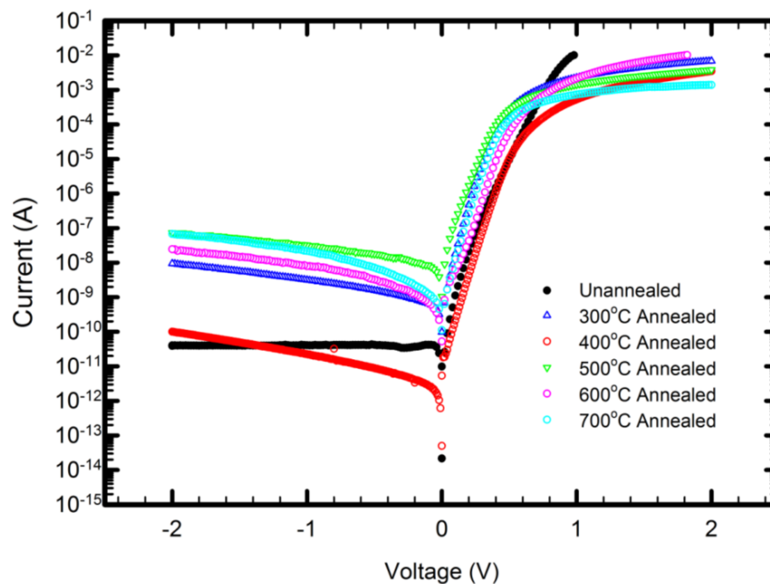

Figure 2.6: Semi-logarithmic IV plots of the Pd/ZnO devices obtained at 298 K.

The other reason for annealing the samples prior to contact fabrication is to avoid the modification of the depletion region of the metal semiconductor contact through in diffusion of the metal into the semiconductor or by vice-versa and also the formation of metal/Zn eutectics. It can be observed that the annealed contacts show an increased reverse current at -2.0 V as compared to the un-annealed contacts. A possible explanation for such an increase in reverse current could be the modification of the layer closer to the surface with annealing, which becomes highly conductive where the surface electrons can contribute to the current through surface conduction as has been suggested [38]. Another possibility is that, annealing can introduce subsurface and also deep level defects that can assist carriers in tunnelling through the barrier increasing the reverse current. Annealing of samples is significant as it can cause thermal decomposition of the ZnO surface (particularly in O_2) which can be used for surface electronic studies of the material [50].

Figure 2.7 shows the IV characteristics of Pt/ZnO Schottky contacts annealed in (a) Ar and (b) O_2, respectively.

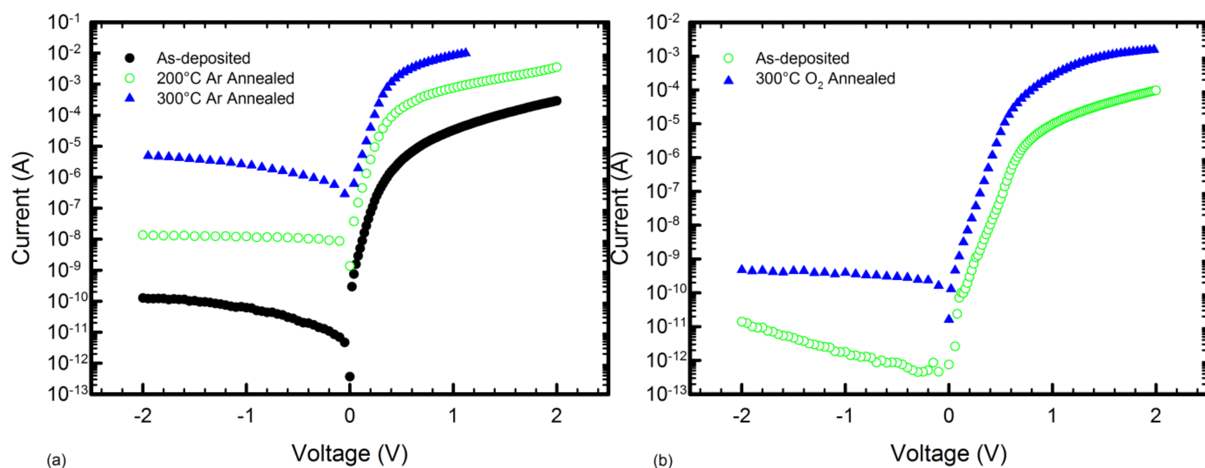

Figure 2.7: Semi-logarithmic IV characteristics of Pt/ZnO Schottky contacts annealed in (a) Ar and (b) oxygen ambient.

From these characteristics, an increase in reverse current is observed after annealing the contacts. The series resistance effects are also reduced. Interesting enough, for samples annealed prior to contact fabrication (Figure 2.6), the series resistance effects are increased. This is possibly due to some accumulation of surface adsorbents during annealing. For samples annealed with contacts fabricated (Figure 2.7), the decrease in series resistance can possibly due to the reduction in the concentration of surface and/or interface states density

because of the solid state reaction which might occur between the metal and semiconductor during annealing. The ideality factor, the series resistance and barrier height obtained from the best selected contacts are shown in Table 2.5.

Table 2.5: *Values of ideality factor, SBH, series resistance and degree of rectification obtained from the best selected Pt/ZnO contacts.*

Annealing ambient	Annealing Temperature (°C)	Ideality factor, n	SBH (eV)	Series Resistance (Ω)	Degree of rectification
------	----------	1.53	0.72	2.69k	7
Ar	200	1.50	0.62	0.48k	5
Ar	300	1.64	0.55	71	4
------	-------	2.14	0.82	11.8k	7
O_2	300	1.84	0.75	0.61k	6

The barrier height decreases with increase in annealing temperature as carriers can now easily cross over the barrier. The series resistance however is drastically reduced for the Ar annealed samples. The same is also observed for the O_2 annealed contacts. However, there is a decrease in the order of rectification with annealing. Thus annealing can also have an effect on the quality of contacts.

2.5.3.2 Capacitance-voltage (CV) measurements

An understanding of the impurity distribution in semiconductor material is essential in the fabrication of devices. The CV technique is ideal to help bring this understanding by analysing the depletion region of a semiconductor through the CV profiling method. This method makes use of the differential capacitance. Under reverse bias conditions, the width of the space charge region of a metal/semiconductor junction depends on the applied voltage. Superimposing a small ac signal upon dc bias results in a separation of negative charges from positive charges where the metal assumes more negative charge which induces a positive charge within the semiconductor region. This creates a region depleted of charge carriers called the depletion region. This junction resembles a parallel plate capacitor with the depletion region acting as a dielectric. A typical CV characteristic is shown in Figure 2.8.

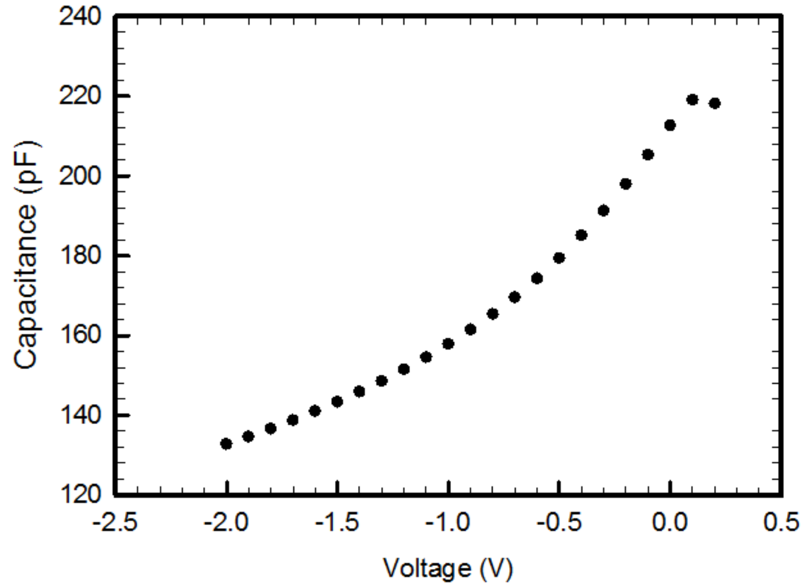

Figure 2.8: *Room temperature CV characteristics obtained from a Pd/ZnO Schottky contact annealed at 400°*C *in Ar.*

2.5.4 The Depletion layer

Based on the depletion width approximation, the semiconductor is assumed to be divided into two distinct regions. These are a layer closer to the interface which is completely depleted of charge carriers and an interior region of perfect charge neutrality in which no electric field exists. The charge density $\rho(x)$ in the depletion region where there are no electrons in the conduction band is given by qN_D. If the depletion width is w, the charge density in the semiconductor can be written as [47,51]:

$$\rho(x) = \begin{cases} qN_\mathrm{D} \text{ if } x \leq w \\ 0 \quad \text{if } x > w \end{cases} \tag{2.6}$$

where N_D is the dopant density and q is the electronic charge.

The existence of an electric field due to charge separation results in a potential difference to across the metal-semiconductor junction. The shape of the band edge profiles can be determined by solving Poisson's equation and applying the necessary boundary conditions. These boundary conditions are obtained from:

(a). the barrier height

(b). the electric field; considering it to be zero within the bulk of the semiconductor.

Taking x to be zero at the interface, $x = 0$ the boundary conditions can be written as $V(0) = V_d$

and $E(\infty) = 0$. The solution for the Poisson's equation can be written in one-dimension as

$$\frac{d^2V}{dx^2} = \frac{1}{\varepsilon_s}\rho(x) \tag{2.7}$$

where $\rho(x)$ is the total charge density in the semiconductor at a depth x and ε_s is the semiconductor permittivity. If $\rho(x)$ includes contributions from the valence band, conduction band, ionized donors and acceptors, the resulting equation becomes more complicated and would require numerical methods to solve it. Making use of the depletion width approximation, integrating equation (2.7) twice and applying the boundary conditions will give the depletion layer width as [42],

$$w = \sqrt{\frac{2\varepsilon_s V_d}{qN_D}} \tag{2.8}$$

Under an externally applied bias, V_a the depletion region is given by,

$$w = \sqrt{\frac{2\varepsilon_s}{qN_D}\left(V_{bi} - V_a - \frac{kT}{q}\right)} \tag{2.9}$$

The electric field in the semiconductor is also given by,

$$E(x) = -\frac{qN_D}{\varepsilon_s}(w - x) \tag{2.10}$$

The electrostatic potential can be obtained by integrating equation (2.10) as

$$V(x) = -\frac{qN_D}{\varepsilon_s}\left(wx - \frac{1}{2}x^2\right) \tag{2.11}$$

The space charge per unit area of the semiconductor, Q_{sc} is given by

$$Q_{sc} = qN_D w = \sqrt{2\varepsilon_s qN_D\left(V_{bi} - V_a - \frac{kT}{q}\right)} \tag{2.12}$$

If this is the amount by which the charge within the depletion width w changes due to a dc bias, then a differential or small signal capacitance is given by,

$$C = \frac{|\partial Q_{sc}|}{\partial V_a} = \sqrt{\frac{\varepsilon_s qN_D}{2(V_{bi} - V_a - kT/q)}} = \frac{\varepsilon_s A}{w} \tag{2.13}$$

This can be written in the form,

$$\frac{1}{C^2} = \frac{2(V_{\text{bi}} - V_a - kT/q)}{\varepsilon_{\text{s}} A^2 q N_{\text{D}}} \tag{2.14}$$

A plot of $1/C^2$ *versus* V_a yields a straight line where the doping density, N_{D} can be calculated from the gradient provided N_{D} is constant throughout the depletion region. The built-in-voltage, V_{bi} is obtained from the voltage intercept. The net doping density is given by;

$$N_{\text{D}} = \frac{2}{A^2 q \varepsilon_{\text{s}}} \left\{ -\frac{1}{d(1/C^2)/dV} \right\} \tag{2.15}$$

Figure 2.9 shows a typical $1/C^2$ *versus* V_a plot.

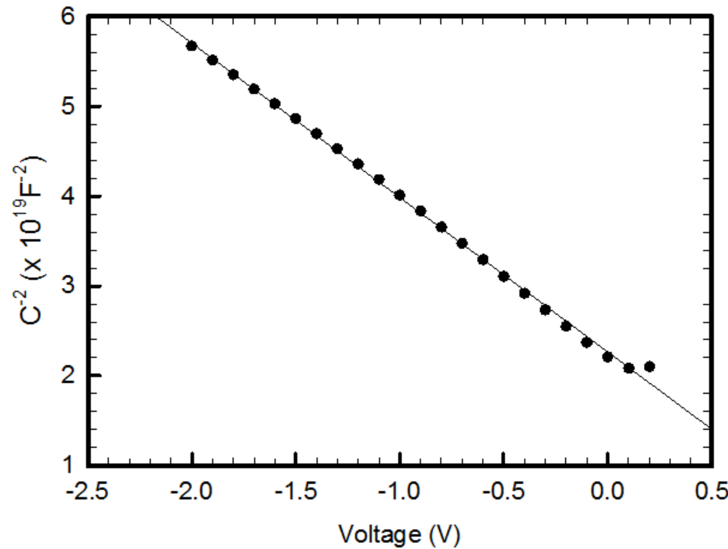

Figure 2.9: Room temperature $1/C^2$ versus V_a characteristics obtained from a Pd/ZnO Schottky contact annealed at 400°C in Ar.

By varying the depletion region width through changing the applied voltage and measuring the capacitance, the net doping profile of the semiconductor can be obtained using equation (2.14). A typical net doping profile is shown in Figure 2.10.

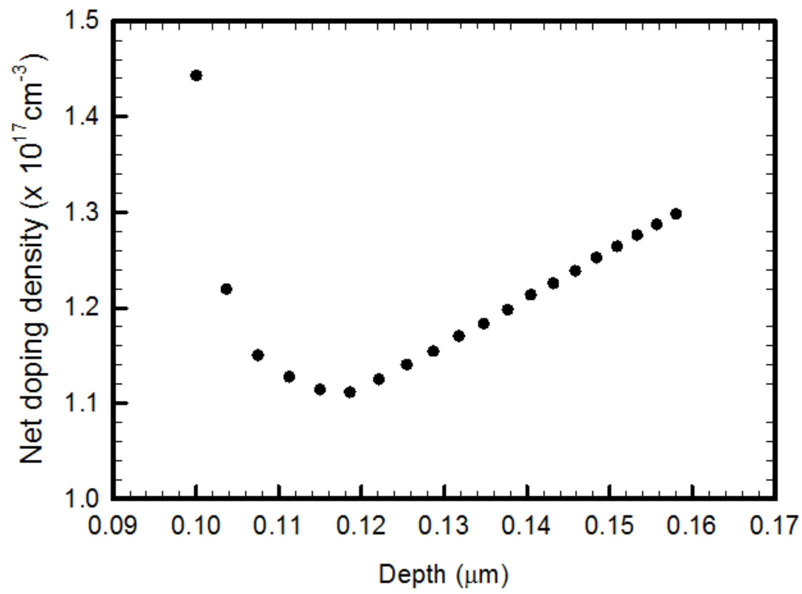

Figure 2.10: *Net doping profile of the Pd/ZnO Schottky contact annealed at 400°*C *in Ar*.

As indicated in Figure 2.10, 400°C Ar annealed ZnO sample reveal a concentration gradient towards the surface. A region up to a depth of 0.16 μm below the metal/semiconductor interface has been probed at a reverse bias of 2.0 V.

Summary

From Table 2.2 and the *IV* characteristics presented in this chapter, it can be mentioned that processing steps prior to Schottky contact fabrication and the deposition techniques used affect the quality of the semiconductor devices. This can be explained by the fact that different cleaning techniques and chemicals react differently with ZnO. As a result of these differences, different surface morphologies, surface states, subsurface defects and chemical reactions influence the quality of the contacts formed. These factors cause a variation of barrier heights obtained from metal/ZnO structures even with the same metal being used. This shows that Schottky contact fabrication on ZnO still needs further investigations to fully understand these structures. The barrier heights determined from these particular contacts vary from 0.55 – 0.96 eV. The resistive evaporation technique produces contacts with very low reverse currents and higher degrees of rectification. E-beam deposition as well as annealing of the samples prior to contact fabrication seems to increase the reverse current that flows through the contacts. The possible explanation for such behaviour could be an introduction of defects within semiconductor material that can promote recombination and other current transport mechanisms other than pure thermionic emission. An investigation into the defects that might have been possibly introduced into the semiconductor material during fabrication and processing is to be performed using DLTS and high resolution Laplace DLTS.

Bestpfe.com

References

1. D. C. Look, J. W. Hemsky and J. R. Sizelove, Phys. Rev. Lett. **82**, 2552 (1999)
2. C. G. Van de Walle, Phys. Rev. Lett. **85**, 5 (2000)
3. E. C. Lee, Y-S. Kim, Y.-G. Jin, and K. J. Chang, Phys. Rev. B **64**, 085120 (2001)
4. S. B. Zhang, S. H. Wei, and A. Zunger, Phys. Rev. B, **63**, 075205 (2001)
5. A. F. Kohan, G. Ceder, D. Morgan, and C. G. Van de Walle, Phys. Rev. B **61**, 15019 (2000)
6. F. Oba et al., J. Appl. Phys. **90**, 824 (2001)
7. A. Janotti and C. G Van de Walle, Appl. Phys. Lett. **87**, 122102 (2005)
8. D. G. Thomas, and J. J. Lander, J. Chem. Phys. **25**, 1136 (1956)
9. E. V. Lavrov, J. Weber, F. Borrnert, C. G. Van de Walle, and R. Helbig, Phys. Rev. B. **66**, 165205 (2002)
10. B. Yao, D. Z. Shen, Z. Z. Zhang, X. H. Wang, Z. P. Wei, B. H. Li, Y. M. Lv, X. W. Fan, L. X. Guan, G. Z. Xing, C. X. Cong, and Y. P. Xie, J. Appl. Phys. **99**, 123510 (2006)
11. M. D. McCluskey and S. J. Jokela, J. Appl. Phys. **106**, 071101 (2009)
12. U. Özgür, A comprehensive review of ZnO materials and devices, J. Appl. Phys. **98**, 41301 (2005)
13. C. Jagadish and J. Pearton, Zinc Oxide Bulk, Thin Films and Nanostructures Processing, Properties and Applications, Elsevier, Oxford, UK, Amsterdam, Netherlands, (2006)
14. W. Mtangi, MSc Dissertation, University of Pretoria 2009
15. R.B. Heller, J. McGannon, and A.H. Weber. Precision determination of the lattice constants of zinc oxide. J. Appl. Phys., **21**, 1283 (1950)
16. R.K. Swank. Surface properties of II-VI compounds. Phys. Rev. **153**, 844 (1967)
17. W.S. Baer. Faraday rotation in ZnO: Determination of the electron effective mass. Phys. Rev. **154**, 785 (1967)
18. M. Oshikiri, Y. Imanaka, F. Aryasetiawana and G. Kido, Physica B, **298**, 472 (2001)
19. N. Ashkenov, B.N. Mbenkum, C. Bundesmann, V. Riede, M. Lorenz, D. Spemann, E.M. Kaidashev, A. Kasic, M. Schubert, M. Grundmann, G.Wagner, H. Neumann, V. Darakchieva, H. Arwin, and B. Monemar. Infrared dielectric functions and phonon modes of high-quality ZnO films. J. Appl. Phys. **93**, 127 (2003)
20. M. Schmidt, PhD Thesis, Leipzig University, 2012
21. http://www.cermetinc.com/materials/crystal_growth.htm, 24/07/2012
22. A. Y. Polyakov, N. B. Smirnov, E. A. Kozhukhova, V. I. Vdovin, K. Ip, Y. W. Heo, D. P.

Norton, and S. J. Pearton, Appl. Phys. Lett. **83**, 1575 (2003)

23. M. W. Allen, M. M. Alkaisi, and S. M. Durbin, Appl. Phys. Lett. **89**, 103520 (2006)
24. W. Mtangi, F. D. Auret, P. J. Janse van Rensburg, S. M. M. Coelho, M. J. Legodi, J. M. Nel, W. E. Meyer, and A. Chawanda, Appl. Phys. Lett. **110**, 094504 (2011)
25. U. Grossner, S. Gabrielsen, T. M. Børseth, J. Grillenberger, A. Y. Kuznetsov, and B. G. Svensson, Appl. Phys. Lett. **85**, 2259 (2004)
26. Q. L. Gu, C. K. Cheung, C. C. Ling, A. M. C. Ng, A. B. Djuriıˆsiæ, L. W. Lu, X. D. Chen, S. Fung, C. D. Beling, and H. C. Ong, J. Appl. Phys. **103**, 093706 (2008)
27. A. Nakamura, and J. Temmyo, J. Appl. Phys. **109**, 093517 (2011)
28. H. Endo, M. Sugibuchi, K. Takahashi, S. Goto, S. Sugimura, K. Hane, and Y. Kashiwaba, Appl. Phys. Lett. **90**, 121906 (2007)
29. H. von. Wenckstern, E. M. Kaidashev, M. Lorenz, H. Hochmuth, G. Biehne, J. Lenzner, V. Gottschalch, R. Pickenhain, and M. Grundmann, Appl. Phys. Lett. **84**, 79 (2004)
30. L. J. Brillson, H. L. Mosbacker, M. J. Hetzer, Y. Strzhemechny, G. H. Jessen, D. C. Look, G. Cantwell, J. Zhang, and J. J. Song, Appl. Phys. Lett. **90**, 102116 (2007)
31. W. Mtangi, F.D. Auret, A. Chawanda, P.J. Janse van Rensburg, S.M.M. Coelho, J.M. Nel, M. Diale, L. van Schalkwyk, C. Nyamhere, Materials Science and Engineering B **177**, 180 (2012)
32. R. Schifano, E. V. Monakhov, U. Grossner, and B. G. Svensson, Appl. Phys. Lett. **91**, 193507 (2007)
33. C. H. Tsai, S.-X. Lin, C. I. Hung, C. C. Liu, and M. P. Houng, J. Appl. Phys. **106**, 093702 (2009).
34. S. H. Kim, H. K. Kim, and T. Y. Seong, Appl. Phys. Lett. **86**, 112101 (2005)
35. W. Mtangi, F.D. Auret, C. Nyamhere, P.J. Janse van Rensburg, M. Diale, A. Chawanda, Phys. B. **404**, 1092 (2009)
36. D.C. Look, Superlattices Microstruct., **42**, 284 (2007)
37. G.H. Kassier, M. Hayes, F.D. Auret, M. Diale, B.G. Svensson, Phys. Status Solidi C **5**, 569 (2008)
38. W. Mtangi, J.M. Nel, F.D. Auret, A. Chawanda, M. Diale and C. Nyamhere, Physica B **407**, 1624 (2011)
39. D. C. Look, G. C. Farlow, P Reunchan, S Limpijumnong, S. B. Zhang, and K. Nordlund, Phys. Rev. Lett. **95**, 225502 (2005)
40. H. von Wenckstern, G. Biehne, M. Lorenz, M. Grundmann, F. D. Auret, W. E. Meyer, P. J. Janse van Rensburg, M. Hayes, J. M. Nel, J. Kor. Phys. Soc. **53**, 5 (2008)

BEST PFE.COM
List of research project topics and materials

41. V. Quemener, L. Vines, E. V. Monakhov, B. G. Svensson, Int. J. Appl. Ceram. Technol. **8**, 5 1017 (2011)
42. D. M. Hofmann, D. Pfisterer, J. Sann, B. K. Meyer, R. Tena-Zaera, V. Munoz-Sanjose, T. Frank, G. Pensl, Appl. Phys. A. **88**, 147 (2007)
43. Y. Natsume, H. Sakata, Mat. In Electronics **12**, 87 (2001)
44. Y. H. Shin, M. D. Kim, J. E. Oh, M. S. Han, S. G. Kim, K. S. Chung, J. Kor. Phys. Soc. **53**, 5 (2008)
45. K. Abe, M. Miura, M. Oiwa, J. Vac. Sci. Technol. A, **29**, 3 (2011)
46. C. Jagadish and J. Pearton, Zinc Oxide Bulk, Thin Films and Nanostructures Processing, Properties and Applications, Elservier, Oxford, UK, Amsterdam, Netherlands (2006)
47. S. M. Sze Physics of semiconductor devices, 2nd Edn. Wiley, New York (1981).
48. E. H. Rhoderick and R. H. Williams, Metal-semiconductor Contacts (Oxford University Press, Oxford 1988)
49. F. D. Auret, S. A. Goodman, G. Myburg, F. K. Koschnick, J.-M. Spaeth, B. Beaumont, and P. Gibart, Physica B, **273**, 84 (1999)
50. L. J. Brillson and Y. Lu, J. Appl. Phys. **109**, 121301 (2011)
51. B. G. Streetman, Solid State Electronic Devices, 5th Ed, Prentice Hall, New Jersey (2000)

Chapter 3

Defects in semiconductors

3.1 Introduction

A perfect crystal is one in which the arrangement of the atoms within the crystal lattice is periodic, i.e. each atom occupies its designated lattice site and there are no missing atoms. However, in real life situations, it is difficult to obtain a perfect crystal. Imperfections in crystal lattices are due to several reasons. These include the growth technique and growth conditions. During crystal growth, some impurities can be unintentionally introduced into the material, thereby disturbing the orientation of the host atoms. Others can also be intentionally introduced during doping. Post-growth annealing of semiconductor material can also introduce or remove defects. Imperfections in semiconductor material can among others be due to missing atoms, impurities, dopants and others and also atoms occupying the wrong positions which disturb the crystal structure.

These imperfections, also referred to as "*defects*" may introduce electronic states in the bandgap of semiconductor material. The electronic states introduced by these defects can be classified as shallow and deep levels depending on their location relative to the conduction or valence band edge. If a defect transition level is positioned in such a way that it can be thermally ionized at room temperature or at the device operating temperature, it is referred to as a shallow level [1]. With particular reference to ZnO, shallow level defects include hydrogen, aluminium, group I related metals, just to mention a few, which are located just a few tens of milli-electron volts below the bottom of the conduction band minimum. Deep level defects include, the oxygen vacancy, Zn vacancy, which are said to be located within the middle third of the semiconductor band gap and are usually unionized at room temperature. Defects in semiconductors can be divided into two main categories, i.e. point defects and extended defects.

Defects in ZnO are often detrimental to device operation as they tend to modify the electrical and optical properties of devices. They also affect the realization of p-type doping and also the fabrication of UV light emitting devices due to their self-compensation behaviour. In some cases, defects can also be important, especially in the fabrication of devices with high switching speeds.

In this particular chapter, an outline of the defects that can be found in semiconductor material is given. This discussion is going to focus mainly on the type, structure and properties with special reference to n-type ZnO.

3.2 Point defects

Many semiconductors possess large concentrations of defects in the form of point defects (intrinsic and extrinsic). As their name states, "point defects" cause some perturbation of the lattice within a localized area about a lattice site involving only a few nearest neighbours. The formation energy of point defects depends on the growth or annealing conditions [2,3]. Point defects are classified as intrinsic and extrinsic lattice defects. Intrinsic lattice defects are those that are caused by the missing of the host atoms (vacancies), interstitials, and host atoms occupying the wrong lattice sites (antisites). Extrinsic point defects are those due to impurity atoms occupying substitutional or interstitial sites. In II-VI compound semiconductors, the intrinsic lattice point defects of interest are vacancies and host interstitials [4] associated with each of the two sublattices. These point defects affect semiconductor material in many ways as they often control background doping, minority carrier lifetime and luminescence efficiency [1,5]. Point defects can cause device degradation as they also assist the diffusion mechanisms that are involved during growth and processing of the material. As much as doping is concerned, native point defects which act as donors in ZnO may self-compensate the introduced acceptors [6,7]. This poses a challenge in the realization of p-type ZnO. Native point defects have also been believed to play a major role in the high levels of unintentional n-type conductivity observed in ZnO [7]. An understanding of the nature and origins of these point defects in ZnO is essential. The native point defects in ZnO include the oxygen vacancy, zinc vacancy, oxygen antisites, zinc antisites, oxygen interstitials and zinc interstitials. Extrinsic point defects include hydrogen and other impurities introduced during growth e.g. group III related elements. The following sections are going to give a brief outline of some of the intrinsic point defects and hydrogen in ZnO.

3.2.1 The Oxygen vacancy

ZnO occurs naturally as n-type, whose conductivity has been attributed to native point defects particularly the oxygen vacancy and some other impurities which act as shallow donors [8, 9, 10,11,12,13]. However, the contribution to the n-type conductivity of ZnO by oxygen vacancies is still an issue under debate. First principles calculations by Janotti *et al.* [3] predicted that the oxygen vacancy V_O, if isolated is a deep donor and assumes the neutral charge state when the Fermi level is near the conduction band minimum, hence it is not responsible for the n-type conductivity in ZnO even though it has lowest formation energy among all the defects that behave as donors [3, 7]. The electronic structure of the oxygen vacancy comprises of four Zn dangling bonds (sp^3 hybrids) and two electrons. The dangling bonds combine forming a fully symmetric state, a_1 in the band gap and three almost degenerate states in the conduction band [7]. In the neutral state, the a_1 is filled (doubly occupied) leaving the three states in the conduction band empty. Each of the four Zn dangling bonds, contribute 1/2 electron to form the neutral state of the oxygen vacancy. The oxygen vacancy has three possible charge states, i.e. the neutral (V_O^0), +1(V_O^+) and +2 (V_O^{2+}), with the V_O^{2+} and V_O^0 being the stable states while the +1 charge is thermodynamically unstable [6]. The atomic structure of the oxygen vacancy in its three charge states is shown in Figure 3.1.

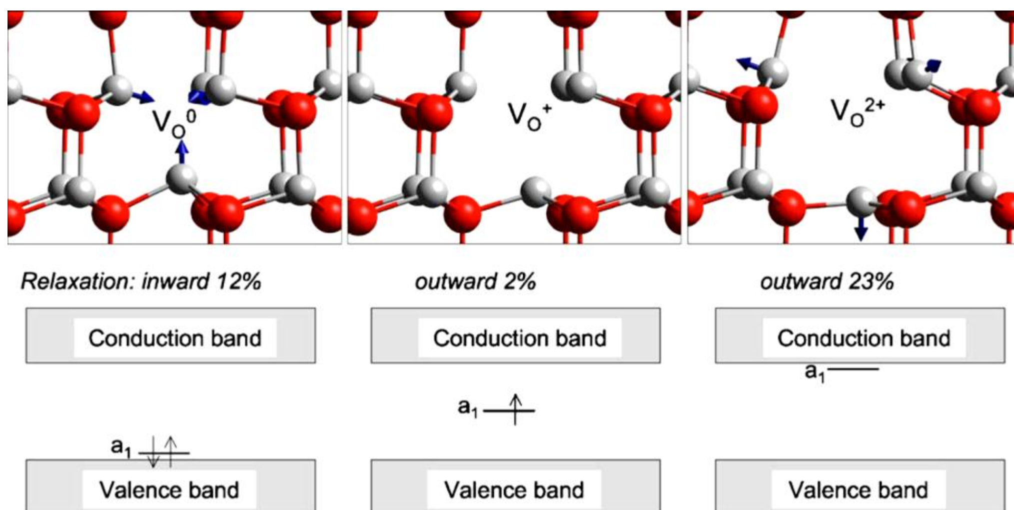

Figure. 3.1: The structure of the local atomic relaxations of the oxygen vacancy and the position of the a_1 state. Redrawn from reference [3]

As indicated in Figure 3.1, the local lattice relaxation of the oxygen vacancy determines the occupation of the a_1 state. In the neutral state, the four Zn atoms strongly relax towards the

vacancy by about 12% of the equilibrium Zn – O bond length. For the +1 state, the Zn atoms relax slightly outwards, while for the +2 charge state, the atoms relax further outwards. The large relaxation of the V_O^{2+} renders it low formation energy compared to the V_O^0 and V_O^+. This makes the 2+ charge state to be the energetically the most preferable state for the O vacancy [14]. Also the relaxation difference between the V_O^0 and V_O^+ reduces the formation energy of V_O^0 relative to the V_O^+. The relaxation differences in the charge states of the oxygen vacancy leads to the negative-*U* behaviour [15,3], which sees the V_O^+ being thermodynamically unstable.

Under p-type conditions, the Fermi level is near the top of the valence band. The oxygen vacancy is stable in the +2 charge state and has low formation energies; hence it acts as a compensation centre [7], affecting the formation of p-type ZnO. Since the formation energy of V_O is very low, at high temperature environments it can be easily formed [10] and is stable up to a temperature of 400°C [5]. It is therefore important to ensure that during growth or annealing of p-type ZnO, one must avoid incorporation of the V_O^{2+}. This can be achieved if the O-chemical potential approaches O-rich conditions and the Fermi level is kept away from the valence band minimum so as to suppress the formation of V_O^{2+} and reduce self-compensation effects.

3.2.2 The Zinc vacancy

Zn vacancies are double acceptors [6]. The acceptor behaviour of the Zn vacancies emanates from the fact that they are partially filled and hence can easily accept additional electrons. The electronic structure of a Zn vacancy is made up of dangling bonds from four oxygen atoms. These O dangling bonds combine to form a doubly charged symmetric state located deep in the valence band, and also introduce three partially occupied states in the bandgap of ZnO that lie very close to the valence band minimum. The Zn vacancy has three possible charge states, i.e. V_{Zn}^0, V_{Zn}^- and V_{Zn}^{2-}. Zn vacancies can easily be formed in n-type ZnO since their formation energy decreases with increase in Fermi level [1,7], hence V_{Zn}^{2-} can occur in high concentrations, acting as compensation centres and is the dominant compensating centre in ZnO [16, 17] .

In p-type ZnO, the formation energy of Zn vacancies is very high and thus can be found in very low concentrations. Formation of the Zn vacancy favours oxygen-rich conditions [7].

3.2.3 The Zinc interstitial

The n-type conductivity of ZnO is attributed to the native defects among which the Zn interstitial is suggested to be a candidate. It is a shallow donor estimated to lie at about 30 meV below the minimum of the conduction band [9]. The zinc interstitial occupies the octahedral interstitial site of the wurtzite structure [18,6] since it is stable at this particular position. Stability of the Zn_i is brought about by the fact that, at the tetrahedral site, it is situated at a distance of approximately $0.833d_0$ (where d_0 is the Zn – O bond length along the c axis) and has one Zn and one O as the nearest neighbours, while in the octahedral site, it is at a distance of approximately $1.07d_0$ and has three Zn and three O atoms as nearest neighbours [7]. Based on size considerations, the Zn interstitial is expected to be stable on the octahedral site because of less geometrical constraints. In ZnO, the Zn_i induces a state with two electrons above the conduction band minimum. The electrons are made available to the conduction band states forming the +2 charge state which is very stable. This behaviour makes the Zn interstitial a shallow donor. However under n-type conditions, the Zn interstitial is said to have high formation energy for Fermi level positions near the conduction band [6,14,1]. This property disqualifies it from being a most likely source of the n-type conductivity in n-type ZnO [14,1] since it exists in very low concentrations. Since the formation energy of the Zn_i^{2+} decreases when the Fermi level moves closer to the valence band maximum, the Zn_i becomes a likely source of compensation in p-type ZnO.

3.2.4 Negative-*U* and Metastability

As has been discussed in section 3.2.1, the oxygen vacancy has three charge states, the +2, +1 and the neutral state, with the +2 state having a low formation energy compared to the other two, while the +1 is thermodynamically unstable, a negative-*U* behaviour is predicted for the oxygen vacancy. This negative-*U* behaviour is brought about by the fact that the unstable +1 state always has higher energy than the +2 and the neutral state [15,1] for any position of the Fermi level in the band gap. With increase in Fermi level position, a transition is observed to occur from the +2 to the neutral charge state [19], which are the stable states. For n-type material, two electrons of the neutral oxygen vacancy are transferred to the conduction band upon optical excitation, which triggers a large lattice relaxation of the defect resulting in the +2 charge state being stable at energies above the neutral charge state [20]. Another

contributing factor to the negative-U behaviour of the oxygen vacancy is, the positively charged ion is readily ionized as opposed to the neutral state and the electron affinity for V_O^{2+} is high in energy than the V_O^{+} [15]. The negative-U behaviour of the oxygen vacancy has been observed using optical techniques. The positive charge state of the oxygen vacancy is detected using electron paramagnetic resonance, EPR experiments [21,22] and also optically detected Magnetic resonance (ODMR) experiments [23] and Optically Detected Electron Paramagnetic Resonance (ODEPR) experiments [22,4]. This negative-U behaviour of the oxygen vacancy results in defect metastability.

Defect Metastability

This refers to defects that can occur in more than one structural configuration for at least one charge state. Metastable defects have structural transformations between atomic configurations under specific device operation or measurement conditions [24]. These transformations can be significant in a way since they can modify the role of a defect in the optical and electrical behaviour of a material, provided they are reproducible. Controllable metastability in semiconductor material is essential for the fabrication of memory devices [4]. An important aspect of the metastable defects is the reversible cycling that occurs among the different atomic configurations within the semiconductor with changes in device operation conditions, or measurement conditions [24]. The charge state, optical excitation, strain and temperature, just to mention a few, are some of the properties that determine the relative populations of the defect configuration.

Consider a defect with two lattice configurations. This defect configuration can be viewed as two total energy wells whose configuration space is separated by a potential barrier [24]. The stable configuration is the one with the lowest total energy and hence contains the largest population at equilibrium. A coordinate configuration diagram is shown in Figure 3.2.

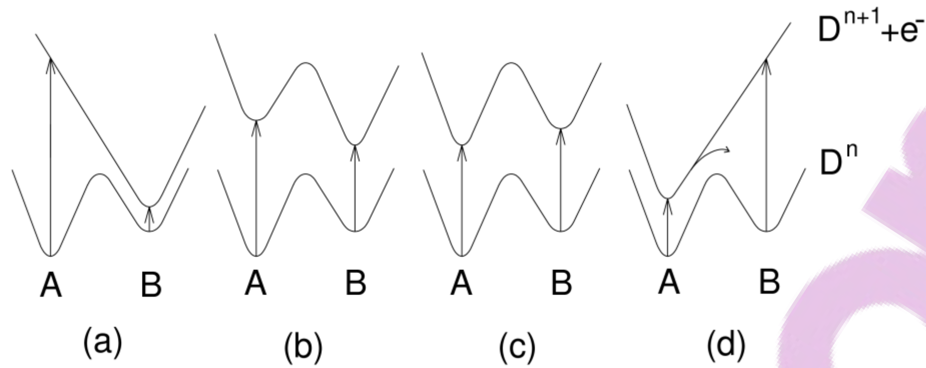

Figure. 3.2: Coordinate configuration diagram for a metastable defect with two lattice configurations. Redrawn from reference [4].

As illustrated in Figure 3.2, the lattice configuration marked A for a defect which has a charge state, n is the stable lattice configuration while B is the metastable configuration. In (a) and (d), large lattice relaxation cases are observed, where the ionized state $D^{n+1}+e^-$ has a local minimum only in one configuration. This is due to the fact that the large Stokes shifts are apparent, i.e. one of the configurations has very high optical ionization energies compared to the true ionization energy. 3.2 (b) and 3.2 (c) indicate ionized states which both have local minima, where the difference lies in which of A or B has the lowest energy configuration. Such cases are often referred to as small lattice relaxations since large Stokes shifts are absent.

In Figure 3.2(a) and 3.2(b), the stable configuration is not the same for the D^n and D^{n+1} charge states. A is the stable configuration in the D^n state while B is the stable configuration in the D^{n+1} charge state. This results in this particular defect being *bistable*. Its configuration can be altered by changing the charge state at a temperature at which the potential barriers can be overcome [4]. This is achieved by cooling the defect to below that temperature where it becomes frozen to a particular configuration where its properties can be determined. In Figure 3.2 (c) and (d), A is the stable configuration for both charge states. In a case where a single configuration is the only stable one for the two charge states, optical excitation or electrical injection can be used to establish thermal equilibrium distribution between the two near energy configurations in the ionized state.

DLTS can be used to detect the metastable configurations of a defect. Under equilibrium conditions, i.e. at non-zero temperature, the two configurations are occupied [24]. By measuring the DLTS peak heights, an estimate of the relative concentrations can be obtained.

Bestpfe.com

Adjusting the bias conditions of the sample can set the charge states of the defects [25]. If the temperature of the sample is varied, by cooling from a high temperature under reverse bias, the position of the Fermi level will be altered, where any defect state below the Fermi level will be filled. The same defect can be set in a different state by cooling under zero bias. If a control of the measurement conditions for the defect configurations is successfully managed, the reaction mechanisms, potential barrier heights, electrical and optical properties of individual defect structures can be determined.

3.3 Extended defects

Extended defects in semiconductors are usually identified as volume defects, surface defects, and line defects. Volume defects are viewed to be any volume that differs from the rest of the crystal in structure, composition, orientation and/or state variables [26] e.g. precipitates, second phase grains, and also grains in polycrystalline material. Surface defects are also defined to be free surfaces or interfaces between distinguishable volumes. These are usually a cause of surface conduction in bulk ZnO samples, with a free carrier concentration of about $(1 - 3) \times 10^{12} cm^{-2}$ [27, 28]. The effects of surface conduction are observed from the Hall effect measurements where the semiconductor can be treated as having two conducting channels [29, 30]. The first one being dominated by surface electrons whose effect is observed at low temperatures (freeze out region) while the other one is dominated by the bulk electrons, usually dominant at high temperatures, i.e. above the freeze out region. Surface conduction can be reduced by exposing the material to air due to possible adsorption of oxygen and/or changes in surface reconstruction [6]. Line defects are classified into different categories, namely *dislocations* and *disclinations* (also referred to as dislocations of rotation). Disclinations are usually observed in liquid crystals in which the rotational symmetry of crystals is violated.

3.3.1 Line defects

As has been mentioned in section 3.3, these types of defects fall into two different categories, namely *dislocations* and *disclinations*. They have three important characteristics [26] which are;

a. The defect formation energy decreases as the number of dimensions in which the defect extends is reduced. These formation energies are also large and hence easy to avoid or eliminate.
b. All of them are fundamentally related. Since all line defects are dislocations, a systematic treatment is possible because of their unity.
c. Dislocations are capable of interacting with all other types of defects and/or can also assist in generating other types of defects.

Dislocations can be explained as linear defects in which some of the atoms of the crystal lattice are misaligned [31]. The two basic types of dislocations are *edge* dislocations and *screw* dislocations. If a plane of atoms in the middle of a crystal is terminated, edge dislocations are formed. In order to have a perfectly ordered crystal structure on either side, adjacent planes bend around the edge of the terminating plane.

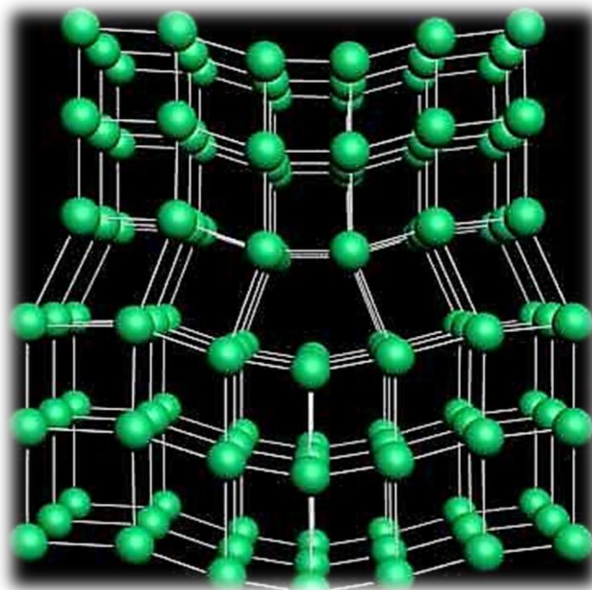

Figure 3.3: Lattice structure illustrating an edge dislocation within a semiconductor.

BESTPFE.COM
List of research project topics and materials

Screw dislocations can be viewed as a structure consisting of a helical path that is traced around the linear dislocation by the atomic planes in the crystal lattice. Such a structure is indicated in Figure 3.4.

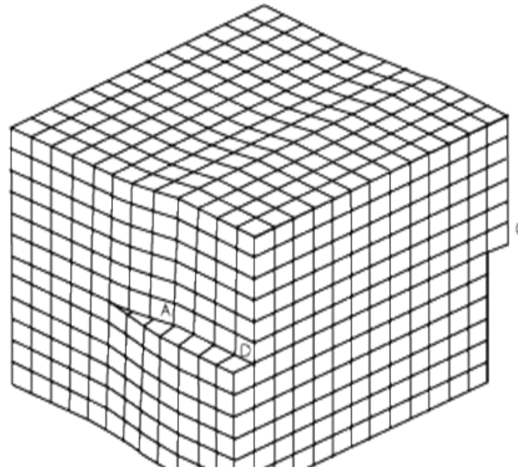

Figure 3.4: Lattice structure indicating a screw dislocation

Dislocations are negatively charged as has been observed from transmission electron microscopy by Muller *et al.* [32]. They affect the electrical properties of materials as they often contain many charges. In crystals, dislocations can also cause lattice distortions or strain and have also been proposed to account for the shear stresses above which single crystals of metals undergo permanent plastic deformation [26]. It has also been proposed that several luminescence peaks are related to extended defects which include dislocations [32]. In ZnO heteroepitaxial layers, threading dislocations with densities of approximately 10^9 cm^{-2} are usually observed [6]. These usually run along the c-axis in ZnO grown under O-rich conditions whereas for ZnO grown under Zn-rich conditions, it has been observed that the dislocations are inclined to 20° - 30° from the *c* axis [34].

In semiconductors, dislocations can be observed using DLTS by monitoring the emission process of charge carriers. Charge carriers can build up in a line and gradually start repelling accumulation of additional charges. This in turn reduces the effective capture cross section as the amount of accumulated charge increases, causing the emission of carriers to follow a non-exponential process [35].

References

1. A. Janotti and C. G. Van de Walle, Phys. Rev. Lett. B. **76**, 165202 (2007)
2. C. G. Van de Walle and J. Neugebauer, J. Appl. Phys. **95**, 3851 (2004)
3. A. Janotti and C. G. Van de Walle, Appl. Phys. Lett. **87**, 122102 (2005)
4. G. D. Watkins, Materials Science Forum, **38-41**, 39 (1989)
5. L. S Vlasenko and G. D. Watkins, Phys. Rev. Lett. B, **71**, 125210 (2005)
6. M. D. McCluskey and S. J. Jokela, Appl. Phys. Rev. **106**, 071101 (2009)
7. A. Janotti and C. G. Van de Walle, Rep. Prog. Phys. **72**, 126501 (2009)
8. Y. Natsume, H. Sakata, Mater. Chem. Phys. **78**, 170 (2002)
9. D.C. Look, J.W. Hemsky, J.R. Sizelove, Phys. Rev. Lett. **82**, 2552 (1999)
10. E. V. Lavrov, Physica B, **404**, 5079 (2009)
11. C. G. Van de Walle, Phys. Rev. Lett. **85**, 5 (2000)
12. F. A. Selim, M. H. Weber, D. Solodovnikov, and K. G. Lynn, Phys. Rev. Lett. **99**, 085502 (2007)
13. D. M. Hofmann *et al.*, Phys. Rev. Lett. **88**, 045504 (2002)
14. F. Oba, M. Choi, A. Togo and I. Tanaka, Sci. Technol. Adv. Mater. **12**, 034302 (2011)
15. C. H. Patterson, Phys. Rev. Lett. B, **74**, 144432 (2006)
16. F. Tuomitso, K. Saarinen, D. C. Look, G. C. Farlow, Phys. Rev. B. **72**, 085206 (2005)
17. F. Tuomitso, V. Ranki, K. Saarinen, D.C. Look, Phys. Rev. Lett. **91**, 205502 (2003)
18. P. Erhart and K. Albe, Appl. Phys. Lett. **88**, 201918 (2006)
19. Kohan, G. Ceder, D. Morgan, C.G. Van de Walle, Phys. Rev. Lett. B, **61**, 22 (2000)
20. D. Pfisterer, J. Sann, D. M. Hofmann, B. Meyer, T. Frank, G. Pensl, R. T. Zaera, J. Zuniga-Perez, C. M. Thomas, and V. Munoz-Sanjose, Phys. Stat. Sol. (c) 3, No. **4**, 997 (2006)
21. C.G. van de Walle, Physica B, **308**, 899 (2001)
22. L. S. Vlasenko, Appl. Magn. **39**, 103 (2010)
23. F. Leiter, H. Zhou, F. Hennecker, F. Hofstaetter, D. M. Hoffman, and B. K. Meyer, Physica B, **308**, 908 (2001)
24. L. J. Benton, Journal of Electronic Materials, **18**, 2 (1989)
25. L. J. Benton and M. Levinson, Defects in Semiconductors II eds. S. Mahajan and J. W. Corbett, (North Holland, New York, 1983) 95.
26. D. B. Holt, B. G. Yacobi, Extended defects in Semiconductors, Electronic properties, Device effects and structures (Cambridge University press 2007) ISBN 978-0-521-81934-3

27. O. Schmidt, P. Kiesel, C. G. Van de Walle, N. M. Johnson, J. Nause, and G. H. Döhler, Jpn. J. Appl. Phys., Part 1 **44**, 7271 (2005)
28. D. C. Look, H. L. Mosbacker, Y. M. Strzhemechny, and L. J. Brillson, Superlattices Microstruct. **38**, 406 (2005)
29. D.C. Look, B. Claflin, H.E. Smith, Appl. Phys. Lett. **92**, 122108 (2008)
30. D.C. Look, Superlattices Microstruct. **42**, 284 (2007)
31. J. P. Hirth and J. Lothe). *Theory of dislocations,* 2nd ed. (Krieger Pub Co. 1992) ISBN 0894646176
32. E. Muller, D. Gerthsen, P. Bruckner, F. Scholz, Th. Gruber, A. Waag, Phys. Rev. Lett. B, **73**, 245316 (2006)
33. H. Alves, D. Pfisterer, A. Zeuner, T. Riemann, J. Christen, D. M. Hofmann, and B. K. Meyer, Opt. Mater. **23**, 33 (2003)
34. A. Setiawan, Z. Vashaei, M. W. Cho, T. Yao, H. Kato, M. Sano, K. Miyamoto, I. Yonenaga, H. J. Ko, J. Appl. Phys. **96**, 7 (2004)
35. D.C. Look, Z-Q. Fang, A. Krtschil, and A. Krost, phys. stat. sol. (c) 2, No. **3**, 1039– 1046 (2005)

Chapter 4

Defect characterization

4.1 Introduction

Defects in semiconductors can be detrimental to devices particularly in photovoltaic applications as they tend to reduce the minority carrier lifetime [1] and at times enhance the operation of devices by increasing the switching speeds by acting as recombination centres [2]. It is therefore essential to have a technique for characterizing defects in semiconductors. Electrically active defects in semiconductor crystals have different characteristics, depending on the location of their energy states relative to the conduction or valence band edge. These defects can be classified as shallow level defects and deep level defects. Shallow level defects are those whose energy levels are within a few tens of milli-electron volts from the respective band edges [3] which can be easily characterized by surface sensitive techniques, e.g. the Hall effect technique. Deep level defects typically reside within the middle two thirds of the semiconductor band gap. The energy required to remove an electron or hole from such a trap to the valence or conduction band is much larger than the characteristic energy, kT. This makes it more difficult to detect these defects with the Hall effect technique. Thus it is essential to have a technique to characterize deep level defects in semiconductors. Deep level transient spectroscopy DLTS is an ideal technique for characterizing electrically active deep level defects in semiconductors.

4.2 Emission and capture of carriers from deep levels

Existence of intrinsic defects in semiconductors poses a serious challenge to the semiconductor industry as defects tend to modify the electrical and optical properties and at times influence doping, e.g. in ZnO where it is still a challenge in obtaining p-type material.

Fabrication and development of efficient semiconductor devices requires a good knowledge of the identity, nature and properties of the deep levels that are native and also those that can be introduced in semiconductor material. Based on application, defects can affect device operation and at times can enhance the operation of devices.

The behaviour of these defects as either traps or recombination centres in devices is vital. High concentrations of deep level defects lead to the deterioration of solar cell parameters by increasing saturation current and decreasing the lifetime of the minority carriers and hence the efficiency [1]. On the other hand, deep level defects can improve the switching speeds of semiconductor switches. Deep level defects almost always change their electron/hole occupancy via carrier transitions between the levels and the bands [4]. A deep level can capture an electron from the conduction band. The electron can stay there until it is re-emitted back to the conduction band. Such a defect level is referred to as an electron trap.

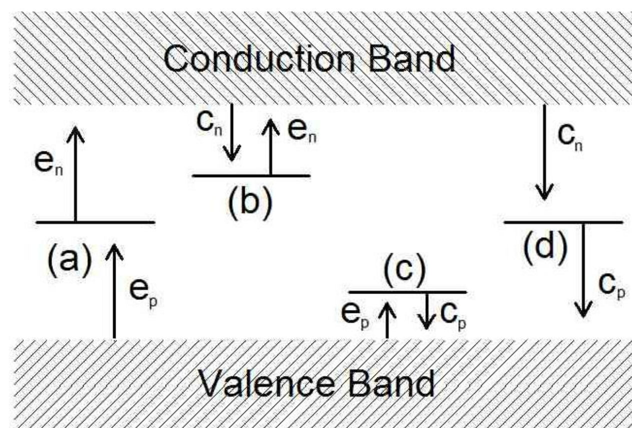

Figure 4.1: Schematic representation of carrier transitions between deep states and the valence- and conduction bands redrawn from ref [4]. *Transfer between deep levels is neglected. The effective direction of electron transfer for both electron and hole processes is indicated by the arrows.*

Figure 4.1 illustrates the four most common processes for the transition of electrons and holes between the deep levels and the bands. The transition marked (a) indicates carrier generation, (b) shows electron trapping, (c) indicates hole trapping and (d) shows the recombination process. In the determination of defect state properties, it is usually electron trapping and hole trapping that are used to derive deep state properties [4]. Electron capture and emission most likely occurs for an empty deep level when the electron capture rate c_n from the conduction band is much larger than the hole capture rate c_p from the valence band, i.e. $c_n >> c_p$.

The kinetics of charge transfer between the deep levels and the bands which are ultimately used to analyse deep level experimental data, are fully described by the Shockley-Read-Hall

(SRH) model [5, 6]. This model is developed by assuming thermal (or near thermal) equilibrium. Detection of deep level defects is experimentally performed by introducing perturbations to the carrier density or to the occupancy of the deep states involved and monitoring the return to equilibrium.

Let us consider an electron that is captured and emitted by a deep level. The electron capture rate is given by

$$c_{\mathrm{n}} = \sigma_{\mathrm{n}} \langle v_{\mathrm{n}} \rangle n \tag{4.1}$$

where σ_{n} is the defect's electron capture cross-section, n is the electron concentration in the conduction band, and $\langle v_{\mathrm{n}} \rangle$ is the average thermal velocity of free electrons given by

$$\langle v_{\mathrm{n}} \rangle = \sqrt{3kT/m^*} \tag{4.2}$$

where m^* is the electron effective mass, k is the Boltzmann constant and T is the temperature in Kelvin.

As a function of temperature, the electron emission rate is given by

$$e_{\mathrm{n}}(T) = \sigma_{\mathrm{n}} \langle v_{\mathrm{n}} \rangle \frac{g_0}{g_1} N_{\mathrm{C}} \exp\left(-\frac{E_{\mathrm{C}} - E_{\mathrm{t}}}{kT}\right) \tag{4.3}$$

where $E_{\mathrm{C}} - E_{\mathrm{t}}$ is the energy separation of the deep state from the conduction band, $g_0$and g_1 are the degeneracy terms referring to the state before and after electron emission, respectively. σ_{n} is the electron capture cross section which is assumed to be temperature independent in this case. N_C is the effective density of states in the conduction band given by,

$$N_{\mathrm{C}} = 2M_{\mathrm{C}} \left(\frac{2\pi m^* kT}{h^2}\right)^{3/2} \tag{4.4}$$

M_C is the number of conduction band minima and h is Planck's constant.

From equation (4.4), the product $\langle v_{\mathrm{n}} \rangle N_{\mathrm{C}}$ has a T^2 dependence. Determining e_{n} as a function of temperature, an Arrhenius plot of log (e_{n}/T^2) versus $1/T$ must produce a straight line whose slope will give the energy difference $E_{\mathrm{C}} - E_{\mathrm{t}}$ while the intercept (at $1/T = 0$) gives the apparent capture cross section $\sigma_{\mathrm{n}a}$, assuming $\sigma_{\mathrm{n}a}$ is temperature independent.

If we allow the capture cross-section to vary with temperature, it will take the form [7],

$$\sigma(T) = \sigma_{\infty} \exp\left(-\frac{\Delta E_{\sigma}}{kT}\right) \tag{4.5}$$

where σ_{∞} is the capture cross-section extrapolated to $T = \infty$ and ΔE_{σ} is the thermal activation energy of the capture cross-section (i.e. the thermal barrier for carrier capture). The possible causes of the temperature dependence of the capture cross-section are the multiphonon capture into deep levels [7]. The temperature dependence of the capture cross-section can be determined from the plot of log $\sigma(T)$ versus $1/T$ where ΔE_{σ} can be obtained from the slope

and σ_∞ can be obtained after extrapolation to $T = \infty$. For a deep level defect whose capture cross section is temperature dependent, its activation energy E_a is identified with $(E_\mathrm{C} - E_\mathrm{t}) + \Delta E_\sigma$. The energy level of the trap is not directly obtained and also the identification only holds if $(E_\mathrm{C} - E_\mathrm{t})$ is temperature independent. Thus for a trap whose capture cross-section is temperature dependent, the thermal emission rate is given by,

$$e_\mathrm{n}(T) = \sigma_\mathrm{n}\langle v_\mathrm{n}\rangle \frac{g_0}{g_1} N_\mathrm{C}\exp\left(-\frac{(E_\mathrm{C} - E_\mathrm{t}) + \Delta E_\sigma}{kT}\right) \qquad (4.6)$$

where ΔE_σ is the thermal activation energy of the capture cross-section. Thus the thermal activation energy for emission of an electron to the conduction band is given by

$$\Delta E_a = (E_\mathrm{C} - E_\mathrm{t}) + \Delta E_\sigma \qquad (4.7)$$

Equation 4.7 indicates that the thermal activation energy has two components: (1) the energy difference between the bottom of the conduction band and the trap level, and (2) the thermal activation energy of the capture cross-section, as illustrated in Figure 4.2.

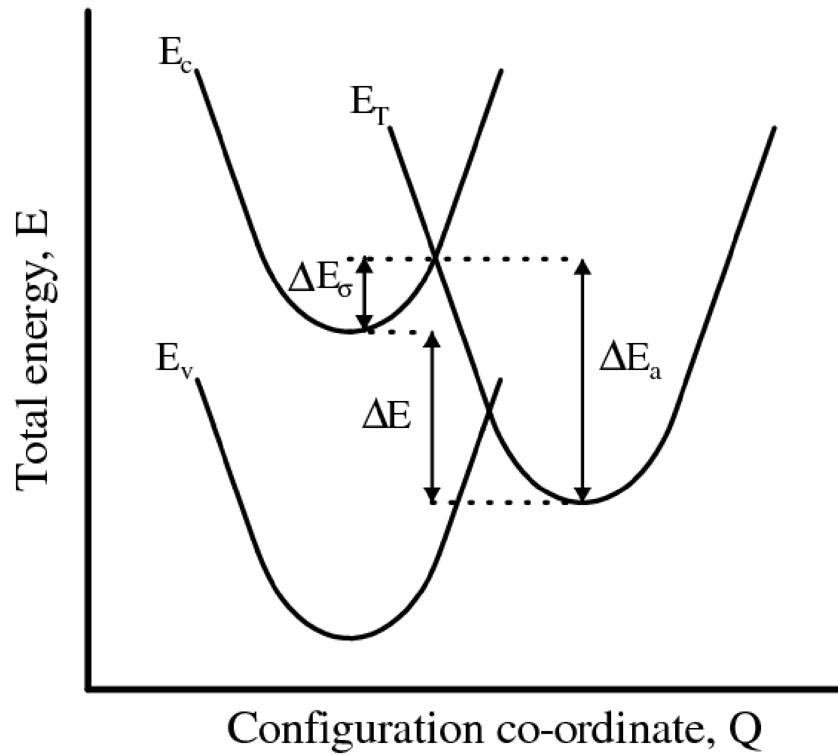

Figure 4.2: Co-ordinate configuration (CC) diagram depicting the energy level of a defect level below the conduction band, ΔE $(= E_\mathrm{C} - E_\mathrm{t})$, the thermal activation energy of the capture cross-section, ΔE_σ, and the total energy an electron requires to escape from the trap level to the conduction band, ΔE_a .

The commonly used parameter for characterizing deep levels is the activation energy for thermal emission [2]. The physical parameter $E_\mathrm{T} = E_\mathrm{C} - E_\mathrm{t}$ is the Gibbs free energy:

$$E_{\mathrm{T}} = \Delta H - T\Delta S \qquad (4.8)$$

where ΔH and ΔS are the changes in enthalpy and entropy due to the change in charge state of the level. Substituting equation (4.8) into (4.6) yields,

$$e_{\mathrm{n}}(T) = \sigma_{\mathrm{n}}\langle v_{\mathrm{n}}\rangle \frac{g_0}{g_1} N_{\mathrm{C}} \exp\left(\frac{\Delta S}{k}\right) \exp\left(-\frac{\Delta H}{kT}\right) \qquad (4.9)$$

This implies that, the slope of the Arrhenius plot gives the enthalpy of the deep level, and not the free energy, which can only be determined from optical measurements [8,9]. Hence, one must be careful when comparing energies derived from thermal emission measurements with other methods [4].

4.3 Deep level transient spectroscopy, DLTS

DLTS is a high-frequency capacitance thermal scanning technique used for observing a wide variety of traps in semiconductors [10]. This is achieved by probing the depletion region of an ordinary p-n junction, a Schottky diode, or a MOS device structure. The measurement process uses the change in the capacitance transient associated with thermal emission of charge carriers from deep levels to thermal equilibrium after an initial non-equilibrium condition in the space charge region. This technique is capable of revealing the nature of a trap by either a positive peak (majority carrier trap) or a negative peak (minority carrier trap) on a flat baseline as a function of temperature. DLTS is very sensitive, rapid and easy to analyse [10]. It can uniquely determine the position of a peak in temperature using the thermal emission properties of the trap, which one can use to determine the activation energy and the capture cross-section of the trap. In addition, this technique has the ability to identify the concentration profiles of the deep levels.

In this section, the main focus of the discussion is based on how the technique is employed with particular reference to the depletion region of a Schottky diode.

Consider the width of the depletion region of a metal semiconductor contact discussed in Chapter 2, given by,

$$w = \sqrt{\frac{2\varepsilon_{\mathrm{s}}(V_{\mathrm{bi}} - V_a)}{qN_{\mathrm{D}}}} \qquad (4.10)$$

where ε_{s} is the semiconductor permittivity, V_{bi} is the built in potential of the junction, V_a is the externally applied voltage, q is the electronic charge, and N_{D} is the density of the ionized

Bestore.com

impurities due to dopants and other defects with levels in the bandgap. The junction capacitance is now given by,

$$C = \frac{\varepsilon_s A}{w} = A\sqrt{\frac{q\varepsilon_s N_D}{2(V_{bi} - V_a)}} \tag{4.11}$$

where A is the cross-sectional area of the junction. From equation (4.10) and (4.11), altering the concentration of electrons or holes trapped at deep levels, by thermally or optically stimulated emission results in a change in the junction capacitance. The same change in the junction capacitance with the temperature dependence of N_D at a constant applied voltage forms the basis of capacitance-based DLTS [2].

During the formation of a metal/semiconductor contact, a region depleted of charge carriers is formed. This region is assumed to be formed within the semiconductor. According to the depletion width approximation, the semiconductor is now divided into two distinct regions, a layer that is entirely depleted of carriers (directly below the metal) and an interior region (bulk) of perfect charge neutrality, and in which no electric field exists. Assume that the semiconductor contains a low concentration of defects that cause a deep electron trap E_T shown in Figure 4.3. This deep level is assumed to be empty in the depletion region and filled in the bulk of the semiconductor. There exist a region λ within the depletion region that extends from the bulk (depletion region edge), where the deep level intersects the Fermi level. In this region, the deep level is also filled under equilibrium and zero bias conditions, since it also lies below the Fermi level.

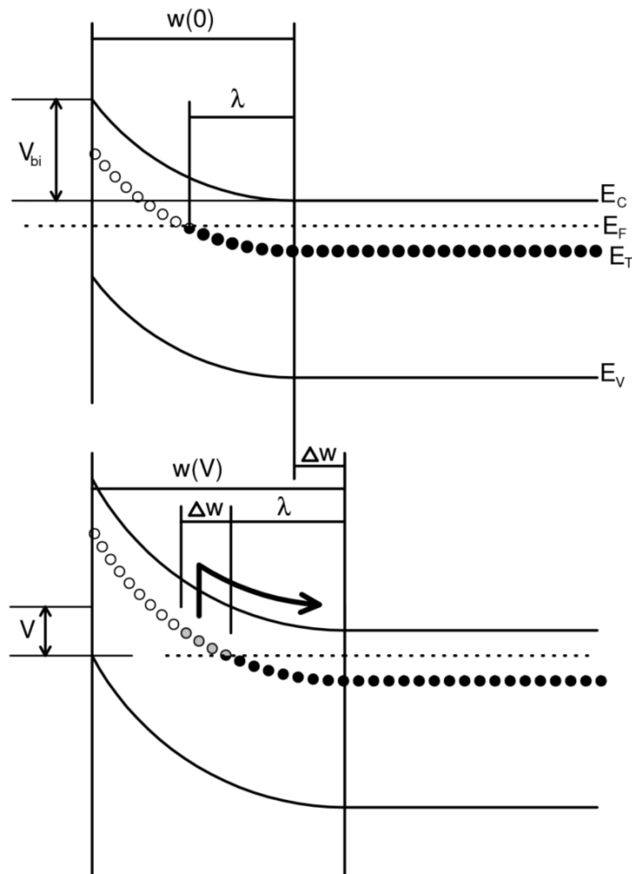

Figure 4.3: Filling (top) and subsequent emission (bottom) of electrons from a deep level in the depletion region, assuming a constant Fermi level. In the top diagram, the filling of the defect during the filling pulse is indicated. It must be noted that because of band bending and defect level depth, the defect level is filled to a depth λ shallower than the depletion region edge. After the filling pulse, the depletion region increases by an amount Δw [11].

Applying a quiescent reverse bias V_a results in an increase in the depletion region width, which in turn alters the occupancy of the space charge region since some of the deep level traps in the depletion region are now filled. The charge density in the depletion region decreases resulting in a decrease in capacitance [11].

A schematic representation of the capture and emission of carriers is shown in Figure. 4.4.

BESTPFE.COM
List of research project topics and materials

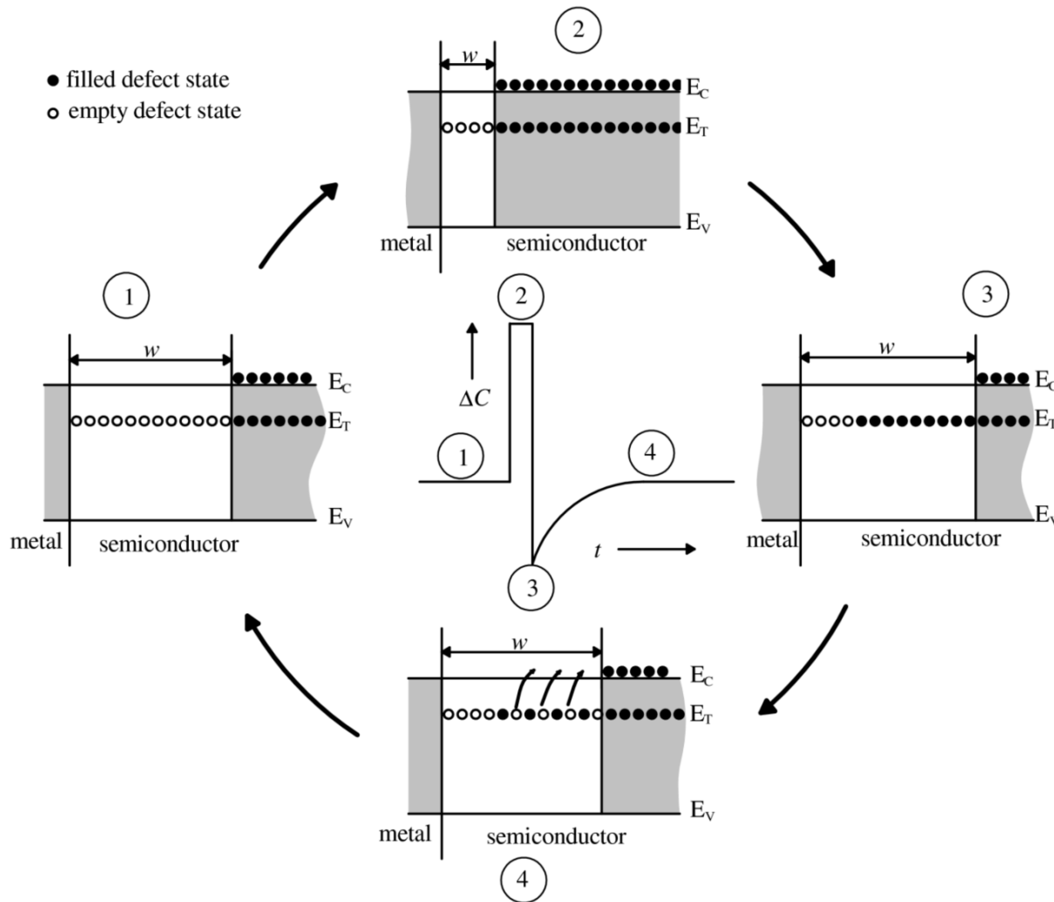

Figure. 4.4: Variation of depletion width and trap occupancy of an electron trap in an n-type semiconductor for a DLTS reverse bias and filling pulse. (1) *shows the equilibrium condition under reverse bias, while* (2) *indicates the change after a filling pulse has been applied.* (3) *and* (4) *indicate the situation at a time t after removing the filling pulse. The resulting capacitance transient is shown in the centre. Redrawn from ref* [2].

If the applied voltage is reduced, by applying a positive going pulse, the depletion width is reduced (2), allowing electrons to be trapped at the deep levels. At this stage, it is assumed that the filling pulse width is long enough to allow all the empty levels to completely fill up. This results in an increase in capacitance since the depletion width will be reduced. After removing the pulse (3), the filled states within the depletion region, above the Fermi level start emitting carriers with a characteristic rate into the conduction band where they are instantaneously swept away by the junction electric field (4). This thermal emission of the trapped electrons where the junction electric field sweeps them instantaneously into the conduction band is taken to be the majority carrier capacitance transient [2].

During experiments, the electron emission rate is determined from the time dependence of the capacitance transient. The density of the occupied traps at time t after removing the filling pulse is given by [2],

$$N(t) = N_{\mathrm{T}}\exp(-e_{\mathrm{n}}t) \tag{4.12}$$

where e_{n} is the thermal emission rate and N_{T} is the trap concentration assuming all the traps were initially filled. For $N_{\mathrm{T}} \ll N_{\mathrm{D}}$, the junction capacitance can be expressed as a time dependent function given by,

$$C(t) = C_0 - \Delta C_0\exp(-e_{\mathrm{n}}t) \tag{4.13}$$

where C_0 is the equilibrium reverse bias voltage capacitance and ΔC_0 is a change in capacitance observed immediately after removing the pulse.

4.3.1 DLTS Concepts

DLTS is a highly sensitive capacitance or current measurement technique with a good transient response. It is also a spectroscopic technique that is capable of resolving signals due to different traps from each other. Due to the above-mentioned features, amongst others, the DLTS principle of operation lies in the processing of capacitance transients obtained after a repeated pulsing sequence. It is also capable of setting an emission rate window such that the measurement apparatus only responds when it sees a transient whose rate falls within its window. During temperature scanning, since the thermal emission process is strongly dependent on temperature, the peak positions of the observed spectra shift to higher temperatures for higher emission rates and to lower temperatures for lower emission rates allowing a unique determination of these positions by using the rate window thermal scan. Initially, DLTS used a dual-gate average (double boxcar) for precise determination of the emission rate window and for signal averaging, enhancing the signal to noise ratio. This averaging helps in the detection of low concentration traps. Besides the fact that there is no lower limit on the rate window, it is ideal to work with rate windows above $1\mathrm{s}^{-1}$. This is because the thermal scan time is long, so below the $1\mathrm{s}^{-1}$ rate window, performing signal averaging would require an exceptionally longer time [10]. Figure 4.5 shows how the double boxcar technique is used to select a rate window.

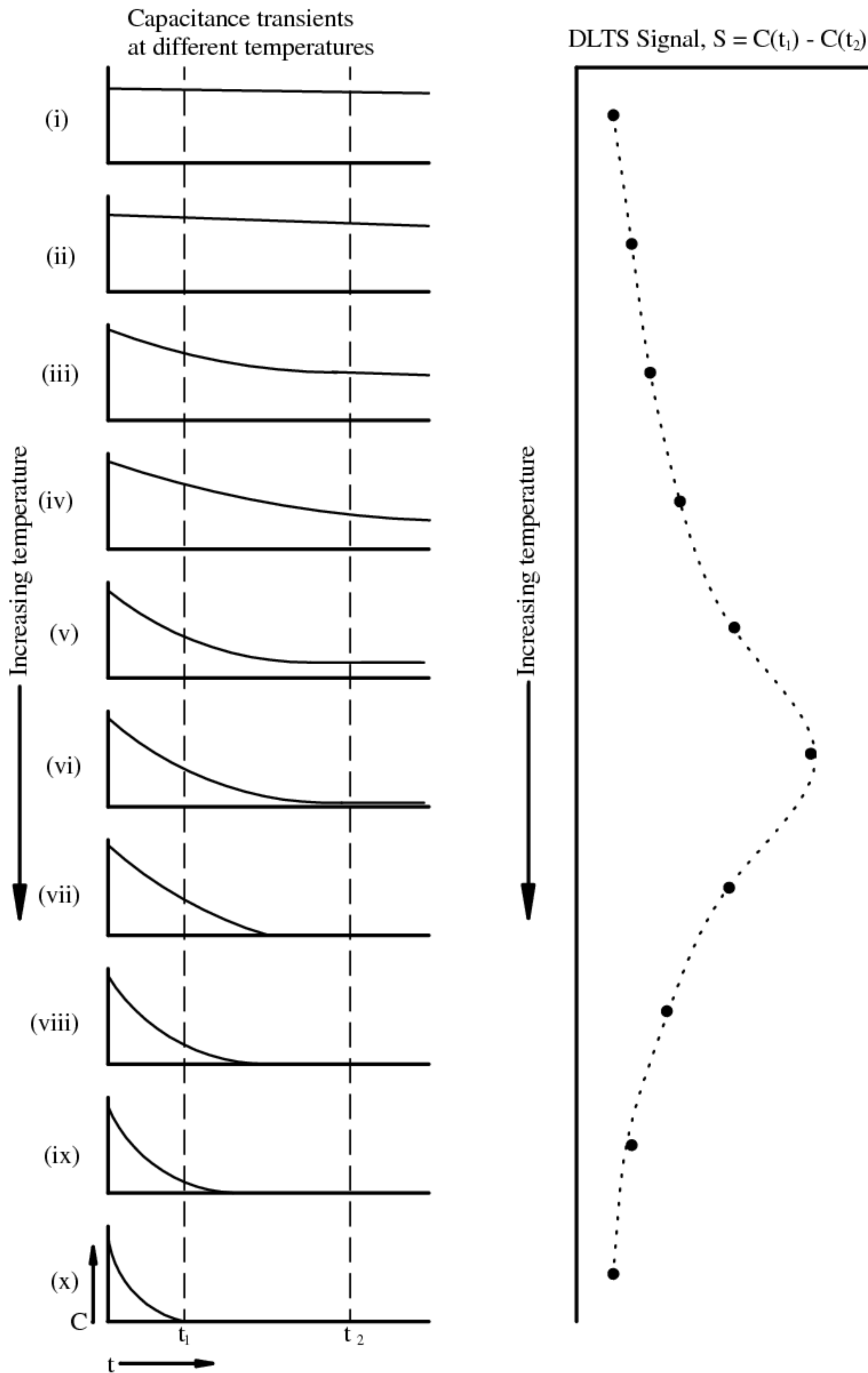

Figure 4.5: The change in the shape of a DLTS transient with increasing temperature (*left*) *and the DLTS signal obtained from the transients as a function of sample temperature* (*right*). *Redrawn from ref* [11].

Transient signals shown on the left hand side of Figure 4.5 are fed through the double boxcar with pre-set times, t_1 and t_2. The average difference between the capacitances at t_1, $C(t_1)$ and at t_2, $C(t_2)$ are plotted as a function of temperature as shown on the right hand-side of Figure 4.5. The rate window for the DLTS thermal scan is determined by the values of t_1 and t_2. As indicated in Figure 4.5, the capacitance difference changes as a function of temperature, i.e. it increases until it reaches a maximum (peak) and then it starts decreasing from either side of the peak. The peak is formed only when the decay constant τ falls within the order of $t_2 - t_1$. The value of τ at the maximum of the $C(t_2) - C(t_1)$ vs T for a particular trap, $\tau_{\max}$ can be related to the gate positions t_1 and t_2. This is achieved by normalizing the DLTS signal given in Fig 4.5 to obtain $S(T)$ defined as,

$$S(T) = [C(t_1) - C(t_2)]/\Delta C(0) \tag{4.14}$$

where $\Delta C(0)$ is the capacitance due to the pulse change at $t = 0$. For exponential transients,

$$S(T) = [\exp(-t_1/\tau)] - [\exp(-t_2/\tau)] \tag{4.15}$$

which can also be written as

$$S(T) = \exp(-t_1/\tau)[1 - \exp(-\Delta t/\tau)] \tag{4.16}$$

where $\Delta t = t_2 - t_1$. Thus the relationship between $\tau_{\max}$, t_1 and t_2 can be obtained by differentiating $S(T)$ with respect to τ and equating the result to zero:

$$\tau_{\max} = \frac{t_1 - t_2}{\ln\left(\frac{t_1}{t_2}\right)} \tag{4.17}$$

Thus the emission rate of the peak of a DLTS spectra obtained from a thermal scan can be precisely and uniquely determined. Performing a thermal scan with many different rate windows enables one to identify the peak positions and the temperatures at which they occur. This information can then be used to calculate the activation enthalpy and apparent capture cross-section as illustrated in Figure. 4.6.

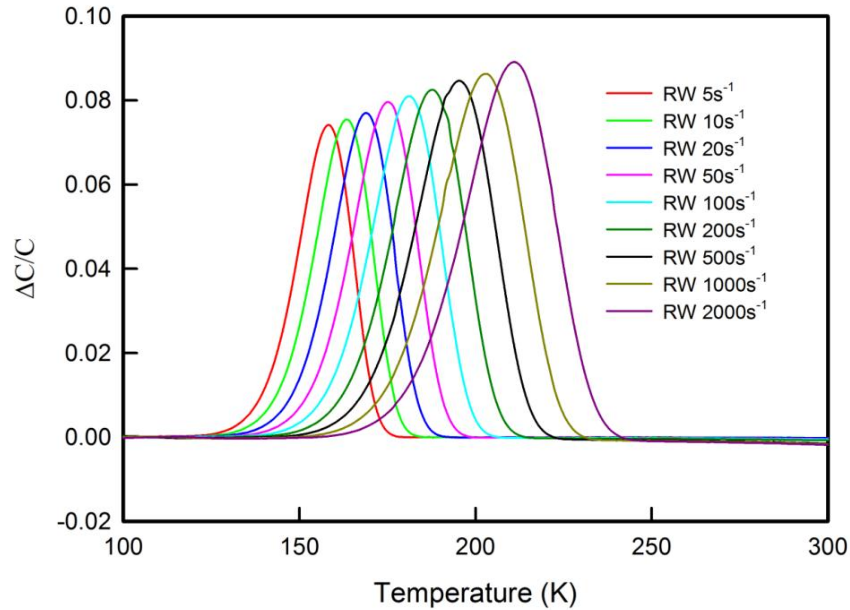

Figure 4.6: (a) Normalized DLTS spectra of the E3 peak in ZnO annealed at 500°C in vacuum to demonstrate how different rate windows can be used to plot an Arrhenius plot shown in Figure 4.6 (b). These spectra were recorded at a quiescent reverse bias of 2.0 V, filling pulse of 0.30 V and pulse width of 2ms.

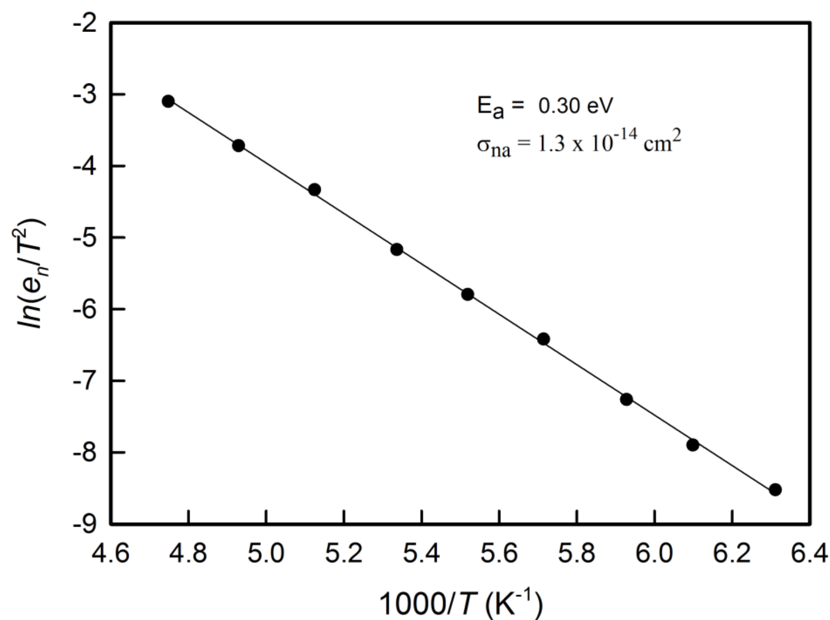

Figure 4.6: (b). Arrhenius plots of the E3 peak obtained using different rate windows indicated in Figure 4.6 (a).

4.3.2 Peak height dependence on rate window frequency

As can be observed in Figure 4.6 (a), the heights of the normalized DLTS peaks seem to depend on RW, i.e. the slower the rate window, the smaller the DLTS peak height. This variation has often been attributed to some peculiar characteristics of the traps under investigation, which include broadening of the trap activation energy resulting in non-exponential capacitance transients caused by field dependent electron emission, amphoteric behaviour of the deep levels [12] and temperature dependence of the capture cross-section [13]. Cavalcoli *et al*. [14] suggested and demonstrated the variation of the peak height due to the presence of a coulombic repulsive barrier associated with the defect under investigation. Rockett and Peaker [15] rule out the dependence of the peak height on non-exponential capacitance transients and suggest it to be rather related to the change in shape of the Debye tail of carriers which spill into the depletion region from the neutral bulk region, with both reverse bias and temperature. A study of the effects of varying the reverse bias conditions on the behaviour of the E3 peak is shown in Figure 4.7(a) and (b).

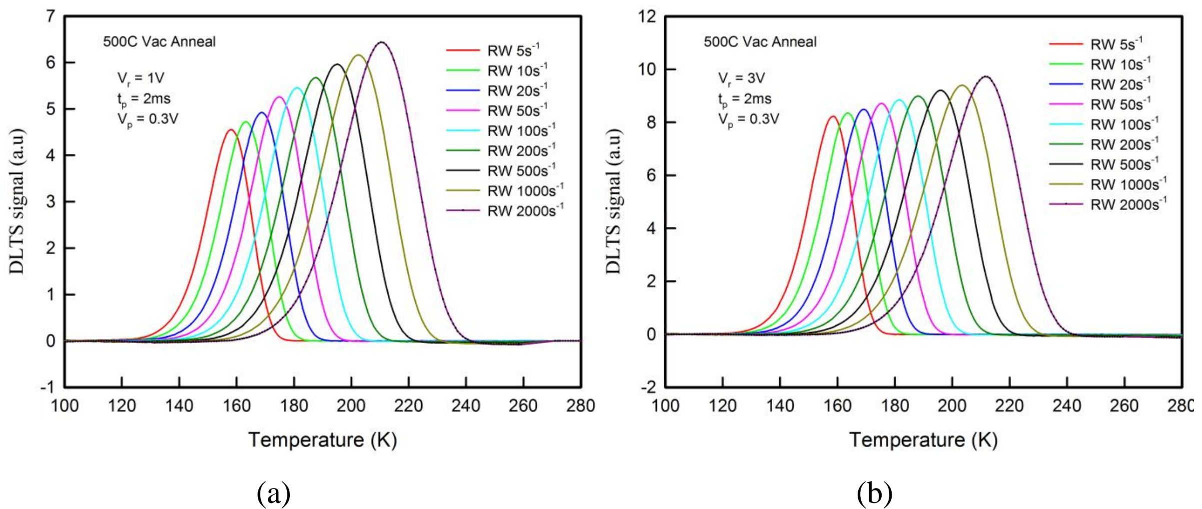

Figure 4.7: DLTS spectra of the E3 peak determined at (a) 1.0 V reverse bias and (b) 3.0 V reverse bias to illustrate the effect of reverse bias conditions on the variation of peak height with rate window.

The peak height variations still show a very strong dependence on emission rates. This indicates that the large peak variations observed in the E3 peak with large and small reverse bias conditions, which suggest field enhanced emission effects are not involved in any important way as has been suggested by Zhao *et al.*[16]. At high temperatures the variation in peak height is expected as the Debye tail penetration into the depletion region is also greater.

Zhao *et al.*[16] however suggest that the variation of the peak height is expected to occur if there is a large temperature dependence of the carrier capture cross section.

4.3.3 Temperature dependence of the capture cross-section

DLTS is a good technique for the determination of the trap thermal activation energy. However, the use of this technique is not sufficient since the determination of thermal capture parameters by DLTS is through an indirect process that reduces the accuracy [17]. Since the capture barrier is usually determined from the temperature dependence of the capture cross section and the available free-majority carriers, there is a high uncertainty associated with the actual shape of the filling pulses when the width is reduced. For pulses with short widths, the captured charge becomes difficult to determine and thus the capture coefficient is often underestimated [17].

However DLTS can be used to address this problem. This is achievable if one performs emission DLTS scans using different filling pulse widths. Saturation filling pulse conditions have to be determined first by using a longer filling pulse width. Once these conditions have been obtained, constant width filling pulses have to be selected to assure partial trap recharge. Figure 4.8 shows the normalized DLTS spectra for the E3 peak obtained under different filling pulse widths.

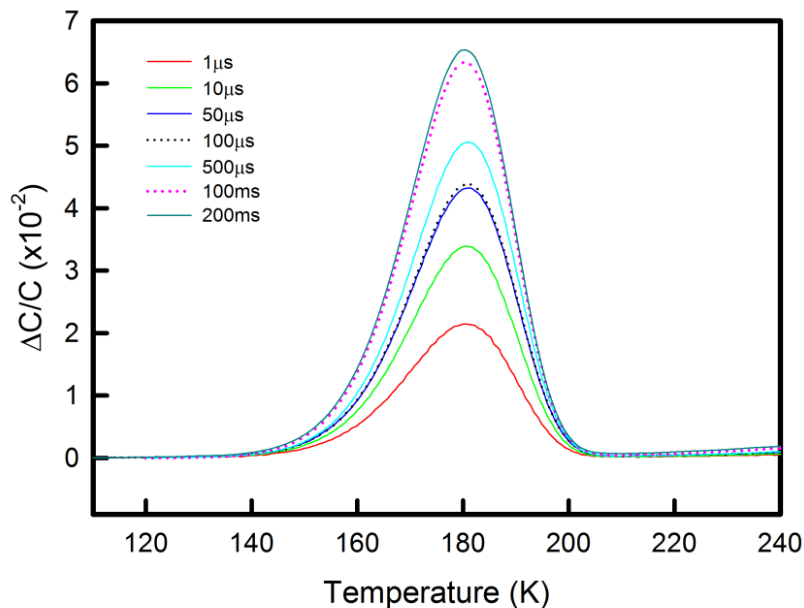

Figure 4.8: Normalized DLTS spectra of the E3 peak measured at different filling pulse widths. The spectra were recorded at a reverse bias of 2.0 V, pulse height of 0 V and rate window of 100 s^{-1}.

It can be observed that with short filling pulses, the peak height is smaller, implying partial trap recharge. With longer filling pulses, the peak height increases until it reaches saturation, i.e. implying all traps will be filled.

Since DLTS is capable of setting different rate windows, performing emission DLTS at different sampling times (keeping the ratio of the gate delay times t_2/t_1 constant to ensure self-consistent trap parameters [18]) will provide a set of true peak heights within a given temperature range. The change in the peak heights is related to the trap filling factor [17]. An Arrhenius plot of the DLTS peak heights and temperature positions can be used to determine the capture barrier energy directly.

A capacitance DLTS signal produced by thermal emission of carriers from a trap can be given by,

$$S(T) = C_0(t_\mathrm{f}, T)\{\exp[-e_\mathrm{n}(T)t_1] - \exp[-e_\mathrm{n}(T)t_2]\} \qquad (4.18)$$

where $C_0(t_\mathrm{f}, T)$ is the capacitance transient amplitude at temperature T obtained with a filling pulse width t_f. t_1 and t_2 are the gate delay times and e_n is the thermal emission rate. The maximum of the DLTS signals occur at T_max such that;

$$S(T_\mathrm{max}) = C_0(t_\mathrm{f}, T_\mathrm{max})B \qquad (4.19)$$

B is a factor that only depends on the ratio t_2/t_1. With long filling pulses, it is expected that the trap will be fully charged and the DLTS peaks for various rate windows (keeping the ratio t_2/t_1 constant) will have the same peak height but appear at different T_max. Under partial filling conditions, $C_0(t_\mathrm{f}, T)$ can now be expressed as

$$C_0(t_\mathrm{f}, T) = C_\mathrm{inf}[1 - \exp(-c_\mathrm{n} t_\mathrm{f})] \qquad (4.20)$$

where C_inf represents the transient capacitance amplitude for a very long charging time (infinite), and c_n is the capture rate. For a thermally activated capture process,

$$c_\mathrm{n} = v_\mathrm{th} n_\mathrm{cap} \sigma_\mathrm{n} = v_\mathrm{th} n_\mathrm{cap} \sigma_\mathrm{n}^{\infty} \exp(-\Delta E_\sigma / kT) \qquad (4.21)$$

$\sigma_\mathrm{n}^{\infty}$ is the high temperature trap electron capture cross section, ΔE_σ is the capture cross-section activation energy, and n_cap is the electron concentration available for trap capture. Assuming the thermal velocity v_th depends on temperature as $T^{1/2}$ while n_cap and C_inf are both temperature independent over the scanned temperature range, we can write,

$$\ln[1 - C_0(t_\mathrm{f}, T)/C_\mathrm{inf}] = KT^{1/2} \exp(-\Delta E_\sigma / kT) \qquad (4.22)$$

where K is the proportionality constant that includes the value of the filling pulse width, t_f that is kept constant for all the measurement rate windows.

For a saturating filling time (long pulse width), the emission DLTS peak is given by,

$$S(t_\mathrm{inf}, T_\mathrm{max}) = C_\mathrm{inf}(T_\mathrm{max})B \qquad (4.23)$$

Bestpfe.com

Thus, the capture barrier energy can be obtained as the gradient of the line from an Arrhenius plot of equation (4.22). The true capture cross-section will also be deduced from the intercept, i.e.

$$e^{c} = n_{\mathrm{cap}}\sigma_{\mathrm{n}}^{\infty}t_{f}\sqrt{\frac{3k}{m^{*}}} \tag{4.24}$$

where c is the intercept, k is the Boltzmann constant and $m^{*}$is the electron effective mass.

The other approach to obtain the capture barrier energy and capture cross-section is to use the pulse bias technique by Henry *et al.*[19]. In this particular method, the filling pulse width is related to the capacitance change, ΔC as,

$$\Delta C(t_{\mathrm{f}}, T) = \Delta C_{\mathrm{inf}}\left[1 - \exp\left(-\frac{t_{\mathrm{f}}}{\tau_{\mathrm{c}}}\right)\right] \tag{4.25}$$

where t_{f}, $C(t_{\mathrm{f}}, T)$ and C_{inf} have the same meaning as has been outlined before. τ_{c} is the capture time constant which is the inverse of the capture velocity, nC_{n}, where n is the carrier concentration and C_{n} can be given as a function of the capture cross-section, σ as,

$$C_{\mathrm{n}} = \sigma v_{\mathrm{th}} \tag{4.26}$$

with v_{th} having its usual meaning.

A plot of $\ln\left[1 - \frac{\Delta C(t_{\mathrm{f}}, T)}{\Delta C_{\mathrm{inf}}}\right]$ versus t_{f} for various temperatures (different rate windows) where the peak of $\Delta C(t_{\mathrm{f}}, T)$ occurs will yield the values of the capture time constant from the gradient of each line. From each of these values, the capture cross-section can be obtained as a function of temperature as,

$$\sigma(T) = \frac{m(T)}{n v_{\mathrm{th}}} \tag{4.27}$$

where $m(T)$ is the gradient obtained from each line at a particular temperature. The capture barrier energy and true capture cross-section can be obtained from an Arrhenius plot of equation (4.5), $\sigma(T) = \sigma_{\infty}\exp\left(-\frac{\Delta E_{\sigma}}{kT}\right)$, i.e.

$$\ln\sigma(T) = \ln\sigma_{\infty} - \frac{\Delta E_{\sigma}}{kT} \tag{4.28}$$

A plot of $\ln\sigma(T)$ versus $1/T$ gives a straight line whose gradient gives the capture barrier energy and the intercept yields the true capture cross-section.

4.4 Defect Depth profiling

DLTS can be used for the determination of the spatial distribution of a defect within a semiconductor and hence can help predict the defect introduction rate. Assuming that the DLTS signal peak height is directly proportional to the concentration of a deep level, the concentration can be obtained directly from a capacitance change observed using a complete trap filling pulse width. Using this concept, the concentration of a defect is given by [10],

$$N_T = \frac{2\Delta C(0)}{C} N_d \qquad (4.29)$$

where $\Delta C(0)$ is the capacitance change just after removing the complete trap filling pulse, C is the junction capacitance under quiescent reverse bias conditions and N_{d} is the net doping concentration obtained using the CV profiling technique. Determination of the defect concentration using eqn (4.29) usually results in an underestimation of N_{T}, particularly for thin films and under low reverse bias conditions. For a better estimation of the trap concentration, we need to consider the region marked λ in Figure 4.3 where the trap level crosses the Fermi level at a λ distance shallower than the depletion region edge. Within this region, the trap is filled and does not contribute to the capacitance transient when a filling pulse has been applied. The width of this particular region is given by [20]

$$\lambda = \left[\frac{2\varepsilon(E_{\mathrm{F}} - E_{\mathrm{T}})}{q^2 N_{\mathrm{D}}}\right]^{1/2} \qquad (4.30)$$

where ε is the semiconductor dielectric constant, E_{F} is the Fermi level, E_{T} is the trap level and q is the electronic charge. For one to determine the defect distribution profile, the defect states within the region to be profiled must be filled. The variation of the defect concentration with depth can be obtained using a constant (fixed) reverse bias voltage and changing the filling pulse height, usually referred to as the *fixed bias-variable pulse* method. This technique monitors the incremental change in capacitance $\delta(\Delta C)$ with a small change in majority carrier filling pulse height, δV_{p}. The relative incremental change in capacitance with pulse height is given by,

$$\delta\left(\frac{\Delta C}{C}\right) = \left(\frac{\varepsilon}{q w^2 N_{\mathrm{D}}}\right)\frac{N_T(x)}{N_D(x)}\delta V_{\mathrm{p}} \qquad (4.31)$$

where x is the depth below the junction, N_{D} is the ionized shallow impurity concentration, w is the depletion region, corresponding to quiescent reverse bias conditions. $N_{\mathrm{D}}(x)$ is obtained using the CV profiling technique. Double integration of the Poisson equation based on the

BESTPFE.COM
List of research project topics and materials

detailed derivation by [20] gives the total signal due to a majority carrier pulse. The corrected expression for the concentration of a deep level defect is given by,

$$N_T = \frac{2\Delta C(0) N_\mathrm{D}(x)}{C}\left[\left(\frac{x-\lambda}{x}\right)^2 - \left(\frac{x_\mathrm{p}-\lambda_\mathrm{p}}{x}\right)^2\right]^{-1} \quad (4.32)$$

$x-\lambda$ and $x_\mathrm{p}-\lambda_\mathrm{p}$ are the depletion widths before and after applying a filling pulse width, respectively. λ_p is the distance from the depletion region edge to the point where the trap level crosses the Fermi level during the application of the pulse. Using this technique, under low noise measurements, defect concentrations of the order of 10^{10} cm^{-3} are detectable.

4.5 Laplace DLTS

4.5.1 Introduction

Since the discovery of the DLTS technique by Lang in 1974, conventional DLTS has been an important tool in the determination of deep level defect signatures in semiconductors. Having the capability of analysing the temperature-dependent emission transient to produce a sequence of peaks on the temperature scale, ability to perform signal processing using the boxcar and lock-in techniques and excellent sensitivity, DLTS has taken many strides in helping improve device performance efficiency. However, the time constant resolution of this standard DLTS technique is poor for studying fine structure in the emission process [21] as it cannot be used to separate closely spaced transients. Since any variation of time constant in a defect results in additional broadening of the peak, there is need for a technique that can help resolve these time constants. Attempts to overcome this particular limitation have been made by using sophisticated peak deconvolution methods and development of different weighting functions [22]. However the problem with such methods is that extracting multiple closely spaced components decaying exponentially is fundamentally ill posed [21] and so in the presence of noise, there is no unique solution. In DLTS measurements, the signal is often quite small; sensitivity and signal to noise ratio considerations are very important [4]. To address the above mentioned problems of the conventional DLTS technique, Dobaczewski *et al* developed the high resolution Laplace-DLTS technique.

4.5.2 Laplace DLTS principles

Laplace-DLTS has a high sensitivity and a sufficiently high energy resolution (of the order of a few meV) to reveal information on the impurity's local environment [23]. In DLTS there are two main categories of transient processing that are classified as analog and digital signal processing. Analog signal processing is performed in real-time, i.e. as the temperature is ramped; one or two capacitance transients are extracted at a time. A filter is then used to produce an output that is proportional to the amount of signal that is observed at a particular time constant range. In digital signal processing, the analog transient output of the capacitance meter is digitized [21]. This is usually performed with the sample held at a fixed temperature and averaging many digitized transients to reduce the noise level. The acquired wave form is then processed using some algorithm. High resolution Laplace-DLTS uses this basis. In identifying the type of algorithm, a method of moments was applied by Ikossi-Anastasiou and Roenker [24], while Nolte and Haller [25] used an approximation the Gaver-Stehfest algorithm to effect a Laplace transform. Even though they achieved a substantial increase in resolution; in the presence of experimental noise levels, the approach appeared to be unstable. In the Nolte and Haller approach, the ultimate theoretical limit of time constant separation in the presence of noise is considered.

To give a quantitative description of nonexponentiality observed in the capacitance transients, one needs to assume that they consist of a spectrum of emission rates, [21]

$$f(t) = \int_0^{\infty} F(s)e^{-st}dt \tag{4.33}$$

where $f(t)$ is the recorded transient, and $F(s)$ is the spectral density function. The mathematical representation of the capacitance transients shown in eqn (4.33) is a Laplace transform of the true spectral density function. To determine the spectrum of the real emission rates present in the transient, an inverse Laplace transform has to be performed using numerical methods [4]. A spectrum of delta-like peaks is expected to be produced for multi-, mono-exponential transients, or broad spectrum with no fine structure for continuous distribution [21]. It has to be noted that eqn (4.33) does not have a general solution for any given function $f(t)$. According to Lerch's theorem [26], for an analytical multi-exponential function, such a solution exists and is unique. However, the number of possible solutions becomes infinite if the function is superimposed with noise. Numerical methods used in the

Laplace DLTS system seeks to find a spectral function with the least possible number of peaks, consistent with the data and experimental noise [4].

The Laplace DLTS system considered in this study consists of three different software procedures used for numerical calculations, based on the Tikhonov regularization method [27]. The three numerical routines are the CONTIN [28], FTIKREG[29] and FLOG[30]. The three differ in the way the criteria for finding the regularization parameters are defined. During the experiment, sample excitation parameters are set using the Laplace card. In some cases, the card is used to trigger an external pulse generator, which supplies the biasing and pulsing conditions to the sample. The Laplace software then acquires the capacitance transient which will then be converted into LDLTS spectra using numerical algorithms. In DLTS, not all states are expected to produce ideal exponential decays. Some conditions e.g. the Poole Frenkel effect result in an increased emission with increasing field, thus it is important that any algorithm must provide accurate amplitude and rate information in relation to each transient component. The parallel use of the three different software packages increases the level of confidence in the spectra obtained [4].

Summary

Properties of the DLTS technique which include among others, its high sensitivity, high resolution and ability to uniquely determine the position of a peak in temperature using thermal emission properties of a trap have been exploited to study deep level defects in ZnO. Capacitance based DLTS has been used to monitor the change in the capacitance within the depletion region of fabricated Schottky contacts leading to the determination of “defect signatures”. This technique has been successfully employed to study the temperature dependence of the capture cross-section of deep level defects. Laplace DLTS principles have also been employed to separate closely spaced energy levels in broad peaks.

References

1. M.A. Green, Solar Cells, Prentice-hall Inc., Englewood Cliffs, NJ, 1982
2. F. D. Auret, P. N. K. Deenapanray, Critical Reviews in Solid State and Materials Sciences, **29**, 1 (2004)
3. H. J. Queisser, Science, **281**, 945 (1998)
4. L. Dobaczewski, A. R. Peaker, K. Bonde Nielsen, J. Appl. Phys. **96**, 9 (2004)
5. Shockley and W. T. Read, Jr., Phys. Rev. **87**, 835 (1952)
6. S. M. Sze, *Physics of Semiconductor Devices* (Wiley, New York, 1969)
7. C. H. Henry and D. V. Lang, Phys. Rev. B, **15**, 989 (1977)
8. G. L. Miller, D. V. Lang, and L. C. Kimerling, Capacitance Transient Spectroscopy. Ann. Rev. Mater. Sci. **7**, 377 (1977)
9. C. O. Almbladh and G. J. Rees, Statistical Mechanics of Band States and Impurity States in Semiconductors, J. Phys. C: Solid State Phys. **14**, 4575 (1981)
10. D. V. Lang J. Appl. Phys. **45**, 3023 (1974)
11. W. E. Meyer PhD Thesis, University of Pretoria 2007
12. K. Knobloch, H. Alexander, Mat Sci. Eng. B, **42**, 63 (1996)
13. W. Szkielko, O. Breitenstein, and R. Pickenhein, Cryst. Res. Technol. **16**, 197 (1981)
14. D. Cavalcoli, A. Cavallini, E. Gombia, Phys. Rev. B, **56**, 23 (1997)
15. P.I. Rockett, A.R. Peaker, Electronic Lett. **17**, 22 (1981)
16. J. H. Zhao, T.E Schlesinger, and A.G Milnes J. Appl. Phys. **62**, 7 (1987)
17. J. Criado, A. Gomez, E. Munoz, and E. Calleja, Appl. Phys. Lett. **52**, 8 (1988)
18. J. Criado, A. Gomez, E. Munoz, and E. Calleja, Appl. Phys. Lett. **49**, 26 (1986)
19. C. H. Henry, H. Kukimoto, G. L. Miller, and F. R. Merrit, Phys. Rev. B **7**, 2499 (1973)
20. Y. Zohta, M. O. Watanabe, J. Appl. Phys. **53**, 3, 1809 (1982)
21. L. Dobaczewski, P. Kaczor, I. D. Hawkins and A. R. Peaker, J. Appl. Phys. **76**, 194 (1994)
22. A. A. Istratov, J. Appl. Phys. **82**, 2965 (1997)
23. http://www.laplacedlts.eu/Dodatki/WordPress/laplacedlts/
24. K. Ikossi-Anastasiou and K.P. Roenker, J. Appl. Phys. **61**, 182 (1987)
25. D. D. Nolte, and E.E. Haller, J. Appl. Phys. **62**, 900 (1987)
26. G. A. Korn, and T. M. Korn, in Mathematical Handbook , McGraw-Hill, New York, 1968
27. C. Eiche, D. Maier, M. Schneider, D. Sinerius, J. Weese, K. W. Benz, and J. Honerkamp, J. Phys. Condens. Matter, **4**, 6131 (1992)

28. S. W. Provencher, Compt. Phys. Comm. **27**, 213 (1982)

29. J. Weese, Compt. Phys. Comm. **69**, 99 (1991)

30. A. Matulis, Z. Kancleris, Semiconductors Physics Institute, Vilnius, Lithuania

Chapter 5

Experimental Techniques

Introduction

This section outlines all the procedures that were followed in the electrical characterization of defects in ZnO starting with sample cleaning, contact fabrication, contact quality evaluation and defect characterization. It also explains some sample preparation methods that were employed to intentionally introduce defects such as proton irradiation and annealing.

5.1 Sample cleaning

Undoped bulk single crystal n-type ZnO samples obtained from Cermet Inc. were used in this study. The samples were rinsed in an ultrasonic bath, first in acetone for five minutes, then in methanol for another five minutes and then treated with boiling concentrated hydrogen peroxide for three minutes. Without any water rinse, the samples were blown dry using nitrogen gas. Immediately after cleaning the samples were taken for ohmic and Schottky contact fabrication. This procedure was followed for all the samples used in this study.

5.2 Contact fabrication

Ohmic and Schottky contacts were fabricated onto either the Zn- or O-polar face of the samples for comparison purposes. Ohmic contacts of either Ti/Al/Pt/Au or Al/Au were e-beam and resistively deposited, respectively as outlined in the results and discussion section. Pd, Ir and Pt were used to fabricate the Schottky contacts. It must be mentioned that in this study, if the ohmic contact was fabricated on the Zn-polar face, the Schottky was put on the O-polar face and vice-versa. The fabrication of the ohmic and Schottky contacts was

performed in vacuum. Since it was observed that e-beam deposition introduces defects in semiconductors, Schottky contacts for the control sample were fabricated using the resistive evaporation system shown in Figure 5.1.

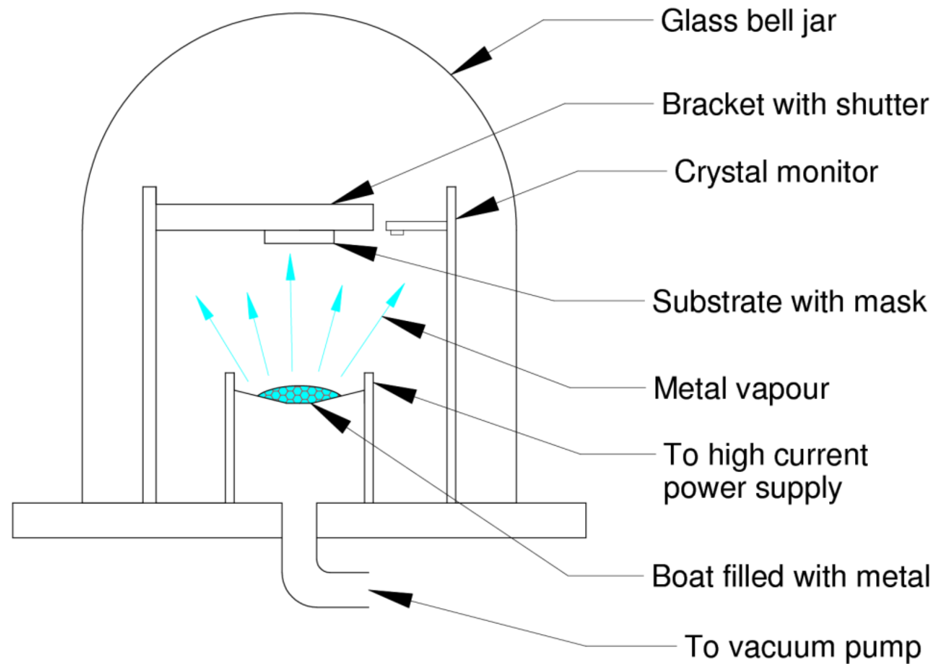

Figure 5.1: Schematic diagram of the resistive evaporation system for contact fabrication.

This method of metal evaporation uses the thermal resistance of the material to melt and evaporate it. A current is supplied and flows through the crucible containing the metal. This crucible heats up because of the metal resistance until the melting point of the metal is reached where it starts evaporating, depositing onto the sample. The amount of current supplied to the material after the melting point has been reached determines the deposition rate. This evaporation technique is ideal for metals with low melting points, $\leq$ 1600°C.

In studying e-beam induced defects, Schottky contacts were fabricated using the e-beam deposition technique. Figure 5.2 shows a typical e-beam deposition system.

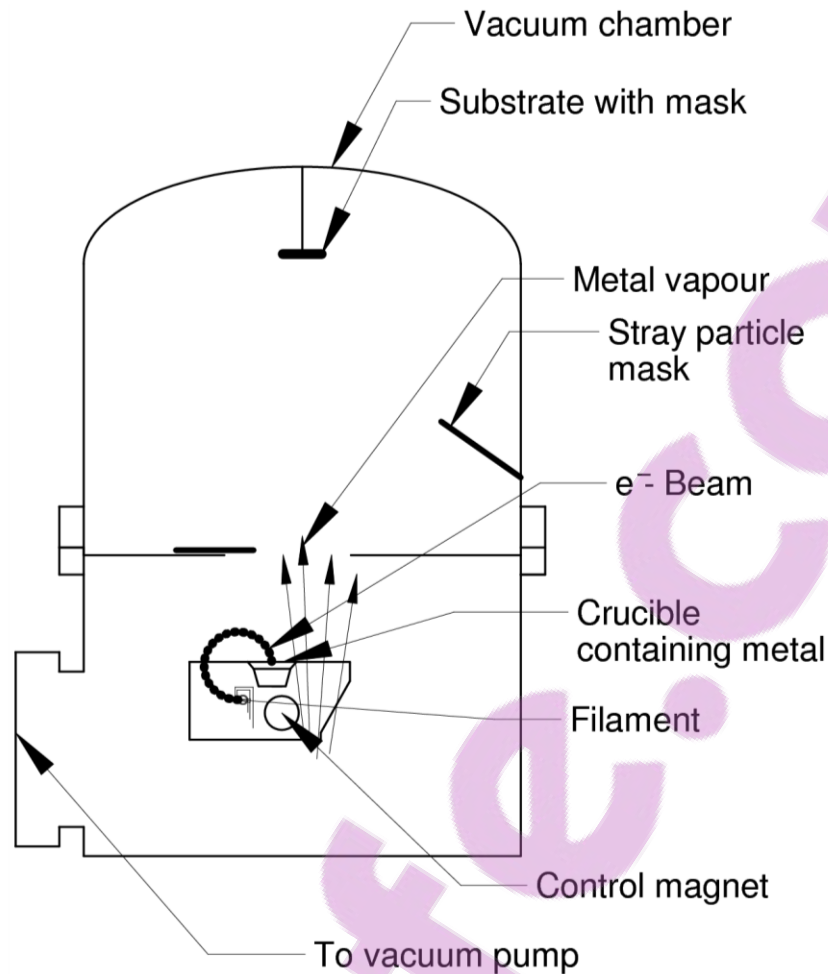

Figure 5.2: Schematic diagram of the electron-beam (e-beam) evaporation system for Schottky contact fabrication.

A beam of electrons emitted by a hot filament is used to heat and evaporate the metal. Electrons are accelerated by a high voltage and bent by the magnetic field towards the metal. The current supplied to the filament controls the rate at which the metal deposits onto a sample. This technique is ideal for high melting point metals, and can also be used for low melting point metals.

During the fabrication of Schottky contacts with either the resistive or the e-beam system, a mask with circular holes was used to produce circular contacts on the sample surface. Figure 5.3 shows a sample containing the ohmic (back contact) and Schottky (circular dots) contacts.

Bestpfe.com

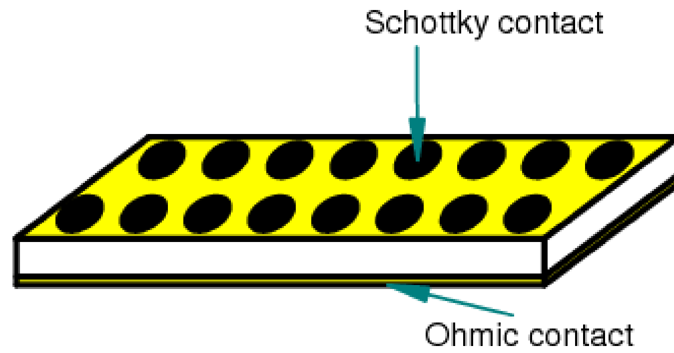

Figure 5.3: A schematic diagram showing the ohmic and Schottky contacts fabricated on ZnO

5.3 Current-Voltage and Capacitance-Voltage measurements

The Current-Voltage (IV) measurement technique is ideal for checking the quality of the Schottky contacts. By measuring the current that flows through the contact under forward and reverse bias conditions, one can deduce whether the contact is a good rectifier or is an ohmic contact. This helps in obtaining the reverse bias conditions which can be applied to a particular contact when one uses capacitance based techniques e.g. DLTS to determine other electronic properties of the contacts such as defects. An analysis of the IV characteristics of a contact can give other contact parameters such as the barrier height, ideality factor and series resistance. These characteristics can help one deduce the dominant current transport mechanisms. In this study, current-voltage measurements were performed in the dark at room temperature conditions. A schematic diagram of the IV and CV station is shown in Figure 5.4. An HP 4140B pA meter/ DC voltage source with a current limit of 10^{-14}A was used to determine the IV characteristics of the contacts.

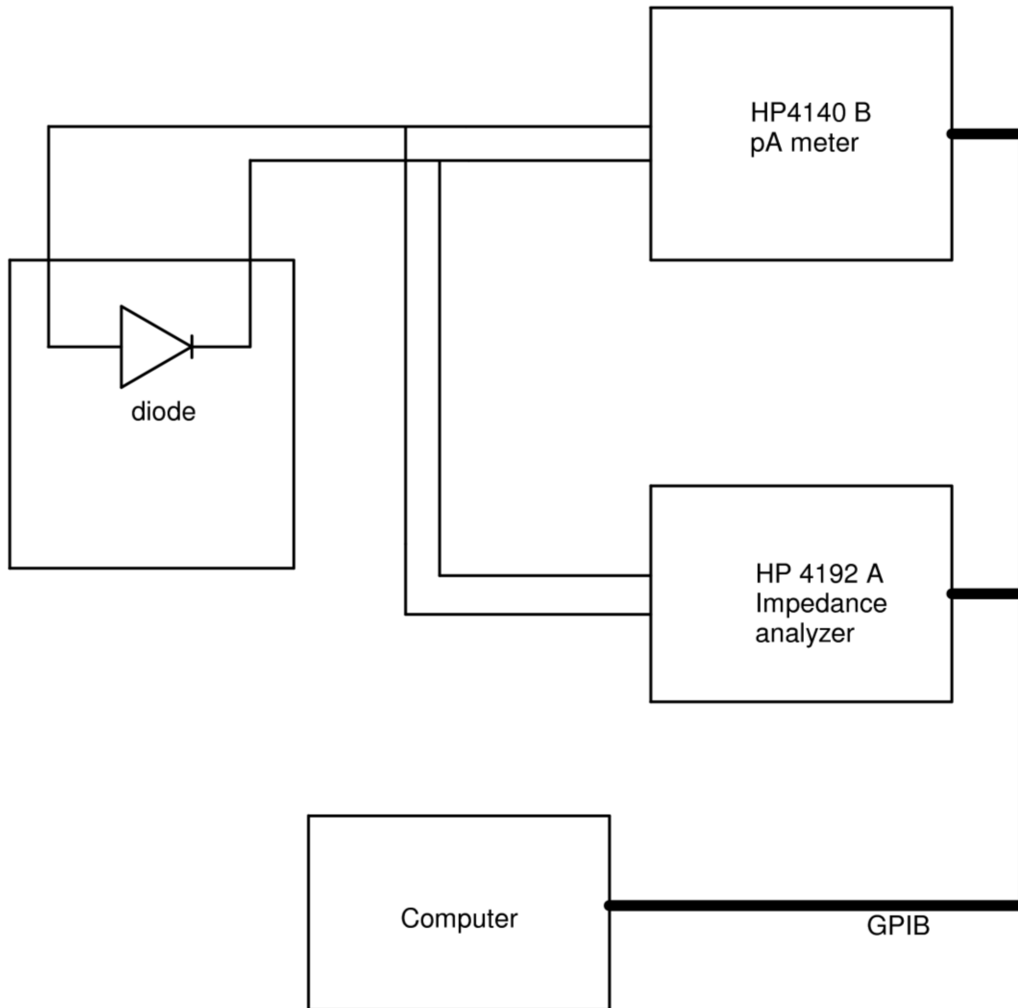

Figure 5.4: A schematic diagram of the IV and CV station that was used in this study.

The Capacitance-Voltage (CV) technique is also used to deduce important parameters of the contact that include the barrier height, the built-in-voltage and free carrier concentration. The use of the CV technique for depth profiling can also yield the net doping concentration of the metal-semiconductor conductor as a function of depth. An HP 4192A LF impedance analyser was used to determine the CV characteristics of the contacts. These measurements were also performed in the dark.

BESTPFE.COM
List of research project topics and materials

5.4 Deep Level Transient Spectroscopy (DLTS) and Laplace-DLTS

Conventional DLTS and high resolution Laplace DLTS were used to characterize the defects in ZnO. Measurements were performed in the 30 K – 350 K temperature range. Figure 5.5 shows a schematic diagram of the DLTS and Laplace-DLTS system that was used in characterizing defects.

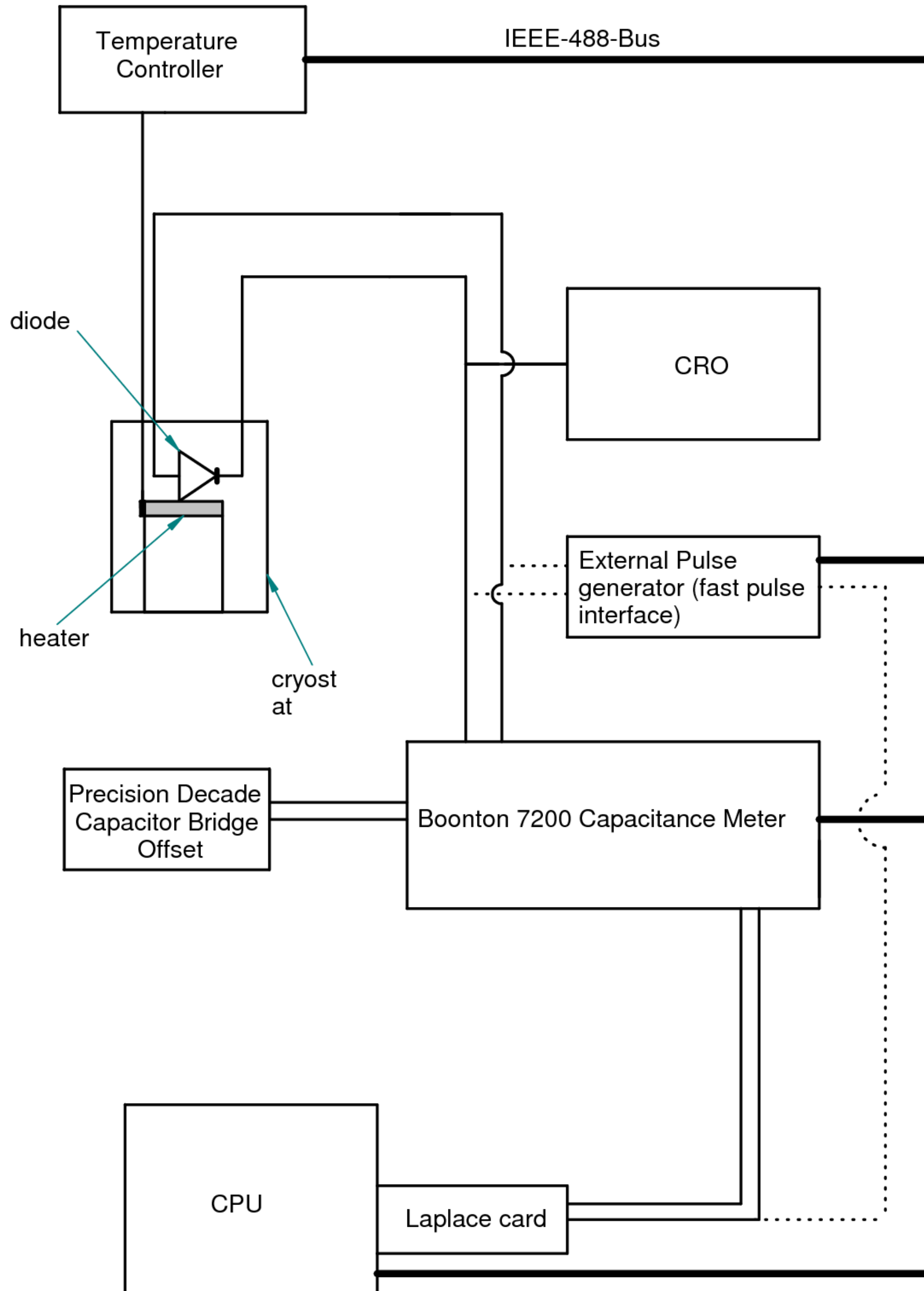

Figure 5.5: Schematic diagram of the DLTS and Laplace DLTS system. The dotted lines show the necessary connections when an external pulse generator is used.

As indicated in Figure 5.5, the sample was mounted in a cryostat. A closed cycle helium cryostat was used in the cooling from high temperatures to low temperatures. A heater located at the tip of the cryostat was used in raising temperature from the low values to high temperature values. The temperature was controlled by a Lakeshore 330 temperature controller. Thermal emission of carriers after excitation by the pulse generator was monitored using the Boonton 7200 capacitance meter with a 100 mV, 1MHz ac voltage signal. A Laplace card [1] with an internal pulse generator was used for generating the desired quiescent reverse bias voltage and pulses. It also contains software that is used for data collection and has a processing system which analyses and averages transients before displaying the spectra for both the conventional and Laplace-DLTS. The Laplace card is also used to record the capacitance-temperature (CT) scans.

Since the Laplace card could not produce well defined signals for short filling pulse widths, an external signal generator (fast pulse interface) was used in measurements that required the use of pulses with shorter filling pulse widths.

Conventional-DLTS and Laplace-DLTS sample excitation parameters are set up using the Laplace program. These include capacitance transient acquisition conditions, measurement initiation, transient acquisition and conversion into a DLTS or Laplace-DLTS spectrum. In the conventional-DLTS mode, the capacitance meter measures the capacitance transients after excitation. These transients are then processed by the Laplace card. Ramping up/down the temperature using a particular rate window, a DLTS spectrum is displayed on a computer. When one is using the Laplace-DLTS mode, the capacitance meter also monitors the capacitance transients after excitation at a fixed temperature. The Laplace card performs transient averaging and implements the inverse Laplace transform to calculate the signal magnitude and emission rates using three different routines; CONTIN, FTIKREG and FLOG [2] before a Laplace spectrum is displayed on the computer.

5.5 Sample annealing

Crystal annealing can at times help reduce defects in semiconductors and in some cases can also introduce them in a case where a certain defect species diffuse along a certain direction within the semiconductor. Annealing of samples was performed in a Lindberg Hevi-duty furnace. Depending on the type of atmosphere/ambient required, the furnace was connected

to a cylinder containing the gas required. The gas was supplied constantly at 3.0 L/min for the entire annealing period. Annealing times for each experiment are given in the results and discussion section.

Vacuum annealing was performed in a Lindberg furnace at a pressure of approximately 10^{-7} Torr. It must be noted that prior to annealing the samples were rinsed in methanol in an ultrasonic bath for five minutes and then blown dry using nitrogen gas. Sample preparation and defect characterization was performed as outlined in sections 5.1 – 5.4. Since it was observed that e-beam fabrication of contacts introduces defects, ohmic and Schottky contacts on annealed samples was performed using the resistive evaporation technique.

5.6 Proton irradiation

Sample irradiation on the deposited Schottky contacts was performed with a van de Graaff accelerator. An energy of 1.6 MeV and a fluence of $1 \times 10^{14} \text{cm}^{-2}$ were used. Immediately after irradiation, the samples were taken for contact evaluation using IV and CV measurements and defect characterization using DLTS and L-DLTS.

References

1. L. Dobaczewski, P. Kaczor, I. D. Hawkins, and A. R. Peaker, J. Appl. Phys. **76**, 194 (1994)
2. L. Dobaczewski, A. R. Peaker and K. B. Nielsen, J. Appl. Phys. **96**, 4689 (2004)

Chapter 6

Results and discussions

6.1 Defects in ZnO

Introduction

ZnO occurs naturally as an n-type semiconductor. This n-type conductivity is attributed to native defects and impurities introduced into the material during growth. During material growth, impurities introduce energy states in the forbidden region within the bandgap of the semiconductor. Depending on their location within the ZnO bandgap, these impurities can be classified as either shallow levels or deep level defects. Characterization of these defects can be performed using several techniques. In this thesis, the Hall effect and DLTS techniques were used to characterize defects. This section gives an outline of the defects observed in as-received bulk single crystal ZnO using DLTS.

Results and discussions

The DLTS spectrum obtained from the as-received ZnO samples using conventional DLTS is shown in Figure 6.1.1.

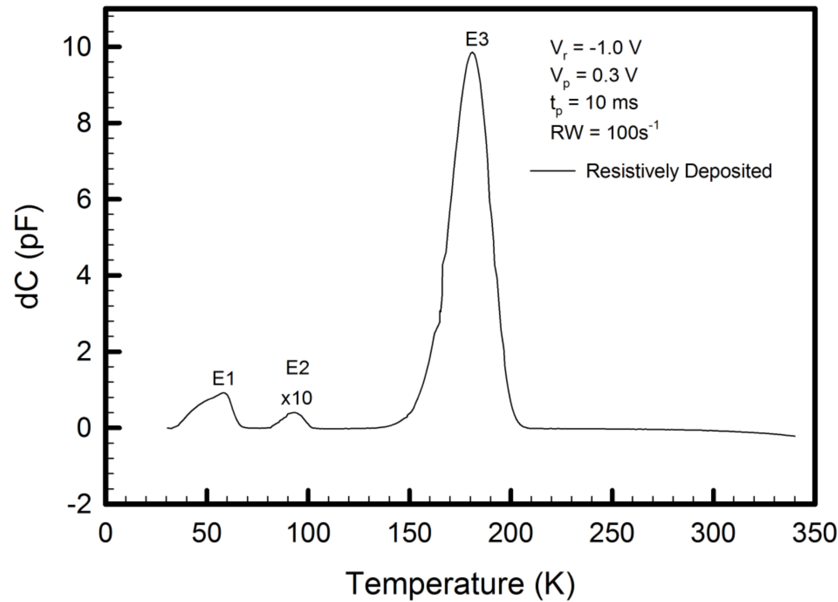

Figure 6.1.1: DLTS spectrum obtained from the as-received melt grown single crystal ZnO obtained from Cermet. The spectrum was obtained at a quiescent reverse bias of 1.0 V, filling pulse width of 10 ms, pulse height, V_p = 0.3 V and rate window of 100 s^{-1}.

To facilitate the use of DLTS, Pd Schottky contacts were resistively deposited on ZnO as it has been observed that this technique does not introduce defects in ZnO [1]. Defects labelled E1 and E3 have been observed in material grown using different techniques. This clearly indicates that these defects are common to ZnO regardless of the growth, processing and contact fabrication techniques [2, 3, 4, 5]. However, the E2 defect has not been reported by many as it has not been observed in some other ZnO materials. Hence this defect might be growth technique related. The Arrhenius plots to determine the estimated activation enthalpies of the E1, E2 and E3 deep level defects are shown in Figure 6.1.2.

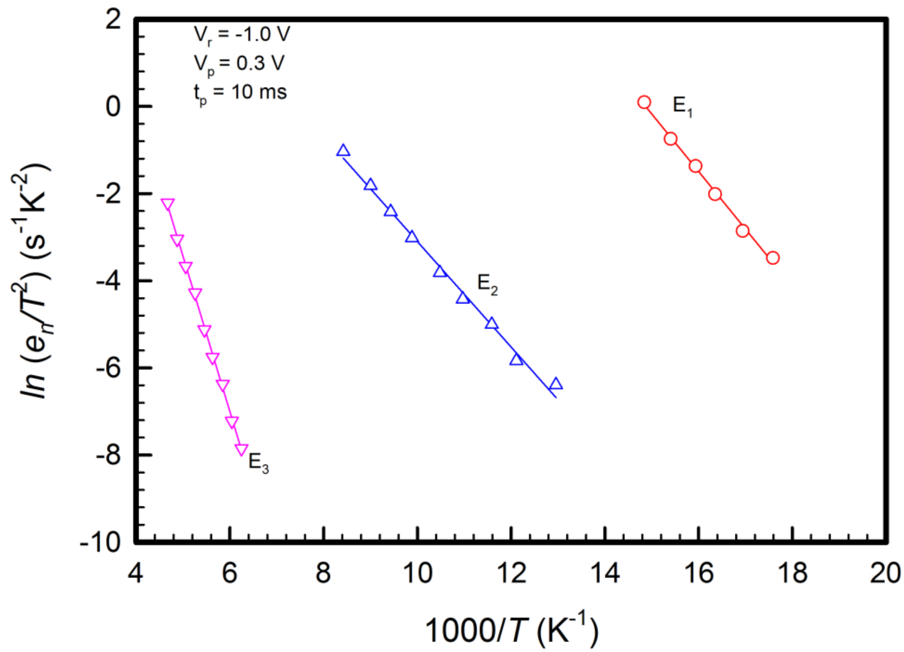

Figure 6.1.2: Arrhenius plots for the as–received melt grown bulk single crystal ZnO.

From the DLTS spectrum of Figure 6.1.1, the E1 peak is asymmetric. This could be due to the fact that it is observed very close to the freeze out region. The *C-T* scan showing the freeze out region of ZnO is shown in Figure 6.1.3.

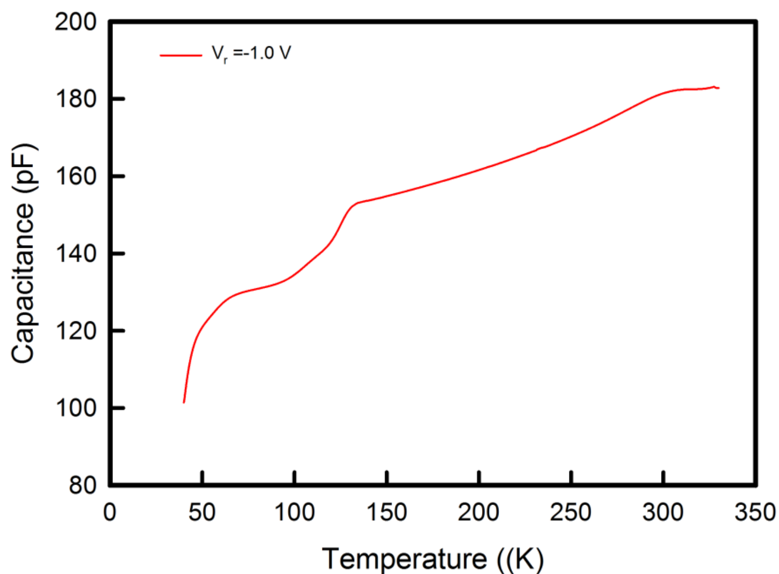

Figure 6.1.3: Capacitance-temperature scan for the as–received melt grown bulk single crystal ZnO. This scan was recorded at a constant reverse bias voltage of 1.0 V, scanning up in temperature.

The freeze out region of ZnO starts occurring at a temperature of about 50 K. The location of the E1 peak near the freeze out region can also influence the accurate determination of its

activation enthalpy. Due to this effect, values ranging from 0.11 – 0.12 eV have been reported for the activation enthalpy of the E1 peak.

Values of estimated activation enthalpies, apparent capture cross-sections and possible identities of these defects are shown in Table 6.1.1. Material growth techniques are also included.

Table 6.1.1. *Values of estimated activation enthalpy, apparent capture cross-section and possible identities of the deep level defects observed in ZnO.*

Defect label	Material Growth technique*	Activation enthalpy (eV)	Apparent capture cross section (cm^2)	Identity	Ref
E1	*PLD	0.10	?	?	[2]
	*MG	0.111	5.2×10^{-12}	O_i?	[3]
	*SCVT	0.12	?	?	[4]
	MG	0.12	?	?	[4]
	Vapour phase	0.12	2.7×10^{-13}	?	[5]
E2	MG	0.110	1.23×10^{-16}	?	[1]
	SCVT	0.10	1×10^{-17}	?	[4]
E3	PLD	0.31	5×10^{-16}	?	[6]
	Hydrothermal	0.30	2.0×10^{-15}	O_2 deficiency	[7]
	Hydrothermal	0.29	2.6×10^{-14}	V_O	[8]
	SCVT	0.29	1.0×10^{-15}	V_O?	[4]
	MG	0.30	2.7×10^{-14}	Transition metal ion related?	[1]
	MG	0.29	1.0×10^{-15}	V_O?	[4]
	Vapour phase	0.29	5.8×10^{-16}	?	[5]
	PLD	0.30	?	?	[2]
	SCVT	0.30	?	?	[9]
	PLD	0.30	2.6×10^{-16}	Transition metal ion related	[10]

*PLD refers to Pulsed Laser Deposition,

*MG refers to Melt growth,

*SCVT refers to Seeded Chemical Vapour Transport

The E1 deep level shows strong electric field dependence which results in electric field enhanced emission effects as shown in Figure 6.1.4. Such an effect has also been reported by [11, 12].

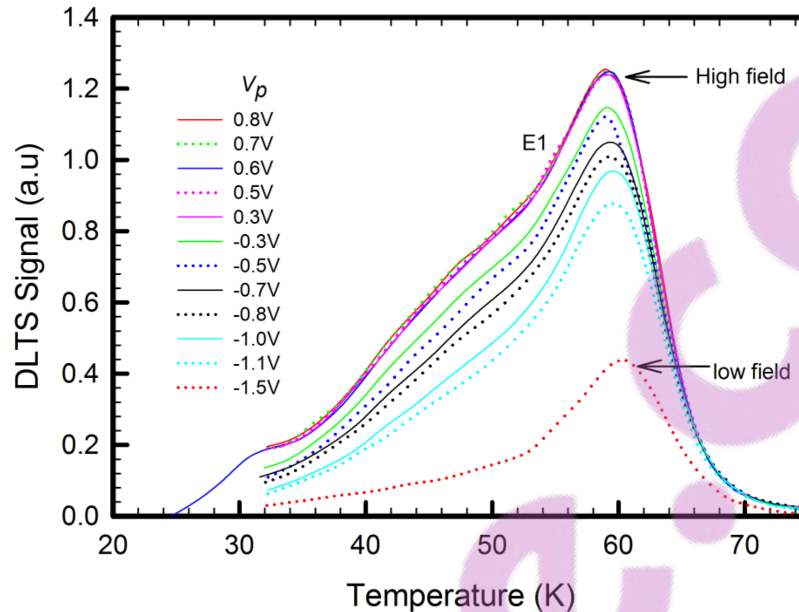

Figure 6.1.4: DLTS spectra showing the electric field dependence of the E1 defect at a rate window frequency of 100Hz, reverse bias voltage of 2.0 V, and filling pulse width of 2.0 ms.

Based on the summary presented in Table 6.1.1, it can be clearly observed that the identities of the native defects in ZnO are not clear yet. However the only valid conclusion is that ZnO contains the E1 and E3 defects independent of the technique used for material growth.

Of particular interest from this study is the behaviour of the E3 defect. The capacitance transients are observed to be non-exponential and also the DLTS peak height shows a significant dependence on rate window frequency. Using shorter filling pulse widths, the peak height increases with increase in rate window. Using large filling pulse widths, the DLTS peak height for all rate window frequencies is the same. This behaviour has been attributed to the temperature dependence of the capture cross-section due to a capture barrier which electrons from a trap level have to overcome to be re-emitted back to the conduction band. A detailed analysis of the behaviour of E3 is given in the attached publication.

Publication 1: On the temperature dependence of the electron capture cross-section of the E3 deep level observed in single crystal ZnO

On the temperature dependence of the electron capture cross-section of the E3 deep level observed in single crystal ZnO

Wilbert Mtangi[1], Matthias Schmidt[1], P. Johan Janse van Rensburg[1], Walter E. Meyer[1], Danie F. Auret[1], Jacqueline M. Nel[1], Mmantsae Diale[1], Albert Chawanda[2]

1 Department of Physics, University of Pretoria, Private bag X20, 0028 Hatfield, South Africa
2 Midlands State University, Private Bag, 9055 Senga Gweru, Zimbabwe

E-mail: `wilbert.mtangi@up.ac.za`

Abstract. We report on the temperature dependence of the capture cross-section of the E3 deep level defect observed in single crystal ZnO samples. Temperature dependent deep level transient spectroscopy reveals an increase in the DLTS peak height with an increase in the rate window frequency for the E3 level which is a proof that the E3 deep level has a temperature activated capture cross-section. However the observed capture rate is not constant during the filling pulse but depends on the occupancy of the defect itself. This phenomenon is in contradiction with what is expected of an ideal deep level.

1. Introduction

ZnO is a wide and direct bandgap semiconductor with experimental bandgap energy of about 3.4 eV. Deep level transient spectroscopy (DLTS) measurements performed on differently grown ZnO crystals reveal the presence of the E3 deep level defect with an activation enthalpy of between 0.29 eV and 0.31 eV and an apparent capture cross-section of $5 \times 10^{-16}\,\mathrm{cm}^2$ to $10^{-14}\,\mathrm{cm}^2$ [1, 2, 3, 4, 5, 6]. However its ionisation energy as well as its energy barrier for electron capture is not known yet, whereas in established semiconductors such as GaAs and Si, capture barrier energies for most defect levels are well known. The capture barrier is usually obtained using emission rate DLTS scans and varying the filling pulse width as suggested by Henry and Lang [7]. A second method which uses DLTS rate window scans with short filling pulses (less than $10\,\mu$s) has been employed by Zhao *et al.* [8], Criado *et al.* [9], Telia *et al.* [10] and Cavalcoli *et al.* [11]. In this paper, we report on the electronic properties of the E3 deep level in a bulk single crystal ZnO sample obtained from Cermet Inc.

2. Sample preparation

In preparation of the DLTS measurements, crystal cleaning was performed as in reference [12]. Ohmic contacts with a composition of Al/Au were deposited on the O-polar face using the resistive evaporation technique at a pressure of approximately 10^{-6} Torr. Finally, Iridium Schottky contacts with a diameter of 0.5 mm and thickness of 100 nm were electron beam deposited onto the Zn-polar face under vacuum at a pressure of approximately 10^{-7} Torr.

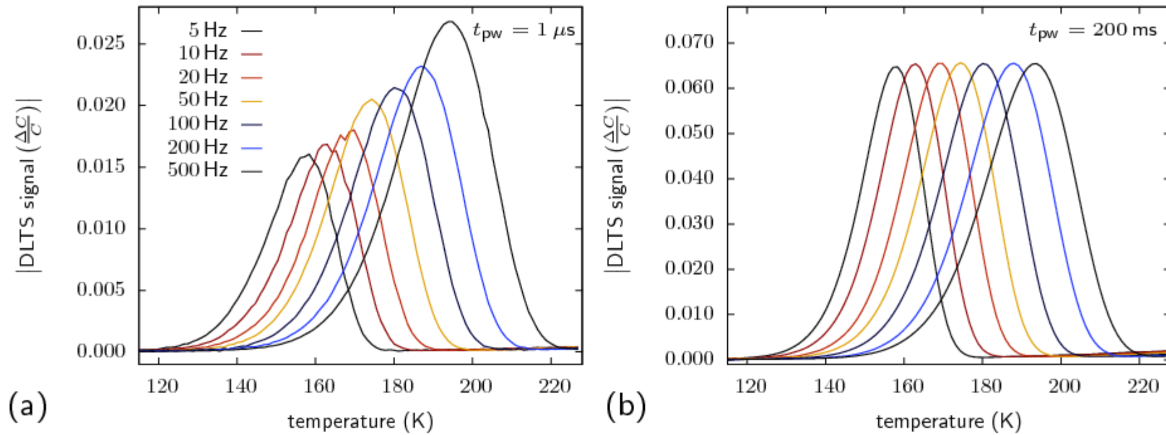

Figure 1. The E3 peak in deep level transient spectroscopy temperature scans conducted at different rate window frequencies using $1\,\mu$s filling pulses (a) and 200 ms filling pulses (b) that flattened the bands. During the recording of the capacitance transients the sample was reverse biased at 2 V.

Current voltage measurements at room temperature confirmed that the sample was suitable for DLTS measurements and a net doping density of $N_{\text{net}} = 4.6 \times 10^{16}\,\text{cm}^{-3}$ was obtained from CV measurements using the van Opdorp analysis [13].

3. Results and discussion

Emission DLTS rate window scans were performed in the dark in a closed cycle helium cryostat and revealed the presence of the E3 deep level, as shown in Figure 1. Arrhenius analysis[1] of the temperature dependence of the thermal emission rate of the E3 level yielded an activation enthalpy of 0.30 eV and an apparent capture cross-section of $10^{-14}\,\text{cm}^2$. It was observed that the spectra differ depending on the filling pulse width (t_{pw}). For $t_{\text{pw}} = 1\mu s$ filling (Figure 1(a)), the DLTS peak height increases with an increase in rate window frequency, whereas for long enough filling pulse widths (Figure 1(b)), the peak height was constant for all rate window frequencies. The variation of the DLTS peak height with chosen rate window frequency for the E3 deep level has previously been observed but to the best of our knowledge, no explanation was given. In the following we are going to shed some light on this observed effect. The DLTS experiment allows one to prepare an initial probability to find a defect state occupied by an electron, q_{in}. This is achieved by the application of a filling pulse and monitoring the capacitance transient afterwards. The DLTS signal peak height, $\Delta C/C$ is related to the trap concentration N_{t} and the difference in the occupancy probabilities by,

$$\frac{\Delta C}{C} = -\frac{N_{\text{t}}}{2N_{\text{net}}}\left(q_{\text{fin}} - q_{\text{in}}\right) \tag{1}$$

where q_{fin} is the final occupation probability. The differential equation for the time evolution of the occupancy probability $q(t)$ of a defect state is [14]

$$\frac{\mathrm{d}q(t)}{\mathrm{d}t} = c_{\text{n}}\left[1 - q(t)\right] - e_{\text{n}}^{\text{th}} q(t). \tag{2}$$

[1] ZnO effective mass: $0.27\,m_{\text{e}}$

BESTPFE.COM
List of research project topics and materials

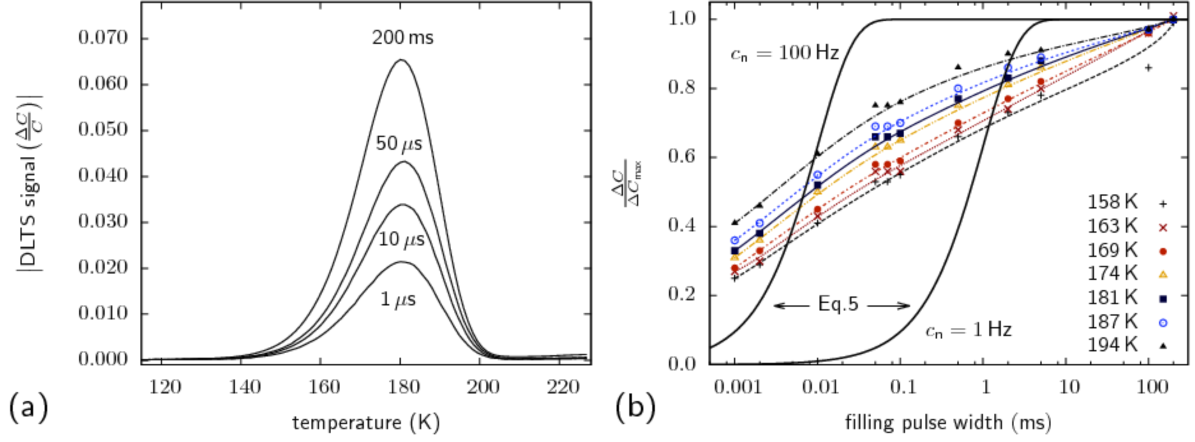

Figure 2. a) Dependence of the E3 DLTS peak height on filling pulse width t_{pw} at a rate window frequency of 100 Hz. b) Symbols represent the variation of the measured, normalised DLTS peak height with filling pulse width and sample temperature. The black solid lines are the graphical representation of equation 5 assuming a constant capture cross-section during the filling process.

c_n denotes the thermal capture rate for electrons and its temperature-dependence is given by

$$c_n(T) = \sigma_n(T) \langle v_{th} \rangle (T) n(T) = \sigma_n^{\infty} \exp\left(-\frac{E_b}{k_B T}\right) \langle v_{th} \rangle (T) n(T) \tag{3}$$

where E_b is the barrier for electron capture, $\langle v_{th} \rangle (T)$ is the thermal velocity of electrons and n is the free electron concentration available for capture. Since at a particular temperature, c_n is considered to be a constant and assuming that during the filling process, $e_n^{th} \ll c_n$, the solution of equation 2 is given by

$$q(t) = 1 - \exp(-c_n t). \tag{4}$$

Thus, equation 1 can be written as,

$$\frac{\Delta C}{C} = \frac{N_t}{2N_{net}} (1 - \exp[-c_n t_{pw}]) \tag{5}$$

since for the maximum DLTS peak height, $q_{fin} \approx 0$.

In the light of this, we studied the filling process of E3 by varying the filling pulse width at fixed rate window frequency. The results are presented in Figure 2(a). As expected, the DLTS peak height increases with increasing filling pulse width as well as increasing temperature, Figure 2(b). However this increase is not in accordance with equation 5 and therefore the Henry and Lang approach [7] cannot be applied. In particular, the slope of the measured, normalised DLTS peak height versus filling pulse width plot is less steep compared to the one predicted by equation 5. A suggestion of this is as follows.

Since every solution of equation 2 must be exponential if c_n and e_n^{th} are constant, only a change of c_n during the filling process can explain our observations. According to equation 3, this change can be attributed to either a decrease in σ_n (at the same temperature) or a decrease in n in the vicinity of the defect while it is being filled. The first possibility might originate from defect-defect interaction which cannot be excluded at doping levels of $N_{net} = 4.6 \times 10^{16}\,\text{cm}^{-3}$. The latter, which to our opinion might be more probable, is due to the charging up of grain

boundaries. This results in a double Schottky barrier and therefore a depletion region which lowers the local electron density [15]. Further investigations and analysis are required and will be performed.

4. Conclusions

In conclusion, the electron capture of the E3 deep level in ZnO was studied in detail by DLTS. The capture process cannot be described by a single exponential filling of the defect state, as would be the case for a simple capture barrier of an isolated point defect. Due to this difficulty, the capture barrier could not be obtained from emission DLTS rate window scans with varying pulse widths without employing a more involved analysis. Furthermore there is a high uncertainty associated with the high temperature limit of the capture cross-section obtained from standard Arrhenius analysis which is frequently reported.

Acknowledgments

The authors wish to thank the University of Pretoria for the financial support. Matthias Schmidt was funded by the Postdoctoral Fellowship Program of the University of Pretoria. This work is based upon research supported by the National Research Foundation (NRF). Any opinion, findings and conclusions or recommendations expressed in this material are those of the author(s) and therefore the NRF does not accept any liability in regard thereto.

References

[1] F.D. Auret, S.A. Goodman, M.J. Legodi, W.E. Meyer, and D.C. Look. *Electrical characterization of vapor-phase-grown single-crystal ZnO*. Appl. Phys. Lett., **80** 1340–1342, (2002).

[2] A.Y. Polyakov, N.B. Smirnov, A.V. Govorkov, E.A. Kozhukhova, S.J. Pearton, D.P. Norton, A. Osinsky, and A. Dabrian, *Electrical Properties of Undoped Bulk ZnO Substrates*. J. Electron. Mater., **35** 663-669, (2006)

[3] F.D. Auret, W.E. Meyer, P.J. Janse van Rensburg, M. Hayes, J.M. Nel, H. von Wenckstern, H. Schmidt, G. Biehne,H. Hochmuth, M. Lorenz, M. Grundmann, *Electronic properties of defects in pulsed-laser deposition grown ZnO with levels at 300 and* 370 meV *below the conduction band*. Physica B, **401-402** 378-381 (2007)

[4] H. von Wenckstern, K. Brachwitz, M. Schmidt, C.P. Dietrich, M. Ellguth, M. Stlzel, M. Lorenz and M. Grundmann, *The E3 Defect in MgZnO*. J. Electron. Mater., **39** 584-588, (2010)

[5] W. Mtangi, F.D. Auret, P.J. Janse van Rensburg, S.M.M. Coelho, M.J. Legodi, J.M. Nel, and W.E. Meyer, *A comparative study of the electrical properties of Pd/ZnO Schottky contacts fabricated using electron beam deposition and resistive/thermal evaporation techniques*. J. Appl. Phys., **110** 094504, (2011)

[6] Matthias Schmidt, *Space Charge Spectroscopy Applied to Defect Studies in Zinc Oxide Thin Films*, PhD thesis, Universität Leipzig, Germany (2012).

[7] C.H. Henry and D.V. Lang, *Nonradiative capture and recombination by multiphonon emission in GaAs and GaP*. Phys. Rev. B **15** 989-1016 (1977).

[8] J.H. Zhao, T.E. Schlesinger, and A.G. Milnes, *Determination of carrier capture cross sections of traps by deep level transient spectroscopy of semiconductors*. J. Appl. Phys. **62** 2865–2870 (1987).

[9] J. Criado, A. Gomez, E. Muñoz, and E. Calleja, *Novel method to determine capture crosssection activation energies by deeplevel transient spectroscopy techniques*. Appl. Phys. Lett. **52** 660-661 (1988).

[10] A. Telia, B. Lepley, and C. Michel, *Experimental analysis of temperature dependence of deeplevel capture crosssection properties at the Au oxidized InP interface*. J. Appl. Phys. **69** 7159-7165 (1991).

[11] D. Cavalcoli, A. Cavallini, E. Gombia, *Anomalous temperature dependence of deep-level-transient-spectroscopy peak amplitude*. Phys. Rev. B **56** 14890-14892 (1997).

[12] W. Mtangi, F.D. Auret, C. Nyamhere, P.J. Janse van Rensburg, M. Diale, and A. Chawanda, *Analysis of temperature dependent I-V measurements on Pd/ZnO Schottky barrier diodes and the determination of the Richardson constant*. Physica B **404** 1092-1096 (2009).

[13] C. van Opdorp. *Evaluation of doping proles from capacitance measurements*. Solid State Electron., **11** 397 (1968).

[14] P. Blood and J.W. Orton. *The Electrical Characterization of Semiconductors: Majority Carriers and Electron States*, volume 1. Academic Press, US, 1992.

[15] F. Greuter and G. Blatter, *Electrical properties of grain boundaries in polycrystalline compound semiconductors*. Semicond. Sci. Technol. **5** 111-137 (1990).

Summary

As-grown melt grown single crystal ZnO samples contain three prominent deep level defects, E1, E2 and E3. The E1 and E3 deep levels are observed in material grown using different techniques. This indicates that these defects are common in ZnO. However, the identity of these particular defects is not known yet. The E2 defect has been observed to be dependent on material growth technique as it has not been observed in all the other materials grown using other techniques except in SCVT and melt grown samples used in this study. From the temperature dependence of the capture cross-section of the E3 peak, a capture barrier energy could not be calculated using the approach by Henry and Lang [13]. This is due to the fact that the capture process of the E3 could not be described by a single exponential filling of a defect state as would be the case for a simple capture barrier of an isolated point defect.

References

1. W. Mtangi, F. D. Auret, P. J. Janse van Rensburg, S. M. M. Coelho, M. J. Legodi, J. M. Nel, W. E. Meyer, and A. Chawanda, J. Appl. Phys. **110**, 094504 (2011)
2. M. Grundmann, H.von. Wenckstern, R. Pickenhain, Th. Nobis, A. Rahm, M. Lorenz, Superlattices and Microstruct. **38**, 317 (2005)
3. W. Mtangi, F. D. Auret, W. E. Meyer, M. J. Legodi, P. J. Janse van Rensburg, S. M. M. Coelho, M. Diale, and J. M. Nel, J. Appl. Phys. **111**, 094504 (2012)
4. F. D. Auret, J. M. Nel, M. Hayes, L. Wu, W. Wesch, E. Wendler, Superlattices and Microstruct. **39**, 17 (2006)
5. F. D. Auret, S. A. Goodman, M. Hayes, M. J. Legodi, H. A. van Laarhoven, and D. C. Look, Appl. Phys. Lett. **79**, 3074 (2001)
6. H. von Wenckstern, R. Pickenhain, H. Schmidt, M. Brandt, G. Biehne, M. Lorenz, M. Grundmann, and G. Brauer, Appl. Phys. Lett. **89**, 092122 (2006)
7. V. Quemener, L. Vines, E. V. Monakhov, and B. G. Svensson, Int. J. Appl. Ceram. Technol. **8**, 1017 (2011)
8. J. C. Simpson, and J. F. Cordaro, J. Appl. Phys. **63**, 1781 (1988)
9. A. Y. Polyakov, N. B. Smirnov, E. A. Kozhukhova, V. I. Vdovin, K. Ip, Y. W. Heo, D. P. Norton, and S. J. Pearton, Appl. Phys. Lett. **83**, 1575 (2003)
10. H. von Wenckstern, G. Biehne, M. Lorenz, M. Grundmann, F. D. Auret, W. E. Meyer, P. J. Janse van Rensburg, M. Hayes and J. M. Nel, J. Korean Physical Society, **53**, 2861 (2008)
11. F. D. Auret, S. A. Goodman, M. Hayes, M. J. Legodi, H. A. van Laarhoven, and D. C. Look, J. Phys.:Condens. Matter. **13**, 8989 (2001)
12. W. Mtangi, F. D. Auret, C. Nyamhere, P. J. Janse van Rensburg, M. Diale, and A. Chawanda, Physica B, **404**, 1092 (2009)
13. C. H. Henry and D. V. Lang, Phys. Rev. B, **15**, 989 (1977)

6.2 Electron-beam induced defects

Introduction

Fabrication of stable rectifying contacts on ZnO has been a problem since the early discovery of the material. Of late reports on highly stable and rectifying contacts on ZnO have been published after hydrogen peroxide treatment [1,2,3,4]. Of concern is the quality of the contacts in terms of barrier height, reverse current, degree of rectification and dominant current transport mechanisms. Some reports have indicated the dependence of contact quality on metal work functions where the focus has been on measured barrier heights. Theoretically, metals with high work functions are expected to produce contacts with high barrier heights. However, reports on metal/ZnO contacts have indicated the independence of barrier heights on metal work functions with most reported barrier heights ranging between 0.60 – 0.80 eV [5,6]. This has been explained as an effect caused by an oxygen vacancy that is situated at an energy level of 0.70 eV below the minimum of the conduction band that pins the ZnO Fermi level and the free energy of metal oxide formation [7].

Other reports have indicated the dependence of contact quality on the deposition technique where focus has been shifted to the defects introduced in the material during contact fabrication. Defects introduced during contact fabrication lead to poor rectification of devices, e.g. reduction in free carrier concentration and high leakage currents. Also of importance is the thermal stability of the contacts. It is expected that metals with high melting points and less reactive should form thermally stable contacts on ZnO. With the potential of fabricating devices that can be used in space applications and the ultraviolet region, i.e. in high temperature and high radiant conditions, thermally stable devices are required.

Reports on the use of Pt and Ir to fabricate thermally stable and highly inert devices have been published [7, 8]. Since Pt and Ir have high melting points, the most likely contact fabrication techniques to be used are the e-beam and sputter deposition, just to mention a few. Auret *et al.* [9] have investigated the effect of e-beam deposition on GaN samples using Ru. Their report indicates the introduction of defects that affect the IV characteristics of the devices. Mtangi *et al.* [10] have reported the introduction of defects in ZnO after e-beam deposition of Pd contacts. In this section, a discussion of the defects introduced in ZnO by e-beam deposition is outlined.

Results and discussions

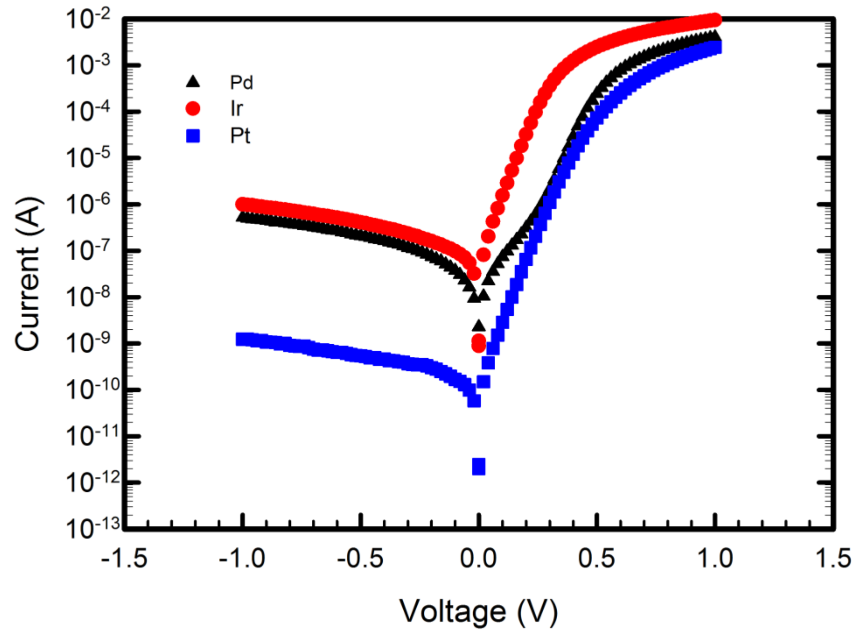

Figure 6.2.1: *A semi-logarithmic IV characteristics of e-beam deposited Schottky contacts measured at 298 K. The dark triangles represent Pd contacts, red circles represent the Ir contacts and the blue squares represent Pt contacts.*

Figure 6.2.1 shows the semi-logarithmic IV plot for the e-beam deposited metal/ZnO contacts obtained at room temperature. Pt contacts reveal a very low reverse current at 1.0 V compared to Pd and Ir contacts. The Pt and Ir contacts reveal the dominance of pure thermionic emission in the voltage range examined while the Pd contacts indicate some generation recombination effects at low voltages, < 0.30 V. The IV characteristics have been analysed by fitting a pure thermionic model to the linear region of the curves. For Pd contacts we have fitted the model to the intermediate region, i.e. $0.30 \text{ V} < V < 0.50$ V. The upper part of the curves shows the dominance of series resistance. Results obtained from fitting a thermionic emission model to the data are shown in Table 6.2.1.

Table 6.2.1: *Values of Schottky barrier height, SBH, ideality factor, series resistance R_s and current at -1.0 V for the e-beam deposited contacts.*

Metal	SBH (eV)	Ideality factor	R_s (Ω)	I (at -1V) (A)
Pd	0.624±0.005	1.66 ± 0.02	110	5.68×10^{-7}
Ir	0.567±0.003	1.28 ± 0.02	70 ± 6	9.09×10^{-7}
Pt	0.710±0.005	1.43 ± 0.04	130 ± 10	1.29×10^{-9}

Pt Schottky contacts indicate a high barrier height compared to Ir and Pd and this justifies the low reverse current measured at 1.0 V while the Ir contacts have a low barrier height, hence the high reverse current measured at 1.0 V. The variation in series resistance can be attributed to the electrical conductivity of the metals. Ir has the highest electrical conductivity of 21.3 x 10^6 S/m, while Pt has the lowest of 9.43 x 10^6 S/m [11], thus the series resistance for the Ir contacts is lower compared to Pd and Pt. Ir contacts also reveal a low ideality factor compared to the Pd and Pt contacts.

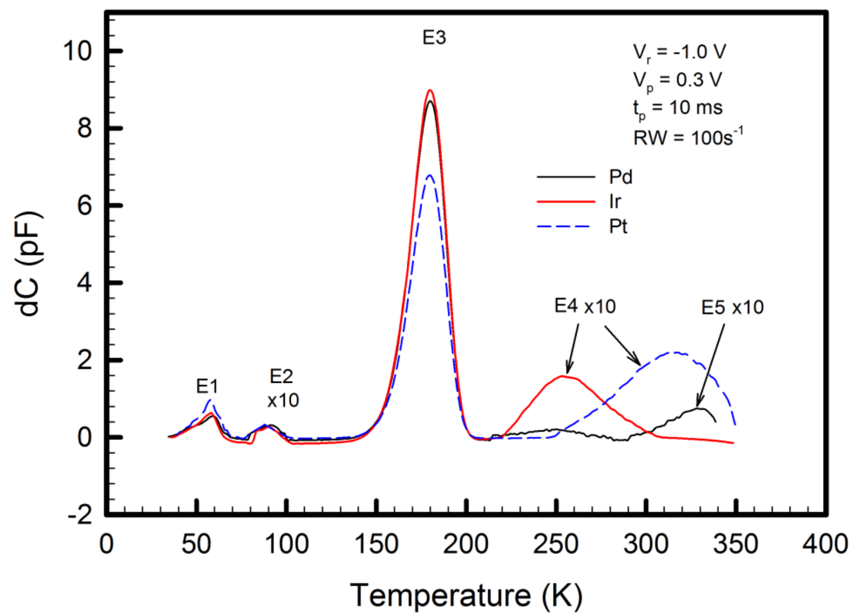

Figure 6.2.2: DLTS spectra for e-beam deposited samples measured at a quiescent reverse bias of -1.0 V, a filling pulse height, V_p = 0.30 V, filling pulse width of 10 ms and rate window of 100 s^{-1} in the 30 – 350 K temperature range. The dark line represents Pd contacts, red line represents Ir contacts and blue dashed line represents Pt contacts

Figure 6.2.2 shows the DLTS spectra obtained for the e-beam deposited contacts. All the samples reveal the presence of three prominent peaks as has also been observed and reported by [10,12]. The fourth peak in all samples is the e-beam induced defect [10]. However the peaks are broad indicating that they may consist of two or more energy levels which are closely spaced or defects with a continuous energy distribution as has been observed by Auret *et al*. [13] in GaAs. Figure 6.2.3 shows the Arrhenius plots obtained from the DLTS peaks.

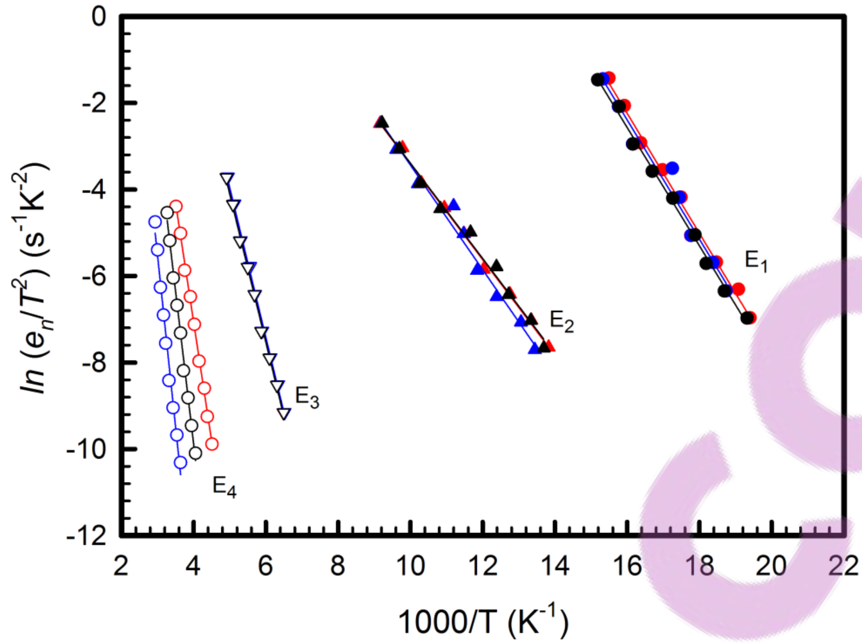

Figure 6.2.3: Arrhenius plots for the e-beam deposited Schottky contacts. Dark symbols represent Pd contacts, red symbols represent Ir contacts and blue symbols represent Pt contacts.

The energy levels obtained from the Arrhenius plots together with the estimated capture cross sections are shown in Table. 6.2.2.

Table 6.2.2: *Values of energy levels and capture cross section for the e-beam deposited contacts. Energy levels are measured below the minimum of the conduction band.*

Metal	E1 (eV)	Capture cross section $\times10^{-12}$ (cm^2)	E2 (eV)	Capture cross section $\times10^{-17}$ (cm^2)	E3 (eV)	Capture cross section $\times10^{-15}$ (cm^2)	E4 (eV)	Capture cross section (cm^2)
Pd	0.12	3.73	0.10	3.10	0.30	7.20	0.60	1.43×10^{-12}
Ir	0.12	6.88	0.10	3.27	0.30	8.62	0.48	5.02×10^{-14}
Pt	0.12	5.20	0.10	8.69	0.30	9.48	0.69	1.37×10^{-12}

Defects labelled E1, E2 and E3 can be said to be native to ZnO as they have been observed in ZnO grown by different techniques as has been discussed in the previous section.

The E4 defect that has been introduced during e-beam deposition can be attributed to stray electrons that originate at the filament and are not focused onto the metal since the filament is not a true point source of electrons [9] and also some other negatively charged ionized gas particles. The average energy level for the E4 defect differs significantly from metal to metal. The observed differences might be due to the differences in the chemical nature and energy of the ionized particles that are causing the damage or possibly E4 consists of defects with a

Bestpfe.com

continuous energy distribution. Since the metals used have different melting points, the current used to produce the electron beam so as to melt the metals also varies and thus the particles ionized together with their speeds towards the sample during the deposition process can also vary.

The extent of the damage caused by the ionized particles, has been further investigated by performing a depth profile of the E4 peak. Figure 6.2.4 shows the results obtained from the three samples.

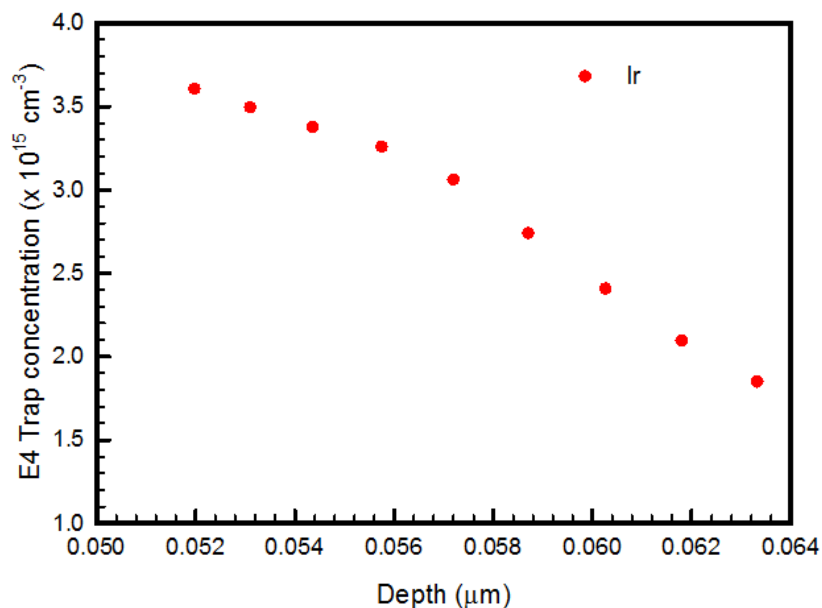

Figure 6.2.4a: *E4 trap concentration versus depth for the Ir Schottky contacts measured at a constant reverse bias of 1.0 V with increasing filling pulse height in steps of 0.05 V*

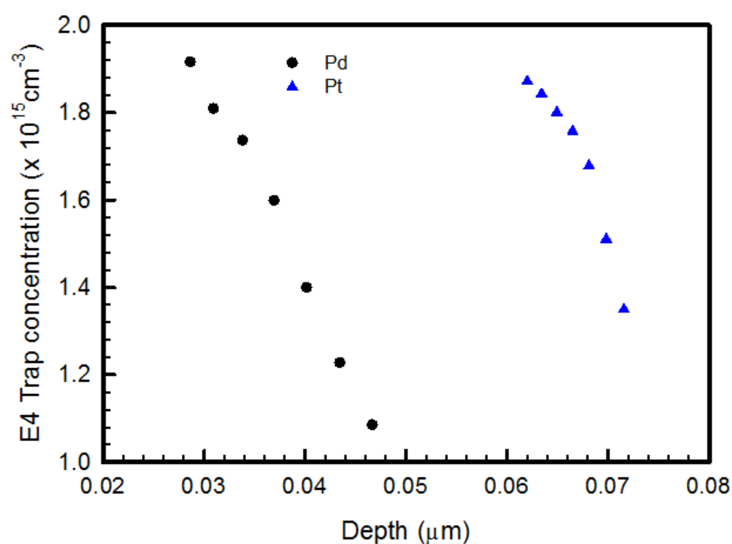

Figure 6.2.4b: *E4 trap concentration versus depth for the Pt and Pd Schottky contacts measured at a constant reverse bias of 1.0 V with increasing filling pulse height in steps of 0.05 V*

The concentration of the E4 defect decreases as we go deeper into the bulk of the semiconductor for all the three metals used. The particles that cause damage during Pd deposition can penetrate a depth shallower than those during Pt and Ir deposition. Since high melting point metals require high current beams compared to those with low melting points, we have higher chances of ionizing more impurities from the metal itself and also those present in the system closer to the filament during deposition. Another possibility is, some ionized metal atoms can gain enough energy during collisions with other particles to cause damage to the ZnO surface [9]. Thus the concentration of the E4 for Ir is higher compared to Pd and Pt. This depth profile was performed at a constant reverse bias of 1.0 V and increasing the pulse height in steps of 0.05 V.

A region of up to 64 nm below the interface has been probed for Ir contacts. The concentration has been observed to decrease from 3.6 x 10^{15} cm^{-3} at a depth of 52 nm to 1.8 x 10^{15} cm^{-3} at 64 nm. Using the same measurement conditions, we have managed to probe a region up to 72 nm below the interface for Pt contacts. The concentration has been observed to decrease from 1.9 x 10^{15} cm^{-3} at 62 nm to 1.3 x 10^{15} cm^{-3} at 72 nm. For Pd, a depth of 46 nm below the interface has successfully been examined. The concentration has decreased from 1.9 x 10^{15} cm^{-3} at 29 nm to 1.1 x 10^{15} cm^{-3} at 46 nm. A similar trend of a decrease in defect concentration with increase in depth has also been observed by [9].

A detailed summary of the e-beam induced defects in ZnO is presented in the article obtained from the link below.

Publication 2: A comparative study of the electrical properties of Pd/ZnO Schottky contacts fabricated using electron beam deposition and resistive evaporation techniques

http://dx.doi.org/10.1063/1.3658027

Summary

Stable rectifying Schottky contacts have been successfully fabricated on ZnO using the electron-beam deposition technique. However, this contact fabrication technique introduces defects on the surface of the material that affect device operation as they contribute to high reverse currents. These deep level defects have successfully been characterized using DLTS. From the defect depth profiling, it has been observed that e-beam deposition introduces defects with high concentrations closer to the surface of the semiconductor. The cause of the E4 defect has been explained as possibly due to ionized impurities from the metals, stray electrons from the filament itself that are not focused towards the metal. These electrons can collide with ionized impurities transferring their energy resulting in impurities impinging onto the sample and also other materials within the system closer to the filament.

References

1. R. Schifano, E. V. Monakhov, B. G. Svensson, S. Diplas, Appl. Phys. Lett. **94**, 132101 (2009)
2. S. Lee, Y. Lee, D. Y. Kim, T W Kang, Appl. Phys. Lett. **96**, 142102 (2010)
3. S.H. Kim, H.K. Kim, S-W Jeong, T-Y Seong, Superlatt. and Microstruct. **39**, 211 (2006)
4. W. Mtangi, F.D. Auret, C. Nyamhere, P.J. Janse van Rensburg, M. Diale, A. Chawanda, Phys. B, **404**, 1092 (2009)
5. U. Ozgur, Y. I. Alivov, C. Lui, A. Teke, M. A. Reshchikov, S. Dogan, V. Avrutin, S. J. Cho, and H. Morkoc, J. Appl. Phys. **98**, 041301 (2005)
6. K. Ip, G. T. Thaler, H. S. Yang, S. Y. Han, Y. J. Li, D. P. Norton, S. J. Pearton, S. W. Jang, and F. Ren, J. Cryst. Growth, **287**, 149 (2006)
7. M. W. Allen, S. M. Durbin, Appl. Phys. Lett. **92**, 122110 (2008)
8. S J Young, L-W Ji, S J Chang, Y P Chen, S-M Peng, Semicond. Sci. Technol. **23**, 085016 (2008)
9. F.D. Auret, S.A. Goodman, G. Myburg, F.K. Koschnick, J.-M. Spaeth, B. Beaumont, P. Gibart, Phys. B, **84**, 273 (1999)
10. W. Mtangi, F.D. Auret, P.J. Janse van Rensburg, S. M. M. Coelho, M. J. Legodi, J.M. Nel, W.E. Meyer, J. Appl. Phys. **110**, 094504 (2011)
11. CRC Handbook of Chemistry and Physics, 80th Edn. 1999-2000
12. F.D. Auret, J.M. Nel, M. Hayes, L. Wu, W. Wesch, E. Wendler, Superlatt. and Microstruct. **39**, 17 (2006)
13. F. D. Auret, G. Myburg, L. J. Bredell, W. O. Barnard, and H. W. Kunert, Mat. Sci. Forum, **83**, 1499 (1992)

6.3 Annealing studies of ZnO using Hall Effect, IV and DLTS

Introduction

Annealing of semiconductor crystals is an important aspect to consider during material processing for device fabrication and characterization. This is due to the fact that it can help recover, activate dopant impurities and in some cases remove defects in crystals that are native or that would have been intentionally introduced. Due to the above-mentioned effects, annealing of crystals results in the modification of the electrical and optical properties of the material and hence fabricated devices. In the case of defects that are already within the material, a study of the annealing kinetics of specific defects can give valuable information on how to improve the efficiency of devices if the optimal conditions have been identified. In ZnO, an effort to identify the nature and origins of the intrinsic defects has been made. Of all the experimental techniques used, none have managed to give the identity of these defects as they have failed to alter the properties of these intrinsic defects. These processes include among others, ion implantation and particle irradiation. Instead, these techniques tend to introduce other electrically active states within the bandgap of the semiconductor. An understanding of the nature of these defects and the origins of the n-type conductivity of the material is essential. This will help in the realization of p-type ZnO since one will have control over the native defects and hence the conductivity of ZnO. Currently, the realization of p-type material is still a challenge since native defects are believed to have self-compensation behaviours. Since the techniques that have been employed have failed to give information to identify the nature of defects in ZnO, one would need to assume that annealing of crystals might give an insight into their identification. However, not much is known about the annealing behaviour of ZnO. In this section, annealing of bulk, melt grown single crystal ZnO samples is studied using the Hall effect, current-voltage and DLTS measurements.

6.3.1 Hall effect studies

Introduction

This technique was employed to characterize the shallow level defects introduced in the material through annealing. This is because the Hall effect technique is a surface sensitive technique. Detailed information pertaining to the study of shallow level defects in ZnO with annealing is obtained from the publication in the link below.

Publication 3: Annealing and surface conduction on hydrogen peroxide treated bulk melt-grown, single crystal ZnO

http://dx.doi.org/10.1016/j.physb.2011.09.101

This publication outlines the experimental procedure used and the results that were obtained together with the conclusions that were drawn from the study.

6.3.2 IV measurements

Introduction

It has been mentioned that annealing affects the electrical properties of devices, such an effect is demonstrated in this section. The results and conclusions drawn from the study are given in the publication obtained from the link below.

Publication 4: Thermal annealing behaviour of Pd Schottky contacts on melt-grown single crystal ZnO studied by IV and CV measurements

http://dx.doi.org/10.1016/j.mseb.2011.10.003

Summary

Annealing of metal/ZnO structures has proved to have an adverse effect on the electrical characteristics of devices. The devices have shown an increase in reverse leakage current with increase in annealing temperature. Annealing the devices at temperatures beyond 550°C results in them losing all their rectification behaviours. An increase in the net doping concentration with increase in annealing temperature has also been observed. The current transport mechanism across the metal/semiconductor interface has been modified from pure thermionic emission to thermionic field emission.

6.3.3 DLTS Studies

Introduction

It has been observed that the Schottky contacts on ZnO lose their rectification behaviour after annealing at high temperatures. At the same time, it has also been mentioned that the depletion layer of the metal/semiconductor interface is modified by annealing. This is a limitation for the determination and characterization of defects in ZnO at high temperatures. In this section, a study on the annealing induced deep level defects in ZnO is performed by annealing the as-received material before contact fabrication. This method allows for the determination of deep level defects even at high annealing temperatures. The Schottky contacts were fabricated after the annealing of the material. This section gives information of deep level defects introduced after annealing the samples in different ambient conditions and temperatures. The results of this study will give an idea of what these defects might relate to by considering those that anneal in or out under the different ambient conditions.

Results and discussions

6.3.3.1 Vacuum annealing

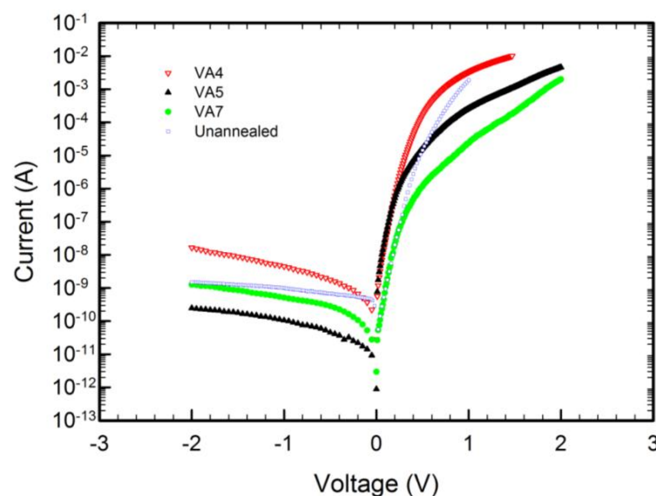

Figure 6.3.3.1.1: Semi-logarithmic IV characteristic of Pd Schottky contacts deposited on vacuum annealed ZnO. The characteristics were recorded at 298 K in the dark.VA4, VA5 and VA7 indicate the annealing temperature of 400°C, 500°C and 700°C, respectively.

Figure 6.3.3.1.1 shows the semi-logarithmic IV characteristics of Pd Schottky contacts deposited on vacuum annealed ZnO samples. It can be clearly observed that annealing modifies the electrical characteristics of the contacts. Parameters extracted from these IV characteristics by fitting the linear region of the forward IV curves are presented in Table 6.3.3.1.1.

Table 6.3.3.1.1: *Average values of Schottky barrier height, SBH, ideality factor, series resistance R_s, and the free carrier concentration from CV depth profile, for the un-annealed and vacuum annealed ZnO samples.*

Annealing Temperature(°C)	SBH (eV) IV	Ideality factor	R_s (Ω)	SBH (eV) CV	N_{dCV} $10^{17}cm^{-3}$
-------	0.721±0.002	1.43 ± 0.01	190	1.16±0.02	2.63±0.03
400	0.58±0.02	1.9 ± 0.3	112±20	1.13±0.02	1.82±0.05
500	0.74±0.05	1.6 ± 0.1	137±30	1.04±0.02	1.48±0.03
700	0.70±0.05	1.3± 0.1	137±20	1.13±0.02	1.94±0.02

Samples annealed at 400°C show a decrease in the average IV barrier height compared to the un-annealed samples. However the barrier height increases after annealing samples at 700°C. For all the annealing temperatures, the average series resistance decreases as compared to the un-annealed sample. This might be due to surface conduction effects in which carriers find an easier path for current flow resulting in low resistance being measured on the samples. The average CV barrier height has been observed to be larger than the IV barrier height. This trend has been observed in many metal/semiconductor contacts and has been explained as due to the influence of thermionic field emission on the charge transport through the interface [1], the existence of an interfacial layer or interface states [2, 3] and also edge leakage currents[4]. From the CV depth profiles, it has been observed that the net doping concentration for all annealing temperatures is less than that of the un-annealed samples.

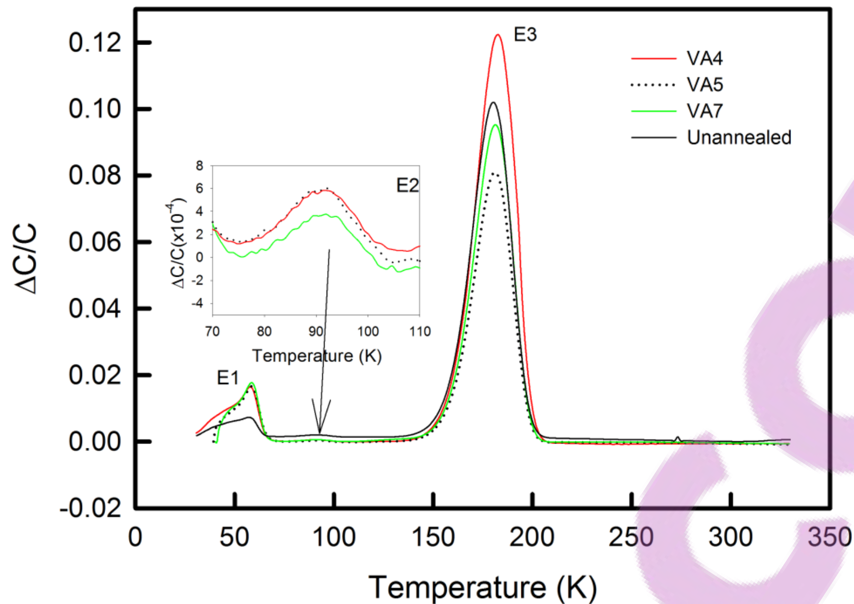

Figure 6.3.3.1.2: DLTS spectra obtained from Pd Schottky contacts deposited on vacuum annealed ZnO. The spectra were recorded at a quiescent reverse bias of -2.0 V, filling pulse of 0.30 V, filling pulse width of 2 ms and rate window of 100s^{-1} in the temperature range 30 – 350 K. VA4, VA5 and VA7 indicate the annealing temperature of 400°C, 500°C and 700°C, respectively. The insert shows the E2 peak.

Figure 6.3.3.1.2 shows the DLTS spectra obtained from the vacuum annealed samples. These spectra were recorded at a rate window of 100 s^{-1}. The annealed samples show three peaks which have been observed in the un-annealed samples. This shows that vacuum annealing does not introduce new defects in bulk-melt grown single crystal ZnO. At the same time, it must be stated that vacuum annealing does not remove deep level defects within the investigated temperature range.

Arrhenius plots shown in Figure 6.3.3.1.3 have been used to extract the defect signatures, i.e. the estimated activation enthalpy and apparent capture cross-section. These values are presented in Table 6.3.3.1.2. The activation enthalpy of the E1 peak has been estimated to be between 94 – 120 meV. This large variation in the activation enthalpy is due to the difficulty in an accurate determination of the value as this defect has a very strong electric field dependence and is also observed very close to the freeze-out region of ZnO indicated in the capacitance temperature scan of Figure 6.3.3.1.4. This defect has been suggested to be Zn vacancy or O_i related [5]. The same explanation can be given for the values of the apparent capture cross-section. The E2 peak has an activation enthalpy that varies from 99 – 103 meV and an apparent capture cross-section of (0.5 – 1) $\times 10^{-16}$ cm^2. Its identity is not known yet.

The E3 peak has an activation enthalpy of 291 – 304 meV and a capture cross-section that varies from (0.5 – 3) $\times 10^{-14}$ cm^2. Its identity is still not clear as illustrated in Table 6.1.1. The E3 peak shows a capture cross-section that is temperature dependent as observed from an increase in the DLTS peak height with increase in rate window frequency.

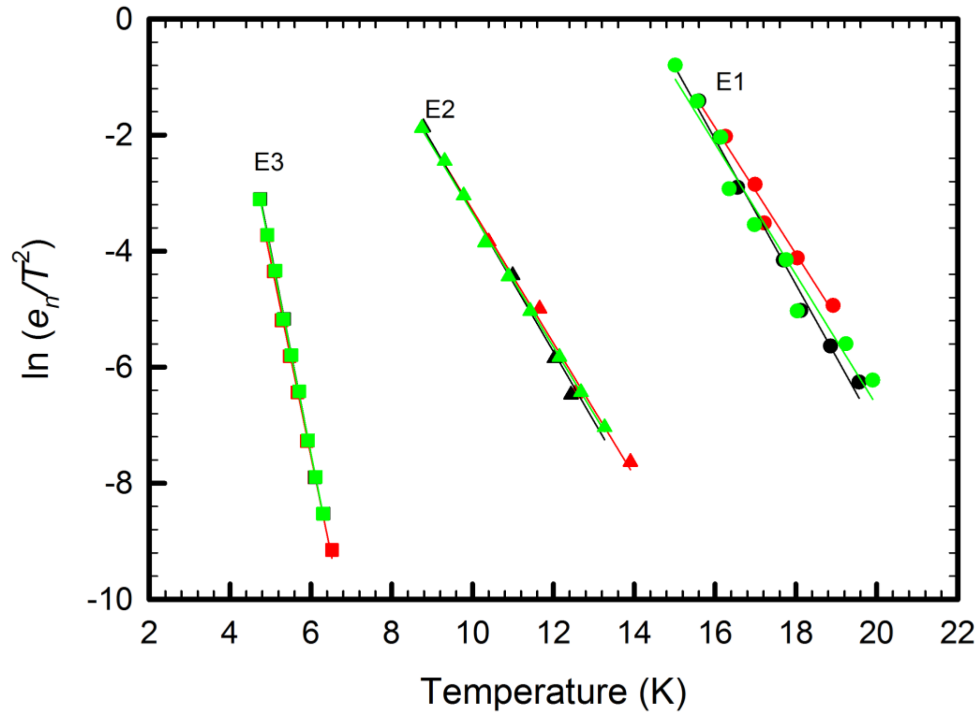

Figure 6.3.3.1.3: Arrhenius plots obtained from Pd Schottky contacts deposited on vacuum annealed ZnO. Red symbols represent samples annealed at 400°C, black symbols are for 500°C annealed samples and green symbols are for the 700°C annealed samples.

Table 6.3.3.1.2: *Values of activation enthalpy and capture cross section for the Pd Schottky contacts deposited on un-annealed and vacuum annealed ZnO. The activation enthalpy is measured relative to the minimum of the conduction band.*

Annealing temperature (°C)	E1 (meV)	Capture cross section (cm^2)	E2 (meV)	Capture cross section (cm^2)	E3 (meV)	Capture cross section (cm^2)
No anneal	120 ± 20	5×10^{-12}	100 ± 20	1×10^{-16}	300 ± 20	3×10^{-14}
400	94 ± 10	9×10^{-14}	99 ± 10	5×10^{-17}	291 ± 10	5×10^{-15}
500	108 ± 10	9×10^{-13}	103± 20	9×10^{-17}	304 ± 20	1×10^{-14}
700	97 ± 10	1×10^{-13}	99 ± 10	5×10^{-17}	301 ± 10	1×10^{-14}

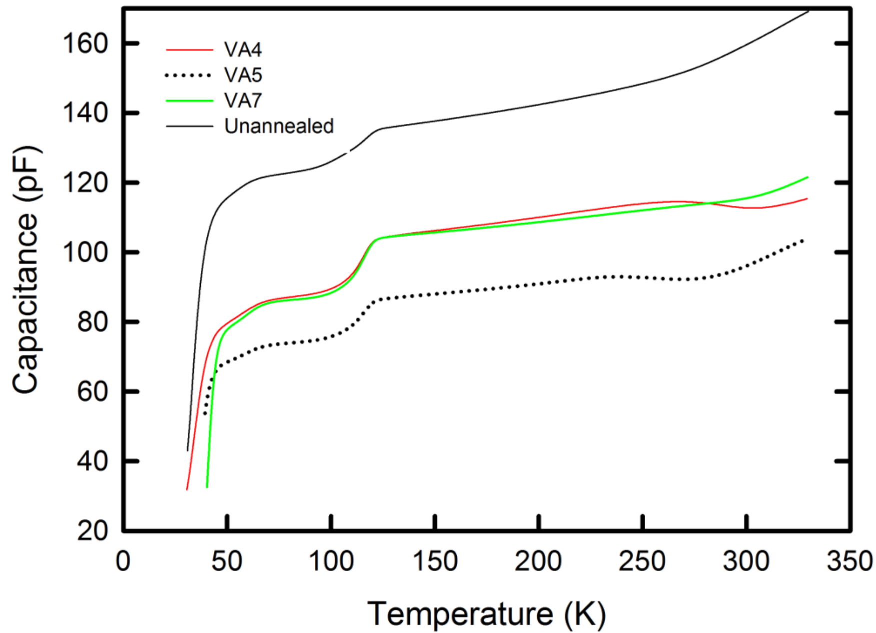

Figure 6.3.3.1.4: Capacitance-temperature scan obtained from Pd Schottky contacts deposited on vacuum annealed ZnO. The spectra were recorded at a quiescent reverse bias of -2.0 V in the temperature range 30 – 350 K. VA4, VA5 and VA7 indicate the annealing temperature of 400°C, 500°C and 700°C, respectively.

Figure 6.3.3.1.4 shows the variation of capacitance with temperature for the vacuum annealed ZnO samples. From these scans, it can be concluded that the freeze-out for ZnO begins around 50 K, where the capacitance drops sharply with a decrease in temperature.

BESTPFE.COM
List of research project topics and materials

6.3.3.2 Oxygen annealing

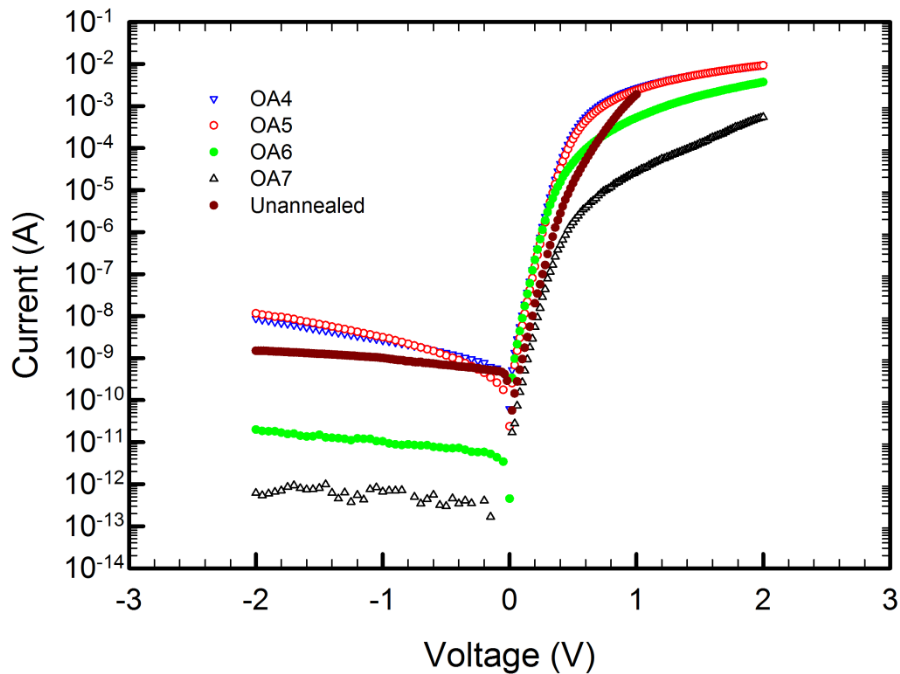

Figure 6.3.3.2.1: Semi-logarithmic IV characteristic of Pd Schottky contacts deposited on oxygen annealed ZnO. The characteristics were recorded at 298 K in the dark.OA4, OA5, OA6 and OA7 indicate the annealing temperature of 400°C, 500°C, 600°C and 700°C, respectively.

The semi-logarithmic IV characteristics for the oxygen annealed ZnO samples indicate a strong dependence on annealing temperature. For the 400°C and 500°C, the characteristics are almost the same to within experimental error. The 700°C annealed samples indicate the lowest leakage current. The leakage current seems to improve with increase in annealing temperature. However, these contacts show a very high series resistance that increases with an increase in annealing temperature. This could be a result of an insulative layer caused by oxygen adsorption during sample annealing. Table 6.3.3.2.1 shows the contact parameters that were obtained from the IV and CV characteristics of the oxygen annealed ZnO samples. As has also been observed with vacuum annealing, the CV barrier height is larger than the average IV barrier height for all annealing temperatures. The net doping concentrations for the annealed samples are also lower compared to that of the as-received samples.

Table 6.3.3.2.1: *Average values of Schottky barrier height, SBH, ideality factor, series resistance R_s, and the free carrier concentration from CV depth profile, for the un-annealed and oxygen annealed ZnO samples.*

Annealing Temperature(°C)	SBH (eV) IV	Ideality factor	R_s (Ω)	SBH (eV) CV	N_{dCV} $10^{17}cm^{-3}$
-------	0.721±0.002	1.43 ± 0.01	190	1.16±0.02	2.63±0.03
400	0.68±0.01	1.44 ± 0.07	143±3	1.09±0.06	1.13±0.04
500	0.65±0.02	1.7 ± 0.2	151±5	0.98±0.04	1.25±0.01
600	0.73±0.02	1.47± 0.06	222±20	1.02±0.03	1.64±0.03
700	0.84±0.02	1.46± 0.06	466±80	1.02±0.02	1.74±0.03

Figure 6.3.3.2.2 shows the DLTS spectra obtained from the oxygen annealed samples. Samples annealed at 400°C, 500°C, 600°C and 700°C indicate the presence of three prominent peaks, similar to those observed in the as-received sample. From the insert shown in the DLTS spectra of Figure 6.3.3.2.3, the 400°C annealed sample shows an extra peak, E4.

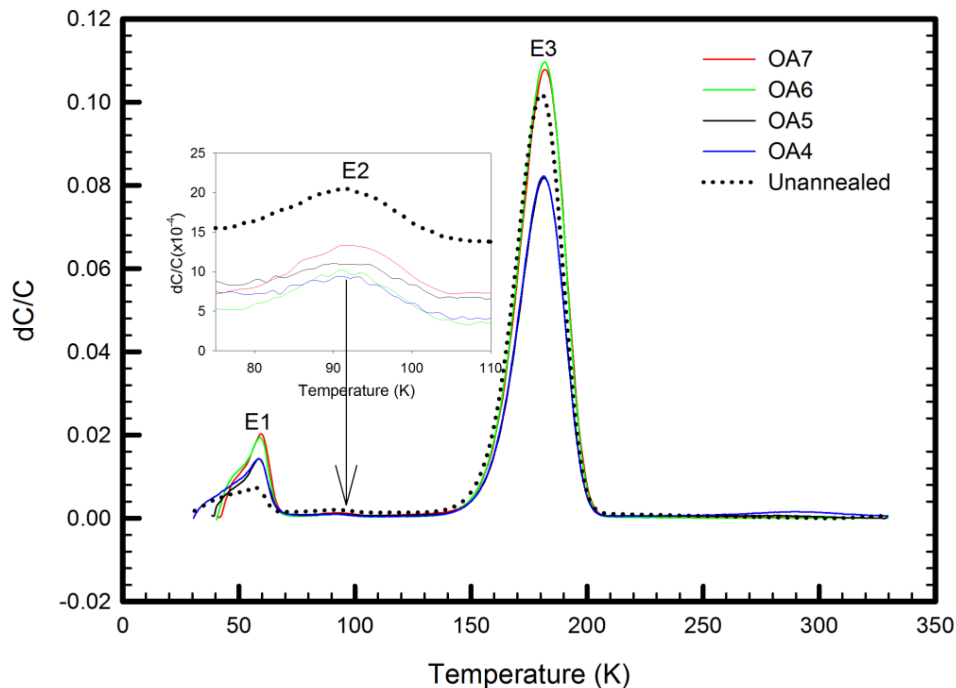

Figure 6.3.3.2.2: DLTS spectra obtained from Pd Schottky contacts deposited on oxygen annealed ZnO. The spectra were recorded at a quiescent reverse bias of -2.0 V, filling pulse of 0.30 V, filling pulse width of 2 ms and rate window of 100s^{-1} in the temperature range 30 – 350 K. OA4, OA5, OA6 and OA7 indicate the annealing temperature of 400°C, 500°C, 600°C and 700°C, respectively. The insert shows the E2 peak.

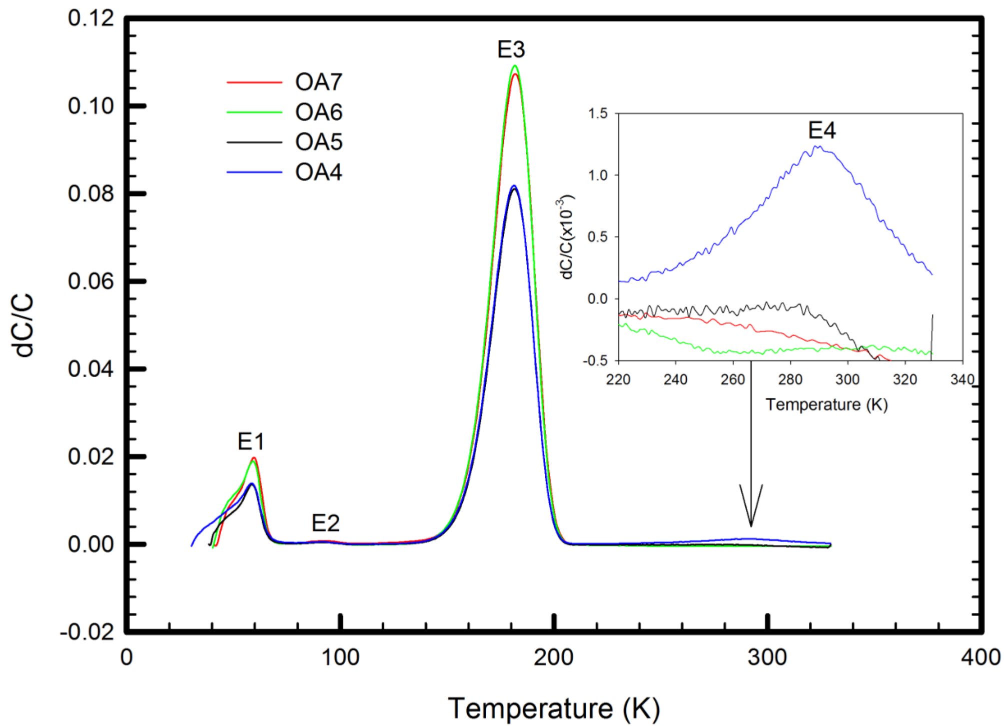

Figure 6.3.3.2.3: DLTS spectra obtained from Pd Schottky contacts deposited on oxygen annealed ZnO. The spectra were recorded at a quiescent reverse bias of -2.0 V, filling pulse of 0.30 V, filling pulse width of 2 ms and rate window of 100 s^{-1} in the temperature range 30 – 350 K. OA4, OA5, OA6 and OA7 indicate the annealing temperature of 400°C, 500°C, 600°C and 700°C, respectively. The insert shows the E4 peak.

The Arrhenius plots shown in Figure 6.3.3.2.4 have been used to calculate the activation enthalpy and apparent capture cross-section for the defects observed in the oxygen annealed ZnO samples. The values obtained from these Arrhenius plots are given in Table 6.3.3.2.2. The activation enthalpy of the E1 defect has been estimated to be 115 – 120 meV and an apparent capture cross-section that varies from (2 – 5) × 10^{-12} cm^2. E2 with an estimated activation enthalpy of 94 – 100 meV has an apparent capture cross-section of (0.3 – 1) × 10^{-16} cm^2. As also observed in the vacuum annealed samples, the activation enthalpy of E3 has been estimated to be 294 – 300 meV and an apparent capture cross-section that varies from (0.7 – 3) × 10^{-14} cm^2. The E4 defect observed in the 400°C annealed samples has an activation enthalpy of 596 meV and an apparent capture cross-section of 4 × 10^{-14} cm^2. Its identity is not known yet.

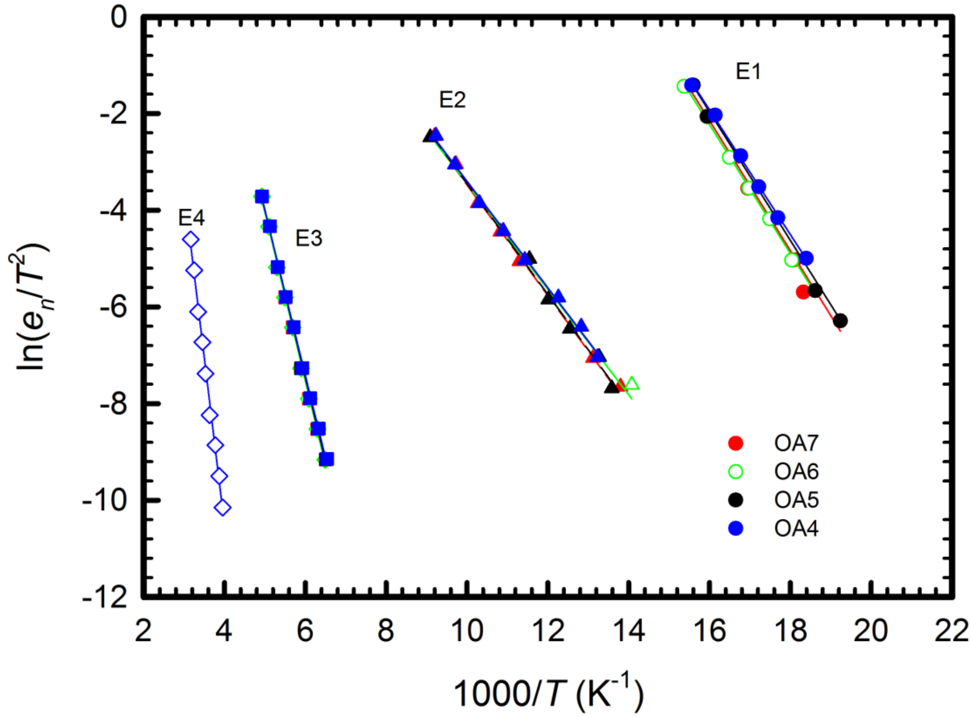

Figure 6.3.3.2.4: Arrhenius plots obtained from Pd Schottky contacts deposited on oxygen annealed ZnO. Red symbols represent samples annealed at 700°C, green symbols are for the 600°C annealed samples, black symbols are for 500°C annealed samples and blue symbols are for the 400°C annealed samples. OA4, OA5, OA6 and OA7 indicate the annealing temperature of 400°C, 500°C, 600°C and 700°C, respectively

Table 6.3.3.2.2: *Values of activation enthalpy and capture cross section for the Pd Schottky contacts deposited on un-annealed and oxygen annealed ZnO. The activation enthalpy is measured relative to the minimum of the conduction band.*

Annealing temperature (°C)	E1 (meV)	Capture cross section (cm^2)	E2 (meV)	Capture cross section (cm^2)	E3 (meV)	Capture cross section (cm^2)	E4 (meV)	Capture cross section (cm^2)
No anneal	120 ± 20	5×10^{-12}	100 ± 10	1×10^{-16}	300 ± 20	3×10^{-14}	-------	---------
400	111 ± 10	2×10^{-12}	95 ± 10	3×10^{-17}	294 ± 20	7×10^{-15}	596 ± 10	4×10^{-13}
500	115 ± 20	4×10^{-12}	99 ± 10	4×10^{-17}	300 ± 20	1×10^{-14}	-------	----------
600	115 ± 20	3×10^{-12}	94 ± 10	3×10^{-17}	300 ± 20	1×10^{-14}	-------	---------
700	116 ± 20	4×10^{-12}	99 ± 10	4×10^{-17}	300 ± 20	1×10^{-14}	-------	---------

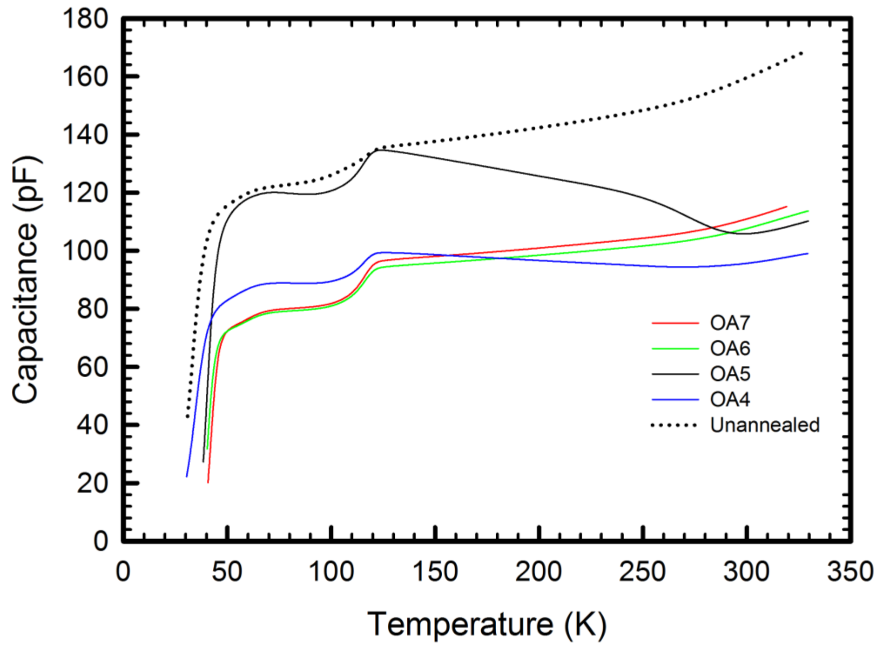

Figure 6.3.3.2.5: Capacitance-temperature scan obtained from Pd Schottky contacts deposited on oxygen annealed ZnO. The spectra were recorded at a quiescent reverse bias of -2.0 V in the temperature range 30 – 350 K. OA4, OA5, OA6 and OA7 indicate the annealing temperature of 400°C, 500°C, 600°C and 700°C, respectively

Figure 6.3.3.2.5 shows the variation of capacitance with temperature for the oxygen annealed ZnO samples. From these scans, it can be concluded that the freeze-out for ZnO begins around 50 K, where the capacitance drops sharply with a decrease in temperature. The Zn_i cannot be observed since the Fermi level is lowered. This lowering is due to the fact that the acceptor concentration for all the annealed samples is now too high, as compared to the concentration of the Zn_i. This is confirmed by the sharp decrease in capacitance in the CT scans. Furthermore, an effective mass donor is formed whose concentration depends on the annealing ambient and temperature, being higher for high annealing temperatures and lower for low annealing temperatures. There is also a possibility that the Zn_i is annealed out and a new shallow donor with high concentration is observed as has been reported by von Wenckstern *et al.* [5] and Mtangi *et al.*[6]. The 400°C and 500°C annealed samples however show a decrease in capacitance with increasing temperature. This has been observed and explained as due to the presence of surface related defects which coexist with deep level defects whose response can only be observed with low frequencies [7].

6.3.3.3 Argon annealing

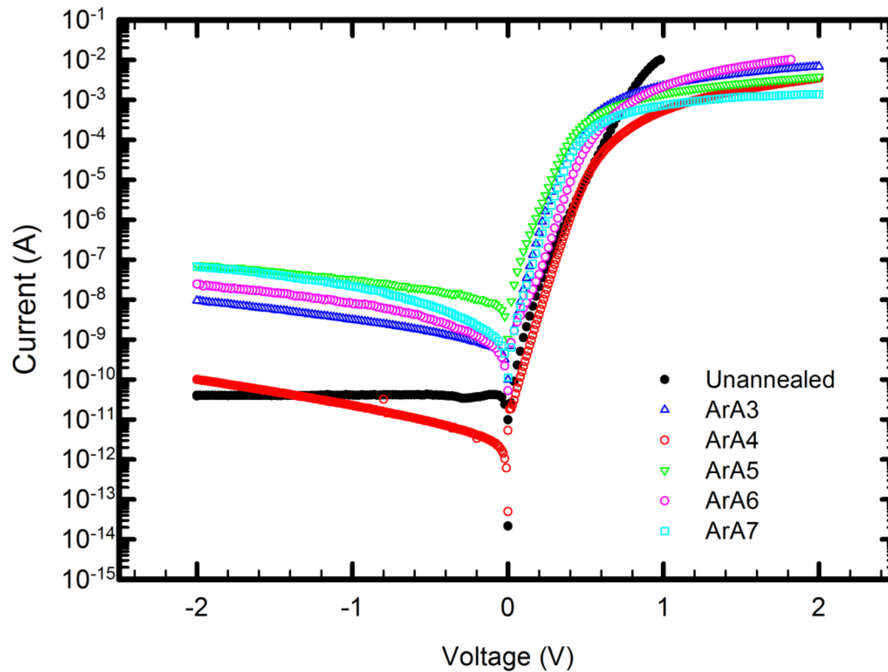

Figure 6.3.3.3.1: Semi-logarithmic IV characteristic of Pd Schottky contacts deposited on argon annealed ZnO. The characteristics were recorded at 298 K in the dark. ArA3, ArA4, ArA5, ArA6 and ArA7 indicate the annealing temperature of 300°C, 400°C, 500°C, 600°C and 700°C, respectively. Figure adopted from ref [8]

Figure 6.3.3.3.1 illustrates the effects of annealing on the IV characteristics of Pd Schottky contacts deposited on ZnO. The annealed samples yield contacts with very high reverse currents compared to the un-annealed contacts. Of particular interest is the reverse current for the 400°C annealed samples. Even though this current increases, it does not differ much from that of the un-annealed samples. These high reverse currents can be explained by considering the defects that are introduced during annealing of the samples. One would expect the 400°C annealed samples to have a low concentration of defects as compared to the 300°C, 500°C 600°C and 700°C annealed samples since defects can also contribute to high leakage currents in metal/semiconductor contacts.

Parameters obtained from the IV characteristics of Figure 6.3.3.3.1 are given in Table 6.3.3.3.1. These have been obtained by fitting the linear part of the forward IV curves to a pure thermionic emission model. The 400°C annealed samples show a very high barrier height compared to all the annealed samples, hence the observed low leakage current. The annealed samples however show an increase in series resistance of the contacts compared to the un-annealed samples. As has been noted with the vacuum annealed and oxygen annealed

samples, the CV barrier height is larger than the IV barrier height and also the net doping concentration for the annealed samples is lower than that of the un-annealed samples.

Table 6.3.3.3.1: *Average values of Schottky barrier height, SBH, ideality factor, series resistance R_s, and the free carrier concentration from CV depth profile, for the un-annealed and oxygen annealed ZnO samples.*

Annealing Temperature(°C)	SBH (eV) *IV*	Ideality factor	R_s (Ω)	SBH (eV) *CV*	N_{dCV} 10^{16}cm^{-3}
-------	0.74±0.02	1.67 ± 0.01	190	1.16±0.02	26.3±0.3
300	0.70±0.01	1.25 ± 0.07	206±3	1.53±0.06	5.53±0.04
400	0. 81±0.01	1.37 ± 0.07	312±30	1.40±0.06	12.4 ±0.4
500	0.63±0.02	1.72 ± 0.02	391±50	2.55±0.04	6.65±0.01
600	0.74±0.02	1.43± 0.06	110±20	1.45±0.03	10.2±0.03
700	0.73±0.02	1.17± 0.05	(8.4±1)k	0.86±0.02	9.40±0.03

Figure 6.3.3.3.2 shows the DLTS spectra obtained from the un-annealed and argon annealed ZnO samples. The insert shows a new peak observed on the 700°C annealed samples together with the E2 peak. The un-annealed and annealed ZnO samples contain three prominent peaks, E1, E2 and E3. Figure 6.3.3.3.3 also shows DLTS spectra for the un-annealed and argon annealed samples. The insert shows the annealing induced E4 peak on the 300°C, 500°C and 600°C annealed samples. Interesting enough, the 400°C does not show any annealing induced deep level defects.

With all the other annealing temperatures examined in this study, the E4 is observed up to an annealing temperature of 600°C after which it disappears and Ex is induced. The identities of the E4 and Ex deep levels are not known yet. The fact is; E4 and Ex are not thermally induced defects, but they are ambient related defects as they have not been observed in vacuum annealing nor in 300°C, 500°C, 600°C and 700°C oxygen annealing. The Arrhenius plots of Figure 6.3.3.3.4 have been used to calculate the estimated activation enthalpy and capture cross-section for the 700°C annealed samples. The values of the activation enthalpy and apparent capture cross-section for the peaks are given in Table 6.3.3.3.2.

The activation enthalpy of the Ex peak has been estimated to be 167 meV with an apparent capture cross-section of 1×10^{-16} cm^2. A defect with an energy level similar to that of Ex was observed in melt-grown samples by Ye *et al.* [9] after oxygen implantation and subsequent annealing at 750°C in air and Gu *et al* [10] after annealing nitrogen implanted ZnO samples.

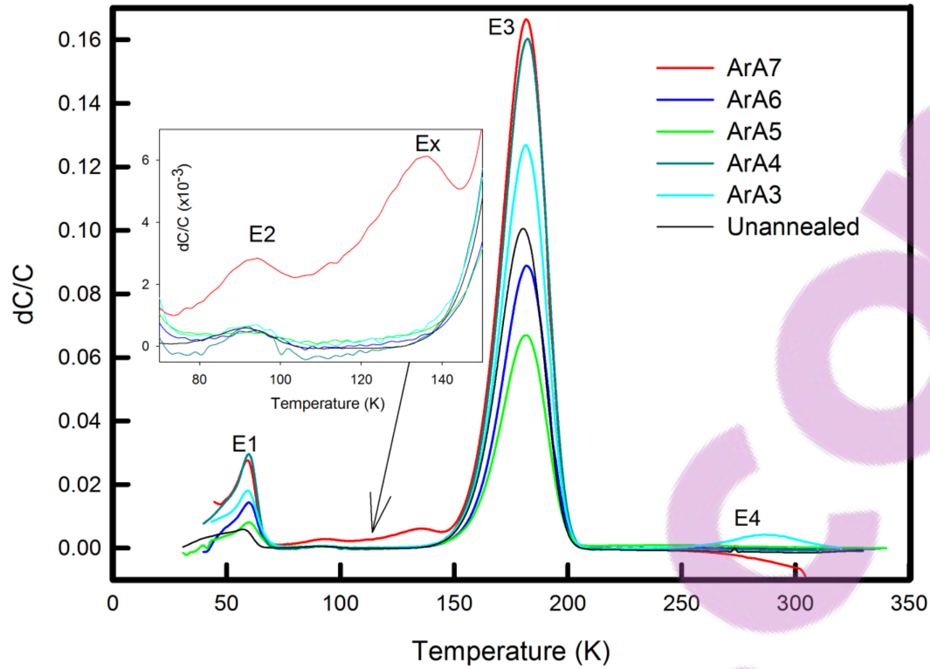

Figure 6.3.3.3.2: DLTS spectra obtained from Pd Schottky contacts deposited on argon annealed ZnO. The spectra were recorded at a quiescent reverse bias of -2.0 V, filling pulse of 0.30 V, filling pulse width of 2 ms and rate window of 100s^{-1} in the temperature range 30 – 350 K. The insert shows the E2 and Ex peaks. ArA3, ArA4, ArA5, ArA6 and ArA7 indicate the annealing temperature of 300°C, 400°C, 500°C, 600°C and 700°C, respectively

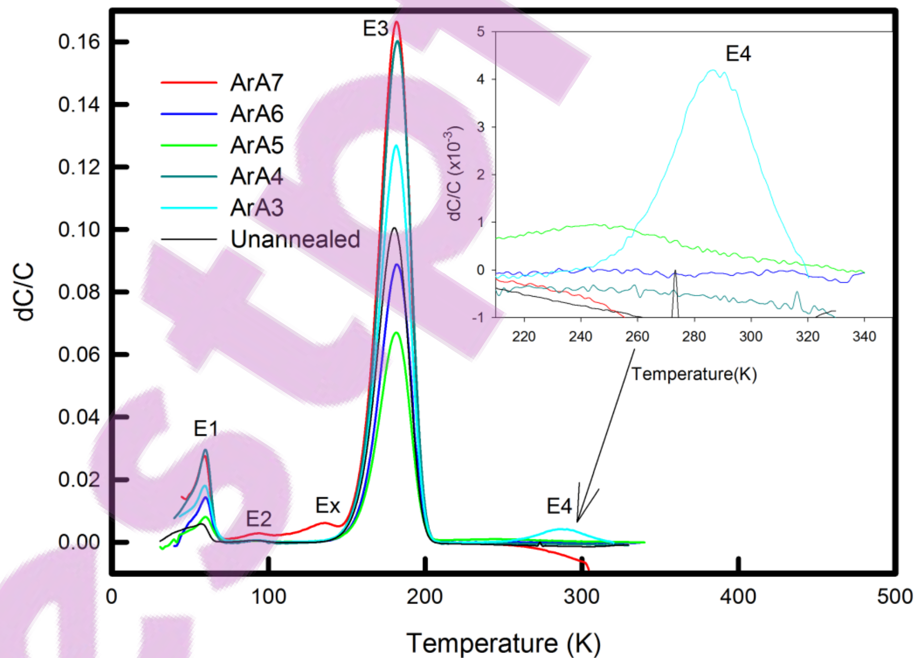

Figure 6.3.3.3.3: DLTS spectra obtained from Pd Schottky contacts deposited on argon annealed ZnO. The spectra were recorded at a quiescent reverse bias of -2.0 V, filling pulse of 0.30 V, filling pulse width of 2 ms and rate window of 100s^{-1} in the temperature range 30 – 350 K. The insert shows the E4 peak. ArA3, ArA4, ArA5, ArA6 and ArA7 indicate the annealing temperature of 300°C, 400°C, 500°C, 600°C and 700°C, respectively

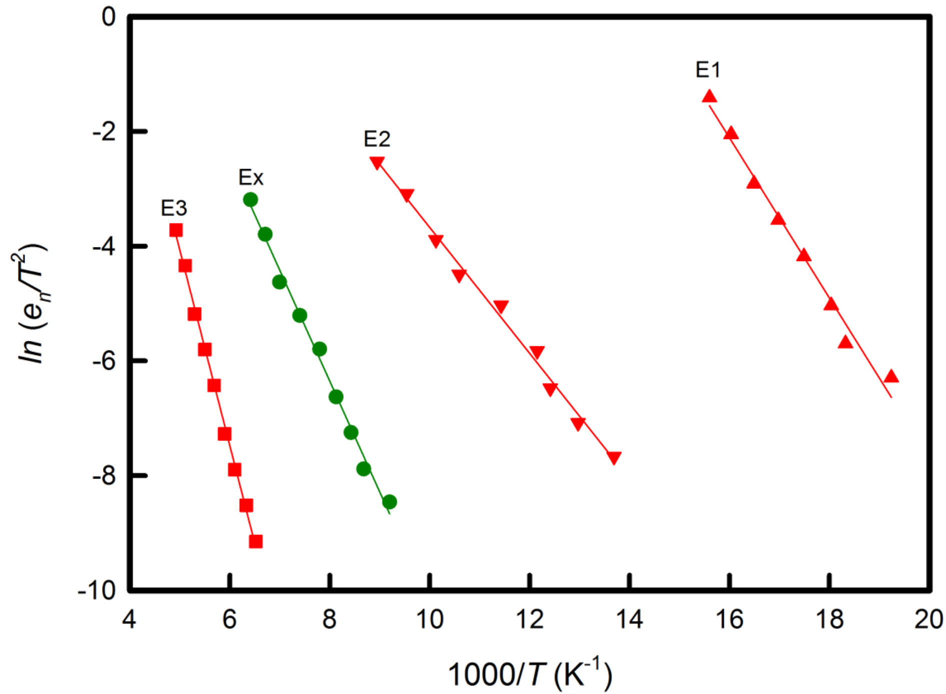

Figure 6.3.3.3.4: Arrhenius plots obtained from Pd Schottky contacts deposited on 700°C argon annealed ZnO.

Table 6.3.3.3.2: *Values of activation enthalpy and capture cross section for the Pd Schottky contacts deposited on un-annealed and 700°C argon annealed ZnO. The activation enthalpy is measured relative to the minimum of the conduction band.*

Annealing temperature (°C)	E1 (meV)	Capture cross section (cm^2)	E2 (meV)	Capture cross section (cm^2)	Ex (meV)	Capture cross section (cm^2)	E3 (meV)	Capture cross section (cm^2)	E4 (meV)	Capture cross section (cm^2)
No anneal	120	5×10^{-12}	100	1×10^{-16}	--------	--------	300	3×10^{-14}	-----	---------
700	120	9×10^{-12}	95	2×10^{-17}	167	1×10^{-16}	293	1×10^{-16}	-----	---------

Of particular interest is the introduction of E4 after annealing ZnO in different ambient conditions. Repeated Ar annealing on several samples from the same batch shows the introduction of E4 at 300°C, 500°C and 600°C and not at 400°C. However, oxygen annealing does not introduce E4 after 300°C, 500°C and 600°C, but it is only observed after annealing ZnO samples at 400°C which is exactly the opposite case for Ar annealing. Figure 6.3.3.3.5 shows the spectra obtained from the 400°C argon annealed and 400°C oxygen annealed samples. The insert shows the E4 peak. The intensity of E3 seems to be affected by the formation of either the Ex or E4 deep level for all the annealing conditions and ambient used in this study. The E4 peak is broad, indicating that it may consist of two or more energy levels which are closely spaced. Laplace-DLTS has been employed to separate these closely

spaced energy levels. Results are presented in the attached publication in section 6.3.4. It must be noted that E4 only refers to the fourth peak that is induced by annealing, not necessarily that the deep level defects introduced during argon annealing at 300°C, 500°C and 600°C and oxygen annealing at 400°C are the same.

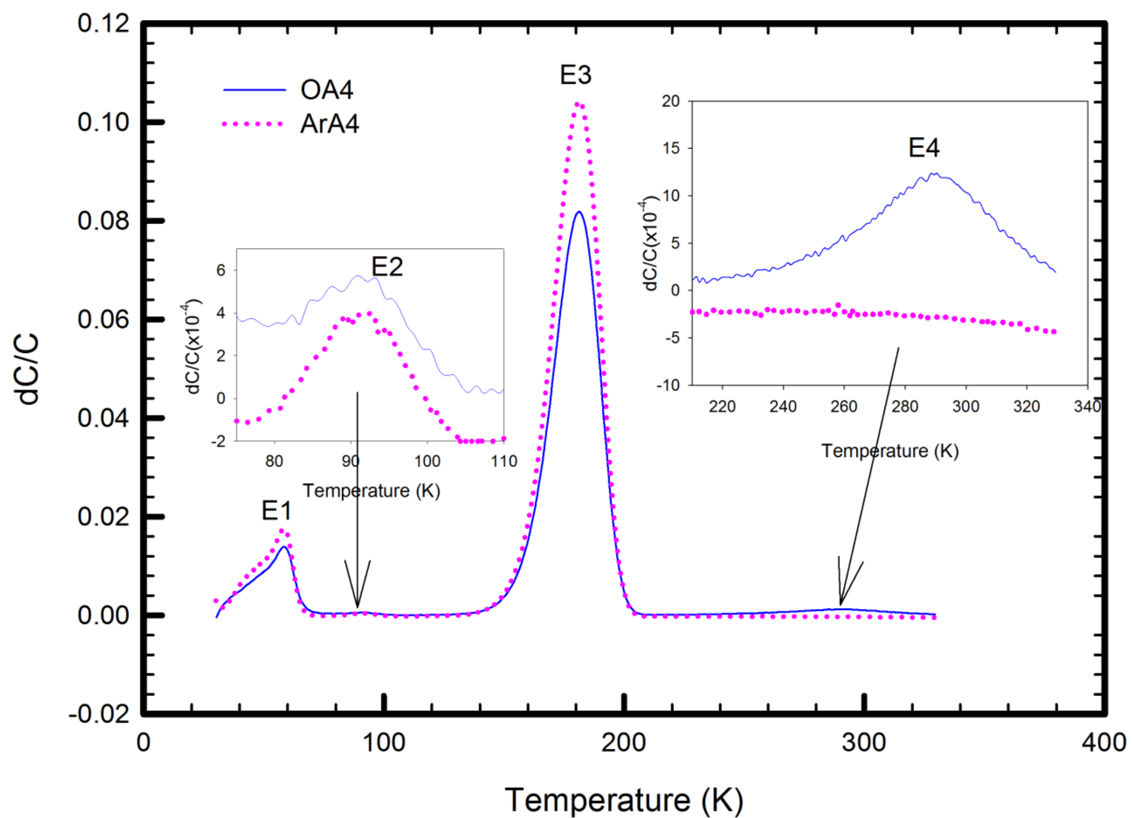

Figure 6.3.3.3.5: DLTS spectrum obtained from Pd Schottky contacts deposited on oxygen and argon annealed ZnO. The spectra were recorded at a quiescent reverse bias of -2.0 V, filling pulse of 0.30 V, filling pulse width of 2 ms and rate window of 100s^{-1} in the temperature range 30 – 350 K. OA4 and ArA4 indicate the sample annealed in oxygen at 400°C and argon at 400°C, respectively. The inserts show the E2 and the E4 peak observed in the oxygen annealed samples.

Since it has been observed that the defects induced through annealing are ambient related and not thermally related, a study of the annealing induced defects at 300°C in different ambient conditions is presented in publication 5 obtained from the link below.

BESTPFE.COM
List of research project topics and materials

Publication 5: Effects of hydrogen, oxygen, and argon annealing on the electrical properties of ZnO and ZnO devices studied by IV, DLTS and LDLTS

http://dx.doi.org/10.1063/1.4709728

Summary

Based on the findings of this study on annealing induced defects in ZnO, this subject is very complicated since one of the inert gases, i.e. argon can induce defects in ZnO. Identifying the nature of these annealing induced defects is still a subject under investigation. Table 6.3.3.3.3 presents the findings by other authors on the annealing induced defects in ZnO under various ambient conditions.

Table 6.3.3.3.3. *Summary of defects induced in as-received ZnO after annealing in different ambient conditions and temperatures.*

Growth Technique	Annealing Ambient	Annealing temperature (°C)	Defect/s induced	Identity	Ref
Melt	Vacuum	400	--------	---------	This work
		600	--------		This work
		700	--------		This work
	O_2	300	--------	--------	[6]
		400	E4 (0.60 eV)	?	This work
		500	--------	--------	This work
		600	--------	---------	This work
		700	--------	---------	This work
	Ar	300	E4 (0.67 eV)	?	[6]
		400	-------	--------	[8]
		500	E4	?	[8]
		600	E4	?	[8]
		700	Ex (0.16 eV)	?	[8]
	H_2	300	E4 (0.60 eV)	?	[6]
Hydrothermal	O_2 N_2 Ar	1400	E4(0.54 eV)	Zn deficiency related	[11]
	N_2/H_2	700			

Conclusions

Annealing of samples prior to Schottky contact fabrication allows for the determination and characterization of high temperature annealing induced deep level defects in melt grown single crystal ZnO. Within the temperature range studied, i.e. 300°C – 700°C, vacuum annealing does not induce any new defects, neither does it anneal out the prominent defects observed in the as-grown material. Oxygen annealing also does not introduce defects on all the other temperatures, except at 400°C where E4 is induced. The identity of E4 is not known as yet. With Ar annealing, a deep level defect labelled E4 is observed at 300°C, 500°C and 600°C. It must be mentioned that this defect is not the same for the three different annealing temperatures. 400°C Ar annealing does not induce any defect in ZnO and also does not anneal out the E1, E2 and E3 defects. Annealing the ZnO samples in Ar at 700°C results in E4 annealing out and a new deep level defect, Ex being induced. Hydrogen annealing has only been performed at 300°C where a deep level defect labelled E4 has also been induced. Melt grown single crystal ZnO samples annealed in different ambient conditions and temperatures reveal the introduction of defects which are ambient and temperature related. This behaviour of ZnO enables, and is significant for defect engineering within the material where if certain defects with certain properties are required, their introduction can be easily achieved and controlled by either using specific temperature and/or ambient conditions.

References

1. C. R. Crowell and V. L. Rideout, Solid-St. Electron. **12**, 89 (1969)
2. A. K. Srivastava, B. M. Arora, and S. Guha, Solid-St. Electron. **24**, 185 (1981)
3. A. K. Srivastava, and B. M. Arora, Solid-St. Electron. **24**, 1049 (1981)
4. S. M. Sze, Physics of Semiconductor devices, Wiley, New York, 2nd Ed., p.292 (1981)
5. H. von Wenckstern, PhD Thesis, Universitat Leipzig (2008)
6. W. Mtangi, F. D. Auret, W. E. Meyer, M. J. Legodi, P. J. Janse van Rensburg, S. M. M. Coelho, M. Diale, and J. M. Nel, J. Appl. Phys. **111**, 094504 (2012)
7. W. Mtangi, F.D. Auret, P.J. Janse van Rensburg, S. M. M. Coelho, M. J. Legodi, J.M. Nel, W.E. Meyer, J. Appl. Phys. **110**, 094504 (2011)
8. W. Mtangi, F. D. Auret, M. Diale, W. E. Meyer, A. Chawanda, H. de Meyer, P.J. Janse van Rensburg, and J. M. Nel J. Appl. Phys. **111**, 084503 (2012)
9. Z. R. Ye, X. H. Lu, G. W. Ding, C. C. Ling, G. Brauer, and W. Anwand, Semicond. Sci. Technol. **26**, 095016 (2011)
10. Q. L. Gu, C. K. Cheung, C. C. Ling, A. M. C. Ng, A. B. Djurisic, L. W. Lu, X. D. Chen, S. Fung, C. D. Beling and H. C. Ong, J. Appl. Phys. **103**, 093706 (2008)
11. V. Quemener, L. Vines, E. V. Monakhov, and B. G. Svensson, Int. J. Appl. Ceramic. Technol. **8**, 1017 (2011)

6.3.4 Argon and Oxygen annealing

Introduction

Following the results that have been presented in the previous sections, a study has been performed to investigate whether it is possible to anneal out the E4 deep level defect in oxygen ambient at the same temperature at which it has been introduced through argon annealing.

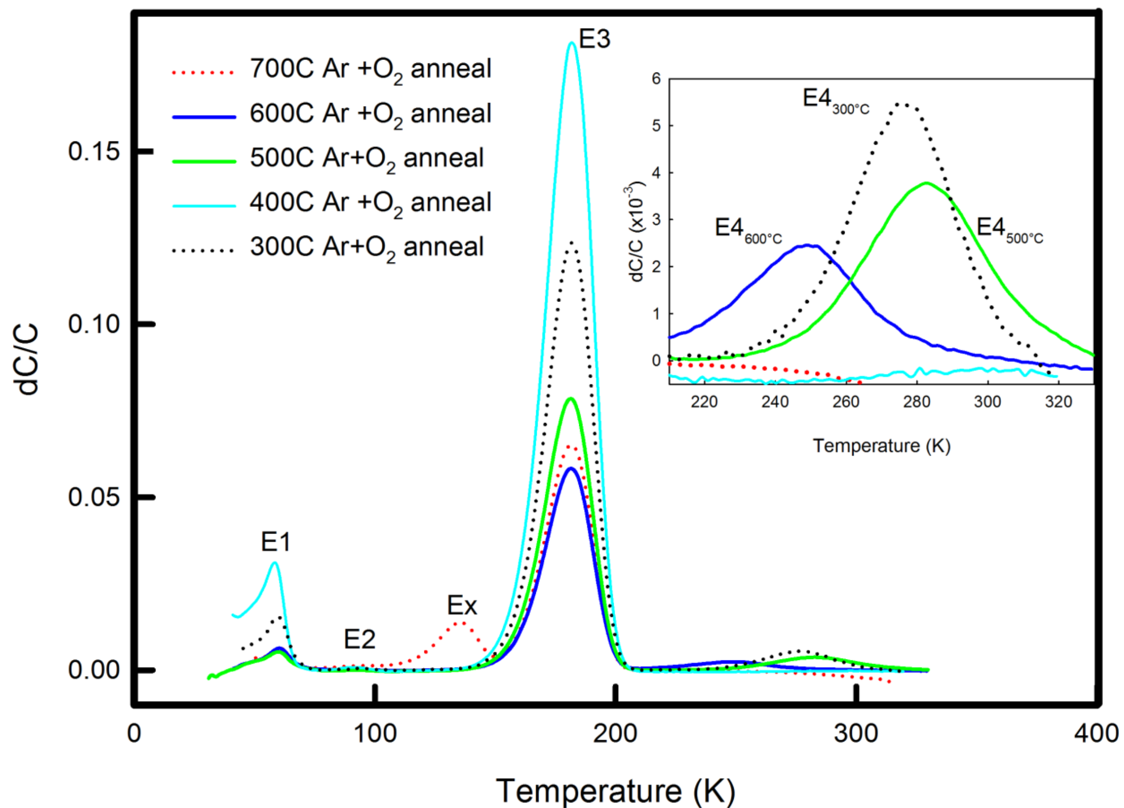

Figure 6.3.4.1: Normalized DLTS spectra of ZnO samples annealed in Ar + O_2 at different temperatures. The spectra were recorded on the 11th of November 2011. The measurement conditions comprised of a quiescent reverse bias of 2.0 V, filling pulse V_p = 0.3 V, filling pulse width of 2.0 ms and a rate window of 100 s^{-1}.

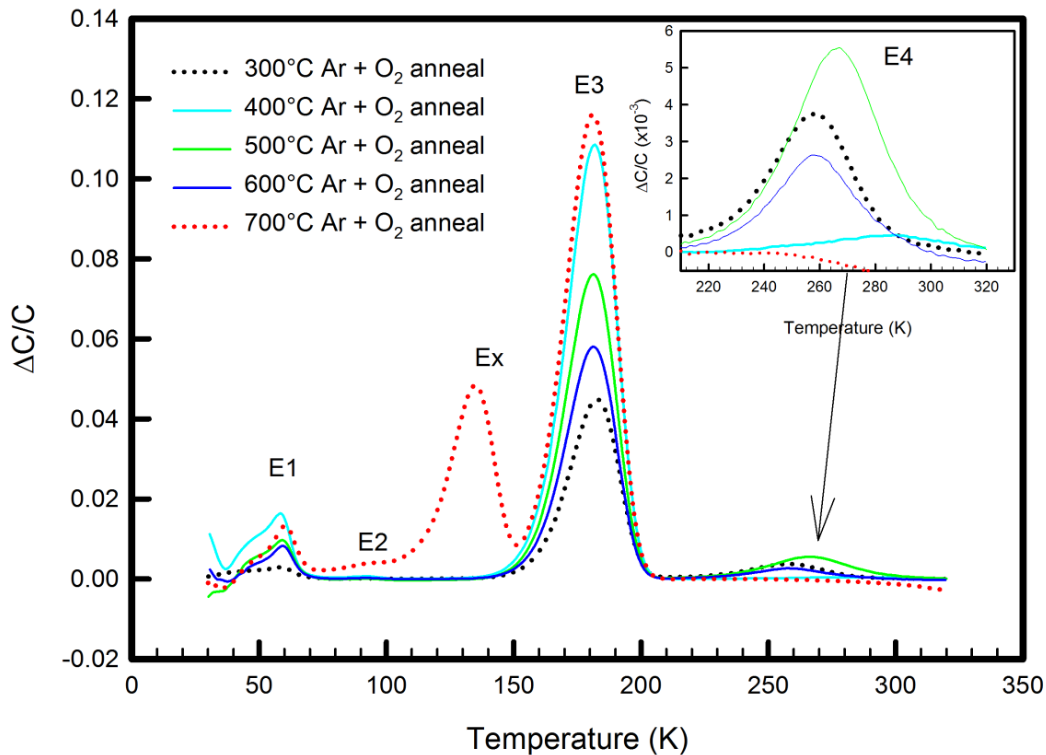

Figure 6.3.4.2: Normalized DLTS spectra of ZnO samples annealed in Ar + O_2 at different temperatures. The spectra were recorded on the 5th of May 2012. The measurement conditions comprised of a quiescent reverse bias of 2.0 V, filling pulse V_p = 0.3 V, filling pulse width of 2.0 ms and a rate window of 100 s^{-1}.

Figure 6.3.4.1 shows the DLTS spectra of the Ar + O_2 annealed samples determined on the 11th of November 2011, while Figure 6.3.4.2 shows the spectra that was obtained on the 5th of May 2012. When the measurements were performed just after contact fabrication, the 400°C Ar + O_2 annealed samples did not show the E4 peak. Six months later, the 400°C annealed sample now shows the E4 peak. All the annealing induced defects indicate a change in either the peak height or the peak position (in terms of temperature). After six months, the intensity of the E4 in the 500°C annealed samples is now higher than that of the 300°C annealed samples. The intensity of the normalized E3 peak for the annealed samples also appears to change with time. It appears as if the E4 peak affects the E3 peak in one way or the other. Using the 400°C annealed sample as an example; when E4 was not present, the intensity of the E3 peak was high (Figure 6.3.4.1). With the E4 peak appearing, the intensity of E3 decreases (Figure 6.3.4.2). For the 400°C Ar annealed samples fabricated on the same day (Figure not shown), after the same number of months, E4 is still not present. Hence O_2 is responsible for the E4 peak that has been observed in the 400°C Ar + O_2 annealed samples.

Figure 6.3.4.3 shows the Arrhenius plots for the annealing induced defects in the Ar + O2 annealed samples. The values of the estimated activation enthalpies and apparent capture cross-sections are presented in Table 6.3.4.1.

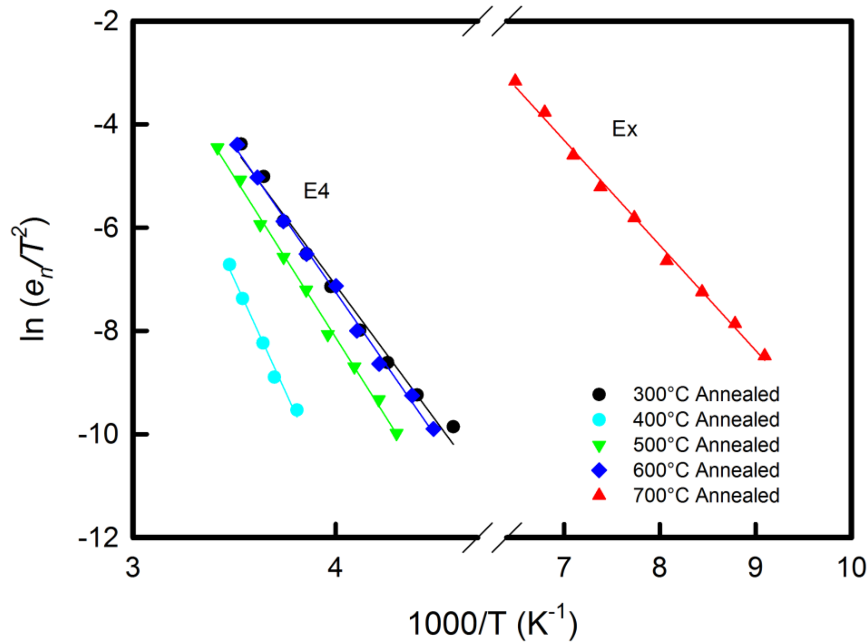

Figure 6.3.4.3: Arrhenius plots for the annealing induced defects in ZnO after Ar + O_2 annealing.

Table 6.3.4.1*: Values of annealing temperature, estimated activation enthalpy and apparent capture cross-section for the annealing induced defects in ZnO from measurements performed on 5 May 2012.*

Annealing Temperature (°C)	Activation enthalpy (meV)	Apparent capture cross-section (cm^2)
300	E4(460)	2×10^{-14}
400	E4(740)	2×10^{-10}
500	E4(540)	3×10^{-13}
600	E4(490)	7×10^{-14}
700	Ex(160 – 180)	3×10^{-16}

From the Arrhenius plots, the estimated activation enthalpy and apparent capture cross-section, it can be clearly observed that the defect labelled E4 is not the same for the 300°C, 400°C and 600°C.

More details on the Ar + O_2 studies are presented in publication 6 obtained from the provided link. The publication outlines the experimental procedure, results and discussions and conclusions drawn from this investigation.

Publication 6: Effects of high temperature annealing on single crystal ZnO and ZnO devices

http://dx.doi.org/10.1063/1.3700186

Summary

Annealing melt grown single crystal ZnO in Ar ambient at high temperatures introduces deep level defects. These deep levels tend to affect the electrical properties of the Schottky contacts fabricated on the annealed material by increasing the reverse leakage current and the series resistance of the contacts. DLTS measurements performed on ZnO material annealed at different temperatures reveal different deep level defects induced at those particular temperatures. An increase in annealing temperature results in a transformation of the observed deep level defects. Below the annealing temperature of 700°C, a deep level defect labelled E4 appeared in the DLTS spectra slightly below room temperature. After 700°C annealing, the E4 deep level defect anneals out and a new low temperature deep level defect, Ex is induced. These deep levels can be said to be unstable as they show some changes in the temperature peak position with time. These changes could be due to changes in the environmental conditions, particularly the temperature at which the samples are kept, which in this particular study is room temperature. For the 400°C Ar + O_2 annealed samples, the E4 deep level defect, which is not observed just after contact fabrication, is observed after a period of time, in this case, six months. This might be a result of room temperature annealing of the samples which activates some defect species. However the E4 deep level is not induced in the 400°C Ar annealed samples kept in the same environment for the same amount of time. The question is: (i). what does Ar annealing do to the samples? (ii). what is the effect of oxygen annealing on Ar annealed ZnO samples? This question is yet to be answered after further investigations.

6.4 Irradiation induced defects

Introduction

ZnO has the potential to be used in the fabrication of UV detectors and space applications. In space applications, devices often operate in harsh radiation conditions which comprise of highly energetic particles and elevated temperatures. This requires the material to be highly resistant to radiation damage for devices to operate reliably for extended periods. In this section, the effects of exposing Pd Schottky contacts to H^+ ion irradiation are presented.

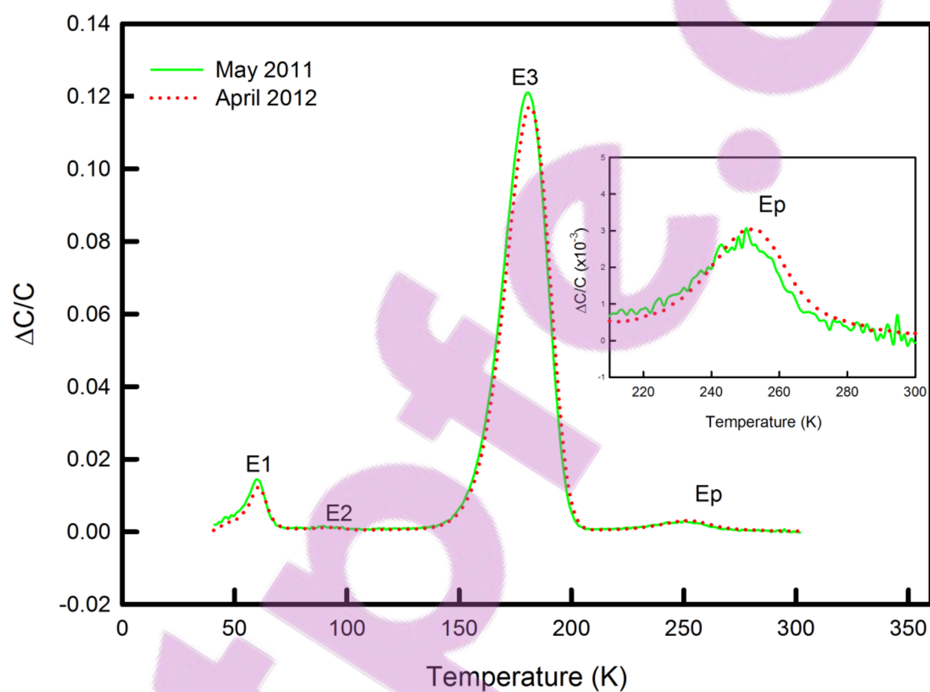

Figure 6.4.1: DLTS spectra for the proton irradiated Pd/ZnO Schottky contacts. These spectra were recorded at a quiescent reverse bias of 2.0 V, V_p = 0.3 V and filling pulse width of 2.0 ms and rate window of 100 s^{-1}. The green solid line shows the spectrum recorded in May 2011, while the red dotted line indicates the spectrum obtained in April 2012.

Figure 6.4.1 shows the DLTS spectra of the 1.6 MeV proton irradiated ZnO samples. The spectra show three prominent peaks that have also been observed in the as-grown samples. An extra peak labelled Ep has been introduced by proton irradiation. The estimated activation enthalpy and capture cross-sections are given in the Arrhenius plots of Figure 6.4.2. The proton induced defect has an activation enthalpy of 533 meV and an apparent capture cross-section of about $1 \times 10^{-12}\text{cm}^2$. A defect with almost the same energy level was observed by

Bestpfe.com

Auret *et al.*[1] in SCVT grown samples after 1.8 MeV proton irradiation. In their study, they report an activation enthalpy of Ep1 to be 0.54 ± 0.02 eV and an apparent capture cross-section of $(3.0 \pm 1.0) \times 10^{-13}\text{cm}^2$. Schmidt [2] also reported a defect which he labelled E4 in ZnO thin films after 1.6 MeV proton irradiation, with activation energy of 0.55 eV. There is therefore a high possibility that the Ep defect is the same as the Ep1 observed by Auret *et al.* [1] and the E4 observed by Schmidt [2]. As shown in Figure 6.4.1, the Ep defect shows high stability for a sample kept at room temperature conditions. The spectra recorded after almost a year indicates the presence of Ep with almost the same concentration.

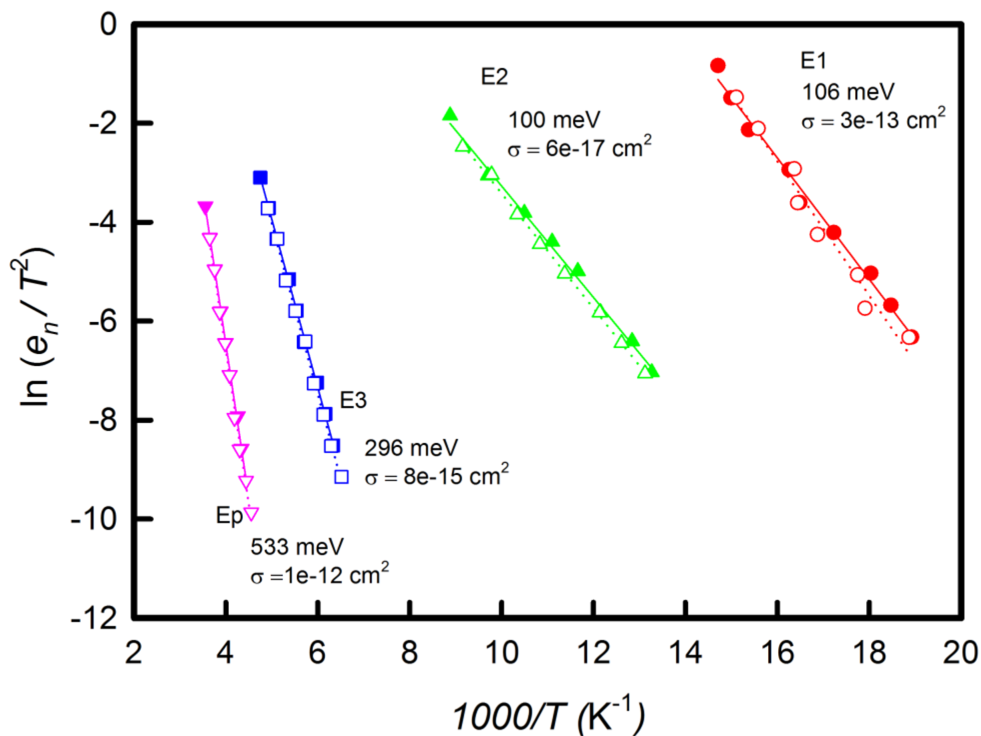

Figure 6.4.2: Arrhenius plots obtained from the 1.6 MeV proton irradiated Pd/ZnO Schottky contacts. Filled symbols indicate the measurements performed in May 2011 while the empty symbols represent the data obtained in April 2012.

The stability of the Ep defect is also illustrated using the depth profile of Figure 6.4.3. This profile was recorded at a constant reverse bias of 2.0 V and increasing pulses in steps of 0.1 V. As demonstrated in Figure 6.4.3, the concentration at any given depth for the sample evaluated in May 2011 is slightly higher than the concentration determined in April 2012, but to within experimental error these values are almost the same. This clearly indicates that once introduced, the Ep1 is stable for the period specified in this study. The same is observed for the E1, E2 and E3 peaks as illustrated in the Arrhenius plots of Figure 6.4.2.

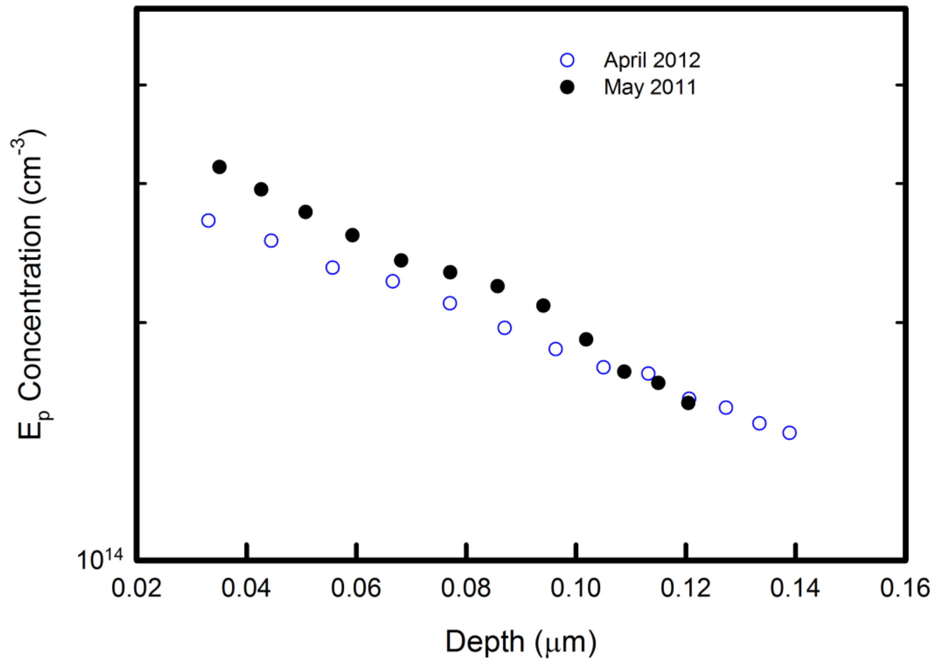

Figure 6.4.3: Variation of trap concentration with depth obtained from the irradiation induced E_p peak observed in Pd/ZnO Schottky contacts.

Summary

Exposing ZnO to highly energetic particles introduces a new deep level defect. However this defect exists in low concentration indicating that ZnO is resistant to radiation damage to some extent. The irradiation induced peak has proved to be stable within the period evaluated within this particular study. Introduction of Ep after irradiation has no effect on the other peaks already present in the material.

References

1. F.D. Auret, S.A. Goodman, M. Hayes, M.J. Legodi, H.A. van Laarhoven, and D.C. Look, Appl. Phys. Lett., **79**, 3074 (2001)
2. M. Schmidt, PhD Thesis, Leipzig University (2011)

BESTPFE.COM
List of research project topics and materials

Chapter 7

Conclusions

Electrical characterization of process, annealing and irradiation induced defects in ZnO has been successfully achieved using conventional and Laplace DLTS techniques. Conclusions drawn from these studies are given at the end of each section in the results and discussions chapter. In this chapter, the major highlights of the study are briefly stated.

Melt grown ZnO samples have revealed the presence of three prominent point defects, two of which have been explained as being native to the material, i.e. $E1 = E_c - 0.12$ eV and $E2 = E_c - 0.10$ eV. The E3 defect with energy level of approximately 0.30 eV below the minimum of the conduction band has been explained as an extrinsic defect. The identities of these defects are not known yet. E1 and E3 have often been observed in ZnO material grown using different techniques implying they are common to ZnO. The E2 defect has however not been observed in other ZnO material grown using other techniques except in SCVT and MG samples. Thus during material growth and processing, three deep level defects as determined from DLTS are introduced into melt grown ZnO samples.

Results from this study also indicate the effects of the fabrication techniques on the quality of contacts fabricated and the deep level defects introduced into the material. Resistive evaporation techniques yield high quality contacts on melt grown ZnO samples without any deep level defect being introduced during contact fabrication, while the electron-beam deposition technique introduces deep level defects into the semiconductor material with very high concentrations closer to the metal/semiconductor interface. The source of these defects has been explained as possibly due to the ionized heavier gas particles and also stray electrons. This is because the filament is not a true point source of electrons, hence the residual heavier gas particles around and close to the filament area are ionized and are not effectively bent by the magnetic field, hence they end up impinging onto the sample causing damage to the surface.

Annealing of ZnO has proved to be a very significant and crucial step in processing the material for device fabrication. This step provides an avenue for defect engineering in ZnO and possibly a major stride in the realization of p-type ZnO once the optimum conditions for the control of native defects in terms of temperature and ambient conditions have been obtained. This is because the properties of the material and the defects induced during annealing strongly depend on the annealing ambient and temperatures. Annealing of ZnO can also help in understanding and controlling the n-type conductivity in the material. Since ZnO is believed to contain deep states with good colour rendering properties, devices which produce these particular colours can be easily achieved by annealing the material to introduce or activate these states and it is also possible to get rid of unwanted deep level defects through annealing.

Even though annealing has proved to control defects in ZnO (by introducing them and annealing them out), the most important, missing part of the puzzle pertains to the identity, nature and properties of these deep level defects.

Summary of deep level defects observed and characterized in this study

Defect Label	Activation enthalpy (meV)	Capture cross-section (cm^2)	Origin	Identity
E1	110 – 120	$(4 - 7) \times 10^{-12}$	Material growth related	O_i
E2	98 – 100	$(1 - 9) \times 10^{-17}$	Material growth related	?
E3	290 – 310	$(0.7 - 3) \times 10^{-14}$	Material growth related	Transition metal ion
Ex	160 – 180	$(1 - 3) \times 10^{-16}$	700°C Ar Annealed 700°C Ar + O_2 Annealed	?
E4	600 ± 10	$1.4 \pm 0.2 \times 10^{-12}$	Pd e-beam deposition	Oxygen vacancy?
	480 ± 10	$5.0 \pm 0.5 \times 10^{-12}$	Ir e-beam deposition	
	690 ± 10	$1.4 \pm 0.2 \times 10^{-14}$	Pt e-beam deposition	
E4	670 ± 10	$2 \pm 0.2 \times 10^{-11}$	300°C Ar Annealed	?
E4a	680 ± 20	$6 \pm 0.1 \times 10^{-12}$	300°C Ar Annealed	
E4b	590 ± 20	$6 \pm 0.1 \times 10^{-13}$	300°C Ar Annealed	
E4c	500 ± 10	$4 \pm 0.2 \times 10^{-14}$	300°C Ar Annealed	
E4	460 ± 10	$2 \pm 0.2 \times 10^{-14}$	300°C Ar + O_2 Annealed	?
E4a	490 ± 10	$4 \pm 0.2 \times 10^{-15}$	300°C Ar + O_2 Annealed	
E4b	520 ± 10	$6 \pm 0.2 \times 10^{-14}$	300°C Ar + O_2 Annealed	
E4c	530 ± 10	$2 \pm 0.2 \times 10^{-13}$	300°C Ar + O_2 Annealed	
E4	740 ± 20	$2 \pm 0.5 \times 10^{-10}$	400°C Ar + O_2 Annealed	?
E4	540 ± 20	$3 \pm 1 \times 10^{-13}$	500°C Ar + O_2 Annealed	?
E4a	620 ± 10	$3 \pm 1 \times 10^{-13}$	500°C Ar + O_2 Annealed	
E4b	470 ± 10	$3 \pm 1 \times 10^{-15}$	500°C Ar + O_2 Annealed	
E4c	440 ± 10	$2 \pm 0.5 \times 10^{-15}$	500°C Ar + O_2 Annealed	
E4	490 ± 20	$7 \pm 2 \times 10^{-14}$	600°C Ar + O_2 Annealed	?
	600 ± 10	$4 \pm 1 \times 10^{-13}$	400°C O_2 Annealed	
	600 ± 10	$5 \pm 1 \times 10^{-13}$	300°C H_2 Annealed	
	530 ± 20	$1 \pm 0.5 \times 10^{-12}$	Proton irradiation	

E4 refers to the fourth defect observed in the material

Chapter 8

Future Work

Due to the chemical blindness/inability of space charge spectroscopy, the identity of the deep level defects observed and studied in this work is not known yet. Different experiments like ion implantation, positron annihilation spectroscopy, electron paramagnetic resonance, just to mention a few need to be conducted so as to identify the nature and origins of the these deep level defects observed in ZnO. Some of the work that still needs to be performed to get more insight on deep levels in ZnO are:

- Optical DLTS
  -To fully understand the nature and the electronic properties of the E3 deep level.
  - To probe the entire bandgap so as to reveal information of all the annealing induced defects in ZnO.
  - To identify the nature of the annealing induced E4 defect which is assumed to be oxygen vacancy related.
  - To get an idea of how the annealing induced Ex deep level behaves under optical excitation and hence the proof that it is the same as the reported T2 deep level.
- Identify the nature of the electron-beam induced defect by introducing them in a controlled manner
- Perform in-situ annealing and space charge spectroscopy experiments to study the kinetics of each annealing induced defect.
- Since it's proposed that ZnO can be used to fabricate devices that can operate in the UV region and space applications, there is need to perform further annealing studies using different ambient and temperature conditions, to fully understand how devices fabricated on ZnO would perform in highly elevated temperatures.
- Since annealing has proved to increase the acceptor concentration in ZnO, it is important to find a technique of characterizing deep acceptors in ZnO.

- Since annealing has indicated the introduction of deep level defects with high concentrations closer to the surface, surface studies are also required to study the morphology of the surface after annealing the samples.